

Masthead Logo

UNLV Theses, Dissertations, Professional Papers, and Capstones

December 2018

Design and Preliminary Evaluation of a Supercritical Carbon Dioxide Brayton Cycle for Solar Dish Concentrator Clean Energy Production

Danielle Nobles-Lookingbill
Danielle.NoblesLookingbill@gmail.com

Follow this and additional works at: <https://digitalscholarship.unlv.edu/thesesdissertations>

Part of the [Mechanical Engineering Commons](#), [Oil, Gas, and Energy Commons](#), and the [Sustainability Commons](#)

Repository Citation

Nobles-Lookingbill, Danielle, "Design and Preliminary Evaluation of a Supercritical Carbon Dioxide Brayton Cycle for Solar Dish Concentrator Clean Energy Production" (2018). *UNLV Theses, Dissertations, Professional Papers, and Capstones*. 3439.
<https://digitalscholarship.unlv.edu/thesesdissertations/3439>

This Dissertation is brought to you for free and open access by Digital Scholarship@UNLV. It has been accepted for inclusion in UNLV Theses, Dissertations, Professional Papers, and Capstones by an authorized administrator of Digital Scholarship@UNLV. For more information, please contact digitalscholarship@unlv.edu.

DESIGN AND PRELIMINARY EVALUATION OF A SUPERCRITICAL CARBON DIOXIDE

BRAYTON CYCLE FOR SOLAR DISH CONCENTRATOR

CLEAN ENERGY PRODUCTION

By

Danielle Nobles-Lookingbill

Bachelor of Science – Psychology
Indiana University, Bloomington
1999

Bachelor of Science – Mechanical Engineering
University of Nevada, Las Vegas
2014

A dissertation submitted in partial fulfillment
of the requirements for the

Doctor of Philosophy in Engineering – Mechanical Engineering

Department of Mechanical Engineering
Howard R. Hughes College of Engineering
The Graduate College

University of Nevada, Las Vegas
December 2018

Copyright 2019 Danielle Nobles-Lookingbill
All Rights Reserved

October 29, 2018

This dissertation prepared by

Danielle Nobles-Lookingbill

entitled

Design and Preliminary Evaluation of a Supercritical Carbon Dioxide Brayton Cycle for
Solar Dish Concentrator Clean Energy Production

is approved in partial fulfillment of the requirements for the degree of

Doctor of Philosophy in Engineering – Mechanical Engineering
Department of Mechanical Engineering

Robert Boehm, Ph.D.
Examination Committee Chair

Kathryn Hausbeck Korgan, Ph.D.
Graduate College Interim Dean

Yi-Tung Chen, Ph.D.
Examination Committee Member

Alexander Barzilov, Ph.D.
Examination Committee Member

Yahia Baghzouz, Ph.D.
Examination Committee Member

Jacimaria Batista, Ph.D.
Graduate College Faculty Representative

ABSTRACT

As we move toward energy independence and more ambitious clean energy goals, solar energy research must push the efficiency limits of traditional energy generation systems. Increases in efficiency can be achieved by increasing the hot temperature of the power cycle. Recent research demonstrates the potential for increased efficiency and a vastly smaller component size when supercritical carbon dioxide Brayton power cycles are used. Concentrated solar and nuclear heat sources are capable of achieving the high working fluid temperatures needed for significant efficiency gains. This NSF EPSCoR funded, experimental research system is designed to exploit the uniquely immense solar irradiance of the Mojave Desert, coupling a solar dish concentrator with the UNLV supercritical carbon dioxide (SCO₂) Brayton cycle, fabricated on campus at the UNLV Center for Energy Research and the UNLV Machine Shop. This, in conjunction with dry cooling, compounds the capacity for increased efficiency with trivial water consumption and decreased environmental and geographical footprints.

Photographic flux mapping (1) was used to provide solar flux information leading to the custom design and on-site fabrication of the solar receiver. A custom air-cooled heat exchanger with expansion capabilities was designed and fabricated for heat rejection. To further increase efficiency, internationally collaborative custom minichannel heat exchangers from the research team at Xi'an Jiaotong University, P.R. China, were added in both zigzag and straight channel geometries; these heat exchangers are installed in parallel, with isolation valves, for experimental comparison and singular recuperation in the system. The turbine and compressor housing exhibits a modular design to allow ease of desired experimental modifications. All components are mounted on an SAIC dish concentrator solar tracking system for on-sun experimental testing. A computational model of the solar receiver and heat rejection system, as well as the entire power cycle, has been created in Engineering Equation Solver (EES).

On-sun experimental tests of the solar receiver and heat rejection systems have indicated system capability to both reach high temperatures and reject the heat required to achieve accelerated efficiencies.

Once high efficiency temperature ranges are achieved, efficient turbomachinery is required for high efficiency operational success. Fabrication issues and resolutions surrounding the machining of small turbomachinery in this high temperature environment are described as a part of this research. Of particular consequence are issues surrounding the design and fabrication of the turbo-compressor shaft to housing interface. Bearing issues prove to be the core limitation preceding successful operational performance of the turbo-compressor unit. Decisions leading to the successful resolution to this issue are also described.

This concentrated solar research system is a demonstration of the innovative component and system design needed to reach the next level in clean solar energy using trivial water consumption. The experimental and computational components support previous theories for the role of concentrated solar in clean power generation systems with increased efficiencies. This experimental system provides proof of concept for supercritical carbon dioxide Brayton cycles with solar concentrator technology, contributes to the advancement of SCO₂ Brayton cycle component fabrication processes, and displays the capacity of UNLV to move this SCO₂ turbo-compressor unit toward commercialization.

ACKNOWLEDGEMENTS

This material is based upon work supported by the National Science Foundation under grant number IIA-1301726. Extreme gratitude goes to the National Science Foundation EPSCoR Solar Energy, Water, Environment Nexus in Nevada project and the UNLV Center for Energy Research for financial support throughout the entirety of my doctoral research studies. This gratitude is extended to the Nuclear Regulatory Commission Nuclear Engineering Fellowship and the UNLV Graduate College STEM Fellowship for much appreciated, additional support.

A very special thank you goes to my advisor and mentor, Dr. Robert Boehm. You have been a supportive and caring mentor since I began working under your direction at the UNLV Center for Energy Research (CER) as an undergraduate research assistant. It has been an honor and privilege to learn, achieve, and grow as an engineer and leader under your superior and gracious example. Your trust in me to lead different initiatives and mentor undergraduate students, meeting CER research goals, is also greatly appreciated. This has helped me grow as a leader in the field we both love. A special thank you goes to Dr. Jacimaria Batista for your extraordinary support throughout my graduate career. You are an exemplary female role model, and your support and mentorship is invaluable. You too have paved the path for my growth as a leader in engineering and research. Thank you to Dr. Yi-Tung Chen. In addition to learning from you, I am extremely grateful for the international research experience you, Dr. Batista, Dr. Boehm, and Drs. Qui-wang Wang and Ting Ma of Xi'an Jiaotong University made possible. Thank you to Dr. Alexander Barzilov and Dr. William Culbreth for your mentorship, and your encouragement and support with regard to funding and internship opportunities. You have both made a true difference in helping me find the career path I am excited and motivated to pursue. A heartfelt thank you goes to Tasha Ramos and Joan Conway for everything you have done throughout both my graduate and undergraduate careers at UNLV. Your tremendous care for all students is humbling. Thank you to Dr. MaryKay Orgill, Dr. Markus Berli, Lori Ciccone, and Michele Casella for all of the different ways you have made a

significantly positive difference in my professional life. Thank you to Dr. Brendan O'Toole, Dr. Hui Zhao and Dr. Yahia Baghzouz for your support of my reaching this fantastic goal.

A very special thank you goes to Rick Hurt and Terry Kell for your valuable advice, expertise, and assistance with the design and fabrication of the system, particularly with the turbo-compressor unit. This level of research would not have been possible without your expertise and work. Thank you to Aaron Sahn for your consistent and valuable advice and assistance toward the design and fruition of this research project. Thank you to Trevor Rose for assistance with the SolidWorks drawings, Paolo Ginobbi for the PLC fundamental configuration and programming, Adam Betemedhin for assistance making modifications to the PLC, and to Veronica McKinney, Elizabeth Heider, Roy Lookingbill, and Francisco Chavarria for your valuable assistance on different configuration and fabrication parts of the whole.

My experience at the University of Nevada, Las Vegas has been amazing, and it is the people I have had the pleasure of learning from and working with over the past years that have made it so. I will be forever grateful.

DEDICATION

To God,
my husband, best friend, and partner, Roy W. Lookingbill,
my step-daughter of whom I am so proud, Samantha Lookingbill,
and to my loving parents, Fran Wagoner, and David and Judy Nobles.



TABLE OF CONTENTS

DISSERTATION APPROVAL	ii
ABSTRACT	iii
ACKNOWLEDGEMENTS	v
DEDICATION	vii
LIST OF TABLES	xii
LIST OF FIGURES	xiii
NOMENCLATURE.....	xvii
Greek Nomenclature	xx
Additional Subscript.....	xxi
EQUATIONS.....	xxii
CHAPTER 1. INTRODUCTION	1
CHAPTER 2. BACKGROUND	3
CHAPTER 3. SYSTEM DESIGN	12
3.1 Solar Receiver	13
3.2 Air Cooled Heat Rejection Heat Exchanger	30
3.2.1 EES Design Code for the Air Cooled Heat Rejection Heat Exchanger	31

3.3	Recuperator	32
3.3.1	Recuperator Design Considerations.....	33
3.4	Turbomachinery Design.....	35
3.4.1	Sonic Speed and Mach Number.....	35
3.4.2	Centrifugal Compressor Flow Conditions	42
3.4.3	Centrifugal Compressor Impeller Dimensions Design	44
3.4.4	Centrifugal Compressor Performance Design Considerations.....	48
3.4.5	Radial Inflow Turbine Impeller Dimensions Design	49
3.4.6	Radial Inflow Turbine Performance Design Considerations	51
3.5	Turbomachinery Fabrication.....	54
CHAPTER 4. ENGINEERING EQUATION SOLVER (EES) COMPUTER MODELING.....		60
4.1	Receiver/Turbine Interface.....	60
4.2	Turbine.....	61
4.3	Recuperator – Xi’an Jiaotong University Printed Circuit Heat Exchanger (XHEX).....	62
4.4	Air Cooled Heat Rejection Heat Exchanger (ACHEX).....	62
4.5	Compressor	63
CHAPTER 5. SENSING DEVICES		64
5.1	Omega High Temperature J Type Thermocouple Model XCIB-J-1-3-10.....	64

5.2	Omega High Temperature R Type Thermocouple Model XIN-P13R-U-187-26-M-TJ-BX-4	65
5.3	Omega High Temperature Resistance Temperature Detector Model CFTF-000-RTD-2-60-1- CC	66
5.4	Omega Pressure Transducer Model PX309-3KG5V	70
5.5	Kulite Super High Temperature Pressure Transducer Model XTEH-10L-190SM.....	72
5.6	Optical Rotational Speed Sensor Model	74
5.7	Rheonik Coriolis Flow Meter Model RHE08	76
5.8	Sensing System Overview	77
CHAPTER 6. DATA COLLECTION METHODS		78
6.1	Campbell Scientific Incorporated Model CR1000 Data Logger (CSI CR1000).....	78
6.2	Siemens Model S7-1200 Programmable Logic Control (PLC)	79
CHAPTER 7. RESULTS		81
7.1	ANSYS Compressor and Turbine Velocity Profile	81
7.1.1	ANSYS Model Framework and Results	81
7.1.2	ANSYS Conclusions.....	89
7.2	Solar Receiver Preliminary Material and Temperature Test Results	90
7.3	Solar Receiver and Heat Rejection Test Results	91

7.4	Turbomachinery Velocity Diagram and Performance Analysis	93
7.4.1	Turbine Velocity Triangles	94
7.4.2	Further Turbine Analysis	98
7.4.3	Compressor Velocity Triangles	101
7.4.4	Further Compressor Analysis.....	105
7.5	System Analysis Summary	111
CHAPTER 8. RECOMMENDATIONS FOR FUTURE WORK.....		112
8.1	Current Progress toward Future Work	113
8.1.1	Bearings	113
APPENDIX A.....		117
8.2	EES Raw Full System Code.....	117
REFERENCES.....		120
CURRICULUM VITAE.....		130

LIST OF TABLES

Table 1. Statistical Analysis of the Horizontal and Vertical Cross Sections	24
Table 2. Percentage of the Concentrated Solar Flux Captured by the UNLV Solar Receiver.....	30
Table 3. XJTU Numerical Design Parameters for the XPCHE	34
Table 4. Thermophysical Properties of Carbon Dioxide at Four Design Points.....	40
Table 5. High Temperature RTD Rational Polynomial Function Coefficients.....	67
Table 6. Full System Sensor List	77
Table 7. Turbine Stage Temperature Results.....	101
Table 8. Compressor Exit Velocity Triangle Results.....	104

LIST OF FIGURES

Figure 1. UNLV Supercritical Brayton Cycle Full System Design	13
Figure 2. SAIC Dish On-Sun Testing	14
Figure 3. Image of the Sun using 4-ND8 and 1-ND4 Filters	16
Figure 4. SAIC Dish Collection Area Reflective Collection Image using 2-ND8 Filters	16
Figure 5. Sun Image Pixel Conversion	17
Figure 6. Receiver Reflectance Ratio Image Collection Arrangement	20
Figure 7. SAIC Dish Receiver Collection Area Solar Flux Distribution	21
Figure 8. Solar Flux along a Horizontal Cross Section of the Receiver Area.....	23
Figure 9. Solar Flux along a Vertical Cross Section of the Receiver Area.....	23
Figure 10. Fractional Power Loss as a Function of Receiver Design Size	26
Figure 11. Component Fabrication using the UNLV Adjustable Radii Tube Bender Tool.....	28
Figure 12. Solar Receiver	28
Figure 13. Backside View of the Solar Receiver	29
Figure 14. Air Cooled Heat Rejection Heat Exchanger	31
Figure 15. Xi'an Jiaotong University Printed Circuit Mini-Channel Heat Exchanger	32
Figure 16. Zig-Zag Channel XHEX.....	33
Figure 17. Preliminary Recuperator Design Parameters.....	33

Figure 18. Fanno and Rayleigh Curve h-s Diagram	41
Figure 19. Illustration of Subsonic and Supersonic Flow (49)	42
Figure 20. Boyce's (50) Adiabatic Efficiency Estimation Based on Specific Speed	48
Figure 21. Barber-Nichols, Inc. Ns-Ds Turbine Chart (54)	52
Figure 22. Turbomachinery Vane Plate Assembly	54
Figure 23. Bolt Pattern Design in a Modular Casing Plate	55
Figure 24. Final SolidWorks Turbine Impeller Drawing	58
Figure 25. Final SolidWorks Compressor Drawing.....	58
Figure 26. Turbomachinery SolidWorks Assembly	59
Figure 27. Turbine and Compressor Wheel Prototypes	59
Figure 28. Omega CFTF-000-RTD-2-60-1-CC Resistance Temperature Device Wiring Schedule	69
Figure 29. Omega PX309-3KG5V Pressure Transducer Wiring Schedule	71
Figure 30. Omega PX-309-3KG5V Pressure Transducer Multiplier.....	71
Figure 31. Kulite Super High Temperature Pressure Transducer Wiring Schedule	73
Figure 32. Photologic Slotted Optical Switch Wiring Schedule (61)	75
Figure 33. Rheonik Coriolis Mass Flow Meter 4-20 mA Output Wiring Schedule	76
Figure 34. Campbell Scientific Inc. CR1000 Sensor Test Box.....	79
Figure 35. Completed Programmable Logic Controller Hardware View	80

Figure 36. ANSYS Flow Area as Defined for the Compressor (left) and Turbine (right).....	82
Figure 37. Compressor Mesh (left) and Turbine Mesh (right).....	83
Figure 38. Compressor Flow Area Velocity Profile for Mass Flow Rate 0.16 kg/s	85
Figure 39. Compressor Flow Area Velocity Profile for Mass Flow Rate 1.22 kg/s	85
Figure 40. Compressor Flow Area Streamline Profile.....	86
Figure 41. Turbine Flow Area Velocity Profile for Mass Flow 0.16 kg/s	87
Figure 42. Turbine Flow Area Velocity Profile for Mass Flow 1.22 kg/s	88
Figure 43. Turbine Flow Area Streamline Profile	89
Figure 44. Solar Receiver Segment Material Test	91
Figure 45. On-Sun Solar Receiver Temperature, ACHEX Temperature, and Mass Flow	93
Figure 46. Radial Inflow Turbine Inlet Velocity Triangle	95
Figure 47. Radial Inflow Turbine Exit Velocity Triangle.....	96
Figure 48. T-s Diagram for a Radial Inflow Turbine.....	99
Figure 49. Compressor Exit Blade Angle Definition using SolidWorks	103
Figure 50. Velocity Diagram for the Compressor Exit	103
Figure 51. Velocity Diagram for the Compressor Inlet	105
Figure 52. Air Bearing Test Configuration.....	114
Figure 53. UNLV Air Bearing	115

Figure 54. Angled View of a UNLV Air Bearing..... 115

Figure 55. Rotational Speed Measurements using a UNLV Separated Channel Air Bearing 116

NOMENCLATURE

A = Characteristic flow area (m)

a_{01} = Sonic speed for the fluid/ideal gas (m/s); characteristic flow area \approx diameter squared

C_p = Specific heat (J/kg K)

C_{w2} = Inlet tangential velocity (m/s)

C_{w3} = Exit tangential velocity (m/s)

c = Sonic velocity (m/s)

D = Diameter (m)

D_s = Specific diameter

E_b = Young's Modulus

E_{DNI} = Direct Normal Irradiance (W/m^2) at the time of sun image collection

$E_{R,i}$ = Irradiance (W/m^2) on a receiver element

F_{bt} = Per bolt force requirement

f_R = Receiver image attenuation factor

f_{Sun} = Sun image attenuation factor

H_{ad} = Adiabatic head (ft lbf/lbm)

h = Heat transfer coefficient ($kg/s^3 K$)

h_{01} = Enthalpy at flow position 1

h_{02} = Enthalpy at flow position 2

h_b = Blade height (m, in)

h_f = Specific enthalpy of saturated liquid (kJ/kg)

h_{fg} = Difference in specific enthalpy (kJ/kg) = $h_g - h_f$

h_g = Specific enthalpy of saturated vapor (kJ/kg)

I = Current (Amps)

k = Thermal conductivity (W/m K)

k_f = Thermal conductivity of the fluid (W/m K)

L = Characteristic length (m)

M = Molecular mass of the gas (kg/mol, g/mol)

Ma = Mach Number

\dot{m} = Mass flow rate (kg/s)

N = Rotational speed (rpm)

N_b = Blade number

N_{bt} = Bolt number

N_s = Nondimensional specific speed

Nu = Nusselt Number

Nu_{heating} = Dittus – Boelter Nusselt Number correlation for heating

Nu_{cooling} = Dittus – Boelter Nusselt Number correlation for cooling

n = Data sample size

P = Pressure (Pa)

P_{01} = Pressure at flow position 01, Compressor inlet (Pa)

P_{02} = Pressure at flow position 02, Compressor exit (Pa)

P_c = Critical Pressure

px^2 = Unit of one square pixel length

Q = Heat transfer (W)

Q_v = Volumetric flow rate (cfm)

R = Gas constant (kJ/kg K, J/mol K)

Re = Reynolds Number

R_x = Resistance (Ω)

r = Radius (m, in)

r_1 = Impeller radius at flow position 1, Compressor inlet (m, in)

r_2 = Impeller radius at flow position 2, Compressor exit (m, in)

r_{eye} = Radius of the impeller eye (m, in)

r_{hub} = Radius of the impeller hub (m, in)

S_y = Yield Strength

T = Temperature ($^{\circ}\text{C}$, K)

T_{01} = Stagnation temperature at flow position 01, Compressor inlet (K)

T_c = Critical temperature ($^{\circ}\text{C}$, K)

T_r = Nondimensional reduced temperature ($^{\circ}\text{C}$, K)

U = Characteristic impeller tip velocity (m / s)

U_2 = Blade speed at flow position 2, inlet (m/s)

U_3 = Blade speed at flow position 3 (m/s)

U_m = Mean blade speed given by the hub – eye mean location

u_{∞} = Fluid free stream velocity in the flow direction (m/s)

V = Velocity (m/s)

V_1 = Characteristic flow velocity at flow position 1, Compressor inlet (m/s)

$V_{CCD,i}$ = Individual digital receiver image pixel value per pixel area (Volts/ px^2)

$V_{CCD_{Sun},i}$ = Digital sun image response due to irradiance in pixel i (Volts/ px^2)

V_f = Fluid velocity (m/s)

V_{f1} = Fluid velocity at flow position 1, Compressor inlet (m/s)

V_{f2} = Flow velocity at flow position 2, Compressor exit (m/s)

V_x = Voltage (V)

v = Specific volume (m^3/kg)

v_f = Specific volume of saturated liquid (m^3/kg)

v_{fg} = Difference in specific volume (m^3/kg) = $v_g - v_f$

v_g = Specific volume of saturated vapor (m^3/kg)

w_s = Stage work per kg mass (Joule/kg)

x = Flow distance (m)

x_c = Critical flow distance; laminar to turbulent transition flow distance (m)

y = Data value

\bar{y} = Mean data value

Z_{ave} = Compressibility factor

Greek Nomenclature

α = Thermal diffusivity (m^2/s)

β = Exit blade angle (Degrees)

δ_b = Bolt deformation

η_p = Polytropic efficiency

η_s = Stage efficiency

μ = Dynamic viscosity (Ns/m^2) or ($\text{kg}/\text{m s}$)

μ_s = Slip factor

ν = Momentum diffusivity (m^2/s)

ρ = Fluid density (kg/m^3)

$\rho_{R,i}$ = Receiver reflectivity

σ = Standard deviation

σ_a = Stress (Pa)

γ = Poisson constant, specific heat ratio = C_p/C_v

γ_{sun} = Angle subtended by the sun (rad)

φ = Flow Coefficient

χ = Quality

ω = Rotational speed (rps, rpm)

ω_a = Eccentric factor, phase characterization factor

Additional Subscript

c = Compressor

t = Turbine

1 = Flow position 1

2 = Flow position 2

3 = Flow position 3

01 = Stagnation position 1

02 = Stagnation position 2

03 = Stagnation position 3

EQUATIONS

1. Mach Number

$$\text{Ma} \equiv \frac{V_f}{c}$$

2. Nusselt Number (2)

$$\text{Nu} \equiv \frac{hL}{k_f}$$

3. Prandtl Number (2)

$$\text{Pr} = \frac{C_p \mu}{k} = \frac{\nu}{\alpha}$$

4. Pseudo-critical Temperature as a function of pressure, P (3)

$$T_{pc}(P) = -122.6 + 6.124P - 0.1657P^2 + 0.01773P^{2.5} - 0.0005608P^3$$

5. Reynolds Number (2)

$$\text{Re}_x = \frac{\rho u_\infty x}{\mu}, x_c \text{ is substituted to calculate Critical Reynolds Number, } \text{Re}_{x,c} = 5E5$$

CHAPTER 1. INTRODUCTION

Nevada is a unique recipient of immense and consistent solar irradiance, creating an ideal environment for solar energy production. In order to properly expand solar energy production in a delicate environment like the Mojave Desert, water and environmental impacts must be considered. According to the National Weather Service, Las Vegas, Nevada receives 4.19 inches of rain per year, receiving 4.77 inches in 2017 (4). This low amount of rain means that the majority, typically 90%, of the water Las Vegas receives is from that released via the Colorado River, with the remainder provided by groundwater resources (5). In 2016, the National Renewable Energy Laboratory published water use estimates for concentrated solar farms in the desert southwest of 7.6 m³ per year (6). Without more efficient technology and the integration of dry cooling, this number is expected to rise (6), limiting Nevada to a mere 42% of the current Renewable Energy Standards and Renewable Energy Goals (7). Water resources are treasured and energy demand tends to continually increase, especially as the population in the Las Vegas valley continues to grow. Discounting the water demand issue, further complications occur as the cleaning process of concentrated solar farms introduce water not typically present to the environment. This addition of water coupled with the unnatural ground shading produced by the system creates changes in the desert ecosystem. The Solar Energy, Water, Environment Nexus in Nevada has developed technology and provided research answers leading to the valuable coexistence of these three factions, solar energy, water, and the environment, allowing renewable energy to grow responsibly in Nevada. This doctoral research is a part of this important Nexus.

The focus of this research is the design and proof of concept for a supercritical carbon dioxide Brayton cycle using a solar dish concentrator. This type of cycle provides a solar energy option, showing higher efficiency capabilities with smaller component size and little to no water requirement as compared to traditional steam cycles (8) (9) (10). Coupled with concentrated solar, the UNLV supercritical carbon dioxide Brayton cycle is the first of its kind. The system is expected to operate in an efficiency region

near similarly sized cycles in the literature. An opportunity for optimization and efficiency improvement is expected, and should be guided by the preliminary experimental data, which is within the scope of this doctoral research, as well as experimental data collected in the succeeding phase. This system will advance solar technology and renewable energy options in Nevada and across the country.

The UNLV Brayton cycle system design is described in Chapter 3, and is broken into sections corresponding to the different main components of the cycle. The most challenging component to design and fabricate predictably proved to be the turbo-compressor unit. This is the most intricate of the components, presenting the greatest number of design challenges. Chapter 3 also details both the individual impeller concerns and the considerations affecting the interconnectivity of both impellers, along with the decided solutions to these interconnected challenges. Chapter 4 describes how system modeling is used to assist in component design optimization, and provides overall operational expectations using Engineering Equation Software (EES).

Methods for experimental collection of data are described in Chapters 5 and 6. High temperature and pressure environments require specified sensor choice and placement. Each sensing device used in the experimental system is detailed in Chapter 5. Data collection methods supporting these sensing devices are described in Chapter 6. Preliminary test data were collected using a Campbell Scientific Model CR1000 Data Logger, and later phase data are collected using a Siemens Model S7-1200 Programmable Logic Control system. Results collected from preliminary tests, as well as a mathematical analysis of the turbine and compressor impellers are described in Chapter 7. Suggestions and plans for the continuation of this research are expressed in Chapter 8, along with the details of the current work toward these future goals.

CHAPTER 2. BACKGROUND

As worldwide energy consumption trends upward, developing more efficient, clean energy systems with decreased environmental and geographical footprints are necessary in energy generation research and development. In an effort to accomplish these goals, power generation systems other than the traditionally used Rankine cycle are considered. The idea of using supercritical power cycles has been among discussions since before Feher (8) published his theoretical conclusions in 1968. Advantages to using a supercritical carbon dioxide Brayton cycle, or SCO₂ Brayton cycle, include a vast decrease in component size, an increase in thermal efficiency, lack of phase change in heat rejection, blade corrosion resistance, and the ability to eliminate nearly all system water consumption when coupled with dry cooling. Additionally, carbon dioxide is preferable due to its abundance, lack of corrosiveness, non-combustibility, and low critical temperature and pressure when compared to some other gases and working fluids. (8) (9) (10)

For 100 MW test systems, Muto et. al. (11) found the supercritical carbon dioxide Brayton cycle exhibits a 3.6% advantage compared to the same cycle using either CO₂ above critical temperature but under critical pressure or helium. System complexity is increased due to high pressure and small component size (11). High pressure is required to maintain the supercritical state throughout the entire cycle, requiring components that possess specific and high pressure ratings. For this reason, materials and designed components possess an additional level of complexity (11). The high density supercritical carbon dioxide provides as a working fluid results in significantly more compact turbine and compressor wheels compared to other systems with power outputs of similar size (12). Increasing fabrication complexity is a result of engineering compact turbine and compressor wheels; however, this complexity is coupled with the positive result of decreased overall system size. Not only are the main components more compact, but, when compared to helium or steam producing the same power output, a cycle using CO₂ in the supercritical state requires a reduced number of stages (13).

Efficiency can be attributed to two main factors: temperature and fluid properties. In general, efficiency is calculated using the temperature difference between the hot flow entering the turbine and the cold flow entering the compressor. Additional increase in efficiency is predominantly a result of the thermo-physical properties of carbon dioxide in the supercritical state, and particularly near but above the critical point. Concentrated solar is capable of achieving temperatures in the 500-800°C range (10) (14). With cold side temperatures just above critical, 31.1°C, the temperature difference resides in the 468-768°C range (15). This temperature difference is consistent with high efficiency power cycles. To increase efficiency further, the focus turns to reducing compression work. Compression work is reduced as the thermo-physical properties of the fluid bring the compressibility factor closer to zero (12) (15). As carbon dioxide nears the critical point, while remaining in the supercritical phase, the compressibility factor is reduced to the range 0.2-0.5 (15). This can be achieved by both designing the heat rejection system in such a way to remove the desired amount of heat, and designing the operational pressure based upon the minimum system pressure point. Thus, the heat addition and heat rejection component/system designs are critical. For optimally sized systems with high temperature working fluid and effective heat rejection components, the SCO₂ Brayton cycle shows potential for greater efficiency advantage and, due to the smaller component size, a considerable reduction in capital cost (16). For operating conditions including a 550°C receiver temperature and a 20 MPa high pressure, a direct supercritical CO₂ cycle can achieve an efficiency of 45.3% and reduce capital costs by roughly 18% compared to a steam Rankine cycle with similar power output (17).

Valuable information for the effective design of an optimal solar receiver is provided by two methods for flux mapping on concentrated solar receivers, and both are described in the literature. Collado and Guallar (18) provide mathematical details for a cylindrical receiver. This method is based on an analytic function in Visual HFLCAL software, which was developed by the German Aerospace Centre and created for design optimization of heliostat and central receivers (19). The Collado and Guallar (18) method would require modification for use with a flat, single plane receiver design; however, the method

does provide mathematical techniques for calculating the power delivered by and optical efficiency of a heliostat or heliostat group. For calculating concentrated solar flux on single plane solar receivers, the photographic flux mapping method presented by Ho and Khalsa (1) is preferred. This method uses pixilated conversion of digital images to determine the flux on elements of the receiver that correspond to each pixel location. Angle of incidence for the camera is calculated in this method, a much more easy to obtain measurement than the heliostat angle of incidence required of the method for cylindrical receivers. Photographic flux mapping does require additional outside information, however, including the direct normal irradiance and the angle subtended by the sun at specific times, as well as filter attenuation required to obtain unsaturated images of the receiver area and the sun.

In addition to the aforementioned efficiency considerations, every component contributes to either efficiency gain or efficiency loss; and, each possesses its own challenges. The turbine and compressor wheels for SCO₂ Brayton cycles are typically small. Optimized for smaller power generation systems, they can be extremely small, between one and two inches in outer diameter (20), or less. Due to the limitations of Computer Numerical Control (CNC) machines, fabrication of these small wheels, especially radial compressor wheels, can become impossible. In these cases, sizing up must occur, causing efficiency losses. Data gained from upsized systems can be used in optimally sized models. Additionally, data collected from smaller experimental systems, as is the subject of this research, can be scaled to provide larger system performance estimations using Euler's equation (20).

Radial inflow turbines are being researched as the high efficiency configuration for smaller scale supercritical CO₂ Brayton cycles, cycles in the low kilowatt to 10 MW power range (21) (22). A radial inflow turbine, as opposed to its axial counterpart, provides the pathway necessary to achieve the previously discussed higher efficiency system with smaller component size. Single stage radial turbines have the capability to achieve 9:1 expansion ratios, significantly greater than axial configurations, which achieve approximately 3-4:1 expansion ratios (23). This difference is contributed to the geometric

configuration governing the inlet (U_2) and exit (U_3) blade speeds. In an axial turbine, blade speeds are essentially equivalent; in radial turbines, the inlet blade speed is faster. Faster inlet blade speed increases stage work per kilogram of mass, as shown by the following formula (23), where C denotes tangential velocity:

$$\text{Stage Work per kilogram Mass} = W_s = U_2 C_{w2} - U_3 C_{w3} \quad [1]$$

The main disadvantage to radial turbines is a single-stage limitation. Single stage systems tend to have lower pressure ratios which lead to lower total power outputs (21). However, lower power systems are the subject of current research with the goal of providing flexible, modular additions and alternatives to large power plants. These low kilowatt to 10 MW power systems include the UNLV system, which is the subject of this research, as well as other systems coupled with concentrated solar (10) (24) (25), natural gas, and small modular reactors (12) in the literature. In an effort to provide a solution to the single stage limitation, thereby increasing the total power output and efficiency of these smaller systems, the use of split-flow loops in the overall power cycle has gained popularity in recent research (15) (25).

Low pressure ratios given by radial turbines lead to coupling these turbines with centrifugal compressors. In fact, for power systems up to 2 MW, radial turbine and centrifugal compressor combinations can be fabricated on a single shaft (23). Centrifugal compressors have lower flow rate capacities, but offer significantly higher pressure ratios than their axial counterparts (26). Centrifugal compressors transfer energy from the wheel to the working fluid by an increase in fluid pressure, accompanied by increases in fluid temperature and fluid velocity (12). The amount of kinetic energy provided by the compressor wheel is determined by the number of impellers. This kinetic energy, again, is transferred to the working fluid; therefore, the number of impellers or blades designed for the compressor is essentially determined by the desired pressure ratio (26). Thus, turbomachinery optimization begins with the desired inlet and outlet conditions of the turbine and compressor (12). As

previously discussed, temperatures are chosen to be as high and low as are possible, within the limitations of material properties and the supercritical state of the fluid; and, the pressure is chosen to assure the lowest pressure in the system remains above critical. Average NIST (National Institute of Standards and Technology) values for the critical temperature and pressure of carbon dioxide are 31.062 °C and 7.368, respectively (27).

Additional efficiency gains can be achieved by incorporating recuperators into the Brayton cycle. When recuperators are compared to recompression loops in concentrated solar SCO₂ Brayton cycles, recuperators have been shown capable of dropping the temperature of the working fluid up to 35% prior to reaching the heat rejection component (28). This leads to the advantage of a much smaller heat rejection system and higher thermal efficiency. Zigzag and straight channel printed circuit heat exchangers are the subject of recent research for use as recuperators for SCO₂ cycles. Recuperators can contribute 60-70% of the total heat transfer in a SCO₂ power cycle. It is found that the channel size and flow are significant factors in the heat transfer capability of this type of heat exchanger with carbon dioxide. Using an ANSYS Fluent model, Printed Circuit Heat Exchangers (PCHE) with zigzag channels transfer the same amount of heat as the straight channel geometry with smaller size; however, the trade-off is a larger pressure drop. (29) Although the heat transfer capabilities of PCHEs provide significant improvements, components able to withstand the high temperature and pressure conditions of the hot side fluid in a SCO₂ Brayton cycle are a challenge. Thermal-hydraulic experiments of a XJTU minichannel PCHE with zig-zag geometry were successfully tested with 900°C helium as the working fluid, providing optimization data and proving the high temperature capability of this heat exchanger. (30)

Single flow and split flow cycles are merely the umbrellas under which there are many possible Brayton cycle configurations in the literature (31). Al-Sulaiman and Atif (31), Wang et al. (32), and Ahn et al. (15) each analyze and compare five and six single flow and six split flow cycle configurations: single flow recuperation, intercooling, reheating, inter-recuperation, pre-compression, and split

expansion; and, split flow recompression, modified recompression, preheating, and three turbine split flow configurations. Single flow recuperation is the simplest of the advanced cycles, and consists of a heater, turbine, recuperator, precooler, and compressor. This system, due to its simplicity, is often considered the reference system to which comparisons of more complex system configurations are made (32). Intercooling incorporates a second compressor in line with the first, and with a second precooler between them. Reheating is the simple recuperation cycle with a second turbine in line with the first, and with a second heater between them. Inter-recuperation is similar to the intercooling cycle, with a second recuperator in lieu of a second precooler. Pre-compression splits the recuperator in the recuperation cycle into two, a high temperature and low temperature recuperator, with a second compressor, a precompressor, in between; the outlet of the main compressor flows through both recuperators in series. Split expansion is the recuperation cycle with a turbine both before and after the heater. Six split flow configurations are compared to these single flow configurations, each having a different number of components or a different flow path.

After a thermodynamic analysis using a heliostat solar power tower, Al-Salaiman and Atif (31) found the recompression Brayton cycle to display the highest overall efficiency, at 52%, 40% considering solar receiver loss. They also noted that the recuperation cycle fared close to this efficiency, creating more power with the same mass flow rate when direct normal irradiance was lower. Ahn et al. (15) concurred, noting specific work comparisons were not completed and may result in different configuration favorability, particularly with bottoming cycle applications which convert waste heat to power. Wang et al. (32) found that maximum specific work resulted from the recuperation cycle with minimum pressures, pressure at the compressor inlet, in the pseudo-critical range, around 8.2 MPa; however, pressure increases beyond 8.2 MPa resulted in progressively decreasing specific work output. Additionally, they concluded that reheating did not add value when the turbine inlet temperatures are high. After testing turbine inlet temperatures up to 800 °C, they found the highest efficiency values with turbine inlet temperatures around 650 °C. Garg et al. (33) concurred, concluding that highest efficiencies

for the supercritical CO₂ Brayton cycle occur with a turbine inlet temperature of 600 °C and a compressor inlet pressure of 8.5 MPa.

When an SCO₂ cycle is integrated into a solar power generation system, transient conditions due to cloud coverage and other interruptive weather conditions must be considered. The transient nature of the natural environment poses concern and consequences in solar power generation systems. Although the degree of consequence to a SCO₂ Brayton cycle by transient cloud coverage in nature is not fully known, Iverson, et al. (24) experimentally found that short term transients have little effect on system functionality. Longer term decreases in energy input may be minimized with the addition of a short term storage unit (24). This behavior and modification may also be extended to short-term nuclear reactor shut-down and maintenance operations in systems that utilize SCO₂ Brayton cycles.

Models of the SCO₂ Brayton cycle with both nuclear and concentrated solar power generation systems demonstrate the feasibility of integrating this power cycle with these moderately high to high temperature heat sources. These models may be completed using numerical modeling or equation solver software, where the former is more common for single components and the latter for multiple component systems. Engineering Equation Solver (EES) is a software program with embedded NIST (National Institute of Standards and Technology) thermo-physical property data for carbon dioxide in all states. This eliminates both the need for interpolation and the error resulting from interpolation of supercritical carbon dioxide properties (34), as the properties near the critical point and in the pseudo-critical temperature range change drastically with small changes in temperature for each pressure point (35). EES solves systems of equations mathematically based upon Newton's method, while calling fluid properties with two known values, such as temperature and pressure (34).

Fluid properties determined using EES are also used to calculate dimensionless parameters and the heat transfer coefficient for CO₂ in the pseudo-critical and supercritical states. The changing temperature and pressure throughout the system, as well as the mechanism for heating and cooling impact the heat

transfer coefficient in different areas of the system. Since using supercritical CO₂ as a working fluid has gained popularity, so has improving correlations leading to proper heat transfer coefficient predictions. The heat transfer coefficient greatly determines the convective heat flux, which is particularly important for the design of the recuperator and the air cooled heat exchanger. The most widely used correlation in the literature is the Dittus-Boelter correlation for heating or cooling fluids in a smooth pipe under turbulent flow conditions (36):

$$\text{Nu}_{\text{heating}} = 0.0243 \text{ Re}^{0.8} \text{ Pr}^{0.4} \quad [2]$$

$$\text{Nu}_{\text{cooling}} = 0.0265 \text{ Re}^{0.8} \text{ Pr}^{0.3} \quad [3]$$

The equation was originally presented by Nusselt; however, Dittus and Boelter are credited with the advancement of the coefficients, and are therefore credited with this common version of the correlation (36). New correlations are typically compared to the Dittus-Boelter correlation. As discussed, carbon dioxide behaves in a hyperresponsive manner near the critical point. This has prompted researchers to both evaluate the heat transfer correlations previously used and examine better possible solutions for characterizing the heat transfer behavior of SCO₂ as it flows through particular paths and specific components in the SCO₂ Brayton cycle. Hasan and Farouk (37) determined that the hyperresponsive and divergent behavior SCO₂ exhibits is demonstrated from critical pressure up to 10 MPa, where the behavior of the fluid becomes much more predictable. Furthermore, below 10 MPa and near the critical point, bulk viscosity cannot be assumed negligible, particularly in cycle locations undergoing compression, density spikes, and thermal diffusivity is between 170 and 3000 times slower than below critical temperatures (37).

Many correlations have been developed and determined more accurate by researchers experimenting under specific conditions. Reviews of the Dittus-Boelter and new correlations using comparisons to

specific experimental conditions are also described in the literature. In many cases, this experimental comparison has led to the development of these new correlations. Oh and Son (38) developed a heat transfer coefficient correlation for cooling supercritical CO₂ in macro-tubes. Liao and Zhao (3) determined another correlation for cooling in mini and micro tubes with flow diameters between 0.50 mm and 2.16 mm. Duffey and Piro (39) evaluate 41 different correlations for use with both carbon dioxide and water, listing the operating pressure, temperature, flow geometry, and flow regime each is designed to describe. In another correlation analysis by Lin et al. (40) found the Dittus-Boelter correlation to fall short in predicting cooling of supercritical CO₂. The Dittus-Boelter correlation is determined to provide insufficient weight to the vast change in density around the critical and pseudo-critical regions of SCO₂ (41). For these reasons, the Yoon et al. (41) correlation, which incorporates a density term into the Dittus-Boelter correlation, is found to predicting the heat transfer coefficient for supercritical carbon dioxide cooling in tubes well (40), with an average deviation of 12.7% (41). Based on a considerable review of the literature, the Dittus-Boelter correlation is most likely to properly describe the heat transfer behavior of SCO₂ farther away from the critical point, and Yoon et al. better describes SCO₂ heat transfer behavior near the critical point and in the pseudo-critical region.

CHAPTER 3. SYSTEM DESIGN

Supercritical carbon dioxide Brayton cycle systems are present in the research and development, however are not yet commercial. Thus, many of the necessary components are not available for purchase. The scope of this research is to design, develop, and fabricate new system-specific components and repurpose components in the development phase. These components are then combined with commercially available, non-system-specific components to create an experimental SCO₂ Brayton cycle for the SAIC dish concentrator on the UNLV campus. In the design process, primary safety measures are given to high expected temperatures and pressure. Material temperature is expected to reach levels in the vicinity of 1000 °C and system pressure is modeled for a 22 MPa maximum.

The main components and the placement of each in the integral SCO₂ system design are displayed in Figure 1. The design, fabrication, and experimental testing of each of these components are the primary focus of this research. Of these components are custom; and, all except the recuperators are fabricated on campus, at the UNLV Center for Energy Research and the UNLV Machine Shop. The recuperators, which are the subject of international research collaboration, are products of the Key Laboratory of Thermo-Fluid Science and Engineering at Xi'an Jiaotong University in China.

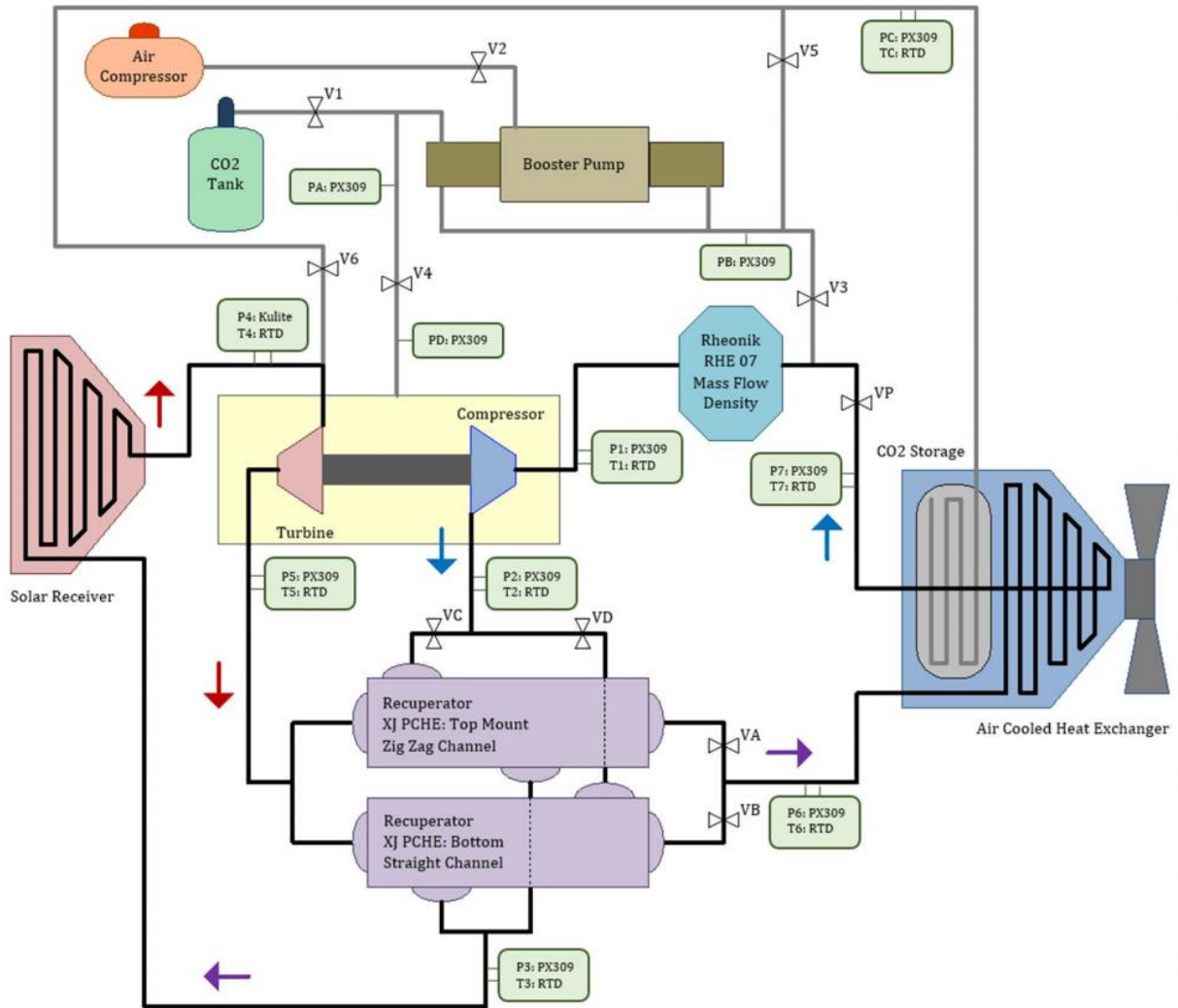


Figure 1. UNLV Supercritical Brayton Cycle Full System Design

3.1 Solar Receiver

The solar receiver is designed based upon and limited by the solar concentration area dimensions of the SAIC dish concentrator. The overall concentration area measures 1 m square. Evaluation of the solar flux distribution provides solar receiver design optimization information. Photographic Flux Mapping (1)

is the method used for determining the flux distribution. This method uses on-sun digital images. The SAIC dish concentrator operating under on-sun conditions is displayed in Figure 2.



Figure 2. SAIC Dish On-Sun Testing

The Ho and Khalsa method for photographic flux mapping (1) requires high resolution digital images of the sun and the receiver area, the direct normal irradiance at the time of image collection, and the reflectivity of the receiver. Gray-scale images of the sun and the concentration area were collected during on-sun operation using a high resolution, Nikon D3100 camera, having a 55 mm focal length, with neutral density filters. Neutral density filters are used to decrease the amount of light entering the camera without altering the image. A combination of Hoya neutral density filters was used for each image to optimize exposure. The image of the sun required two Hoya ND8 and one ND4 filters, providing optical densities of 0.9 and 0.6, respectively. To properly collect the receiver image, the filter combination was reduced to two ND8 filters, providing an optical density of 0.9 each. The total optical density per image is given by simply adding the optical densities provided by each filter in the respective combination. Therefore, the expected total optical density is 4.2 for the sun image and 1.8 for the receiver image. These expected optical densities were tested with a spectrometer to ensure accuracy. The spectrometer is used first to measure the sun without filters, then with each filter, separately, to determine the actual optical density of each individual filter. The spectrometer determined the total optical density to be 4.5929 for the filter combination used to collect the sun image and 1.9830 for the combination used to collect the receiver image. The resulting sun and receiver images, using the described filters, are displayed in Figure 3 and Figure 4, respectively.



Figure 3. Image of the Sun using 4-ND8 and 1-ND4 Filters



Figure 4. SAIC Dish Collection Area Reflective Collection Image using 2-ND8 Filters

Systematic pixel conversion of the sun image in Figure 3 is completed by first assigning a 16 bit value to each pixel. This is, therefore, a number from zero to 65,535, where black is zero and white is 65,535. A scale using this range is chosen to optimize the signal to noise ratio. Each pixel value is then converted into a relative irradiance value that yields a pixel summation equal to the direct normal

irradiance collected by a pyranometer at the time of image collection. Figure 5 is the resulting pixel conversion of the sun image, with each pixel displaying a color-coded value corresponding to a portion of the total direct normal irradiance (DNI) at image collection, 990.154 W/m².

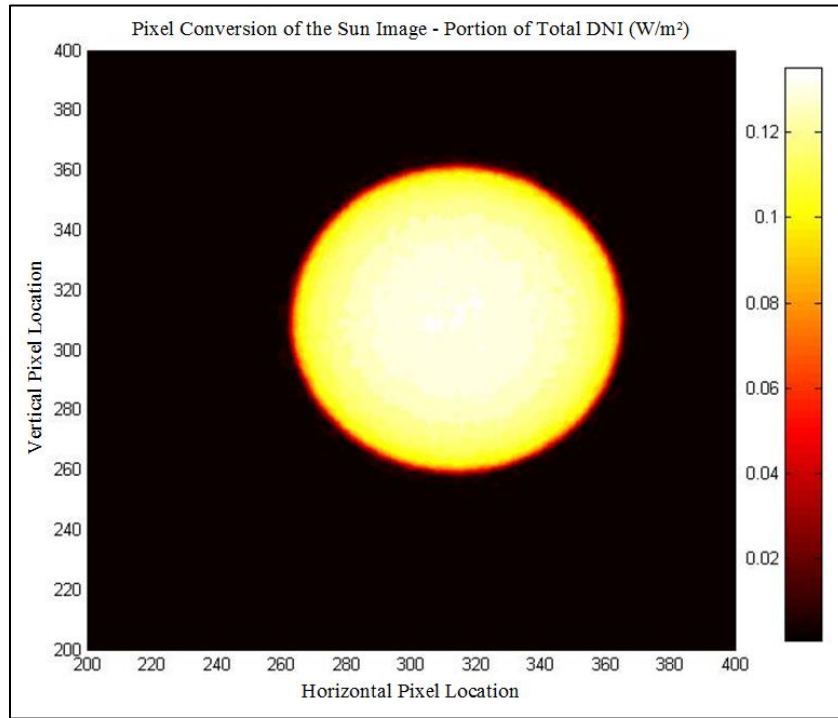


Figure 5. Sun Image Pixel Conversion

A Matlab script is created to calculate the flux map of the receiver area, based upon equations and methodology provided by Ho and Khalsa (1). The overall equation is as follows:

$$E_{R,i} = \frac{V_{CCD,i} E_{DNI}}{\rho_{R,i} \tan^2(\gamma_{sun}/2)} \frac{\pi r_{Sun_Pixels}^2}{\sum_{Sun} V_{CCD_{Sun,i}}} \frac{f_R}{f_{Sun}} \quad (W/m^2) \quad [4]$$

$$f_R = 10^{(\text{Receiver Image Total Optical Density})} = 10^{1.9830} \quad [5]$$

$$f_{\text{Sun}} = 10^{(\text{Sun Image Total Optical Density})} = 10^{4.5929} \quad [6]$$

$$\gamma_{\text{sun}} = 2\arctan(\text{radius of the sun/target angular diameter}) \quad [7]$$

The digital response due to background in this equation is negligible due to the position of the receiver during on-sun operation, thus it is omitted. During operation, and image collection, the receiver is facing exactly away from the sun, shaded from a significant level of irradiance compared to the concentration of the system. Furthermore, the main focus of this procedure is to determine the optimal size and provide design considerations for the custom receiver, making this small amount of error inconsequential.

The script requires the user to input the desired sun image and the desired receiver area image with specified labels. The images are converted to 16 bit gray scale images. The derivative of each individual pixel in the sun image is calculated to isolate those pixels making up the sun. Sun pixel normalization filters pixels with low value derivatives to determine the edge of the sun within the image. The result is used to determine the sun pixel radius, center point, and area.

The angle subtended by the sun, γ , is found by using the distance from the sun at the time of image collection. This information is provided by the NASA Jet Propulsion Laboratory Horizons System (JPL Horizons) (42). JPL Horizons is a data and ephemeris service which provides calculated positions of orbiting objects in the solar system using a high-precision Earth Orientation Parameters model. A date and time range, around that of image collection, is entered, along with a requested data step size of one minute. The observation location is entered as the location at the UNLV Center for Energy Research (UNLV CER), 115°08'39.6''W and 36°06'51.1''N at 2025 ft. Target angular diameter output, in

arcseconds, is set to use the date and time corresponding to the minute the sun image was collected. The radius of the sun is estimated to be 6.96E5. The angle between the camera and receiver normal is calculated by simple trigonometry using measurements taken between the camera and receiver area.

The reflectivity of the receiver can be found by using the methodology described by Ho and Khalsa, by using back to back pyranometers, or by comparing the reflectivity of a known material. The latter is used in this case. Ceramic material with a reflectivity of 0.8 is attached to the receiver area and an image is collected. The collected image shows both the ceramic material and the bare insulation behind the image, as shown in Figure 6. The materials are compared in pixel conversion, providing a light reflectance ratio between the ceramic and the bare insulation to the right of the ceramic material. This ratio and the known reflectance of the ceramic are used to calculate the receiver area reflectance, averaged as uniform, per the equation below. The resulting value is in the range of light rock ground reflection measurements taken at the UNLV CER via back to back pyranometers, as expected for this type of material.

$$\rho_{R,i} = \text{Refelctance Ratio} * \text{Ceramic Reflectance} = 0.788 * 0.8 = 0.63 \quad [8]$$



Figure 6. Receiver Reflectance Ratio Image Collection Arrangement

All of these parameters are entered into the receiver area flux map Matlab script. The pixel values are converted into a value corresponding to the solar radiation flux density incident on the pixel area. The resulting image, color coded to differentiate levels of irradiance, describes the solar flux distribution incident on the solar collection surface as displayed in Figure 7.

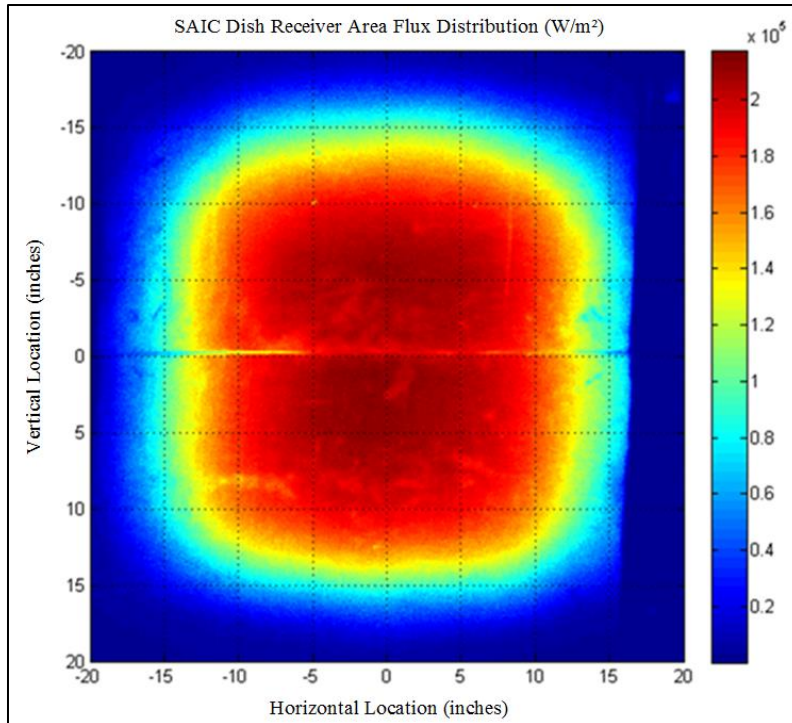


Figure 7. SAIC Dish Receiver Collection Area Solar Flux Distribution

This resulting solar flux distribution provides both the maximum concentration ratio achieved on a clear day, and solar receiver design dimension optimization insight. As shown in Figure 7, the beam is nearly centered within the solar concentration area in a rounded square pattern, achieving a solar flux of over $2E5 \text{ W/m}^2$ from the center to approximately 10 in (0.25 m) vertically and 8 in (0.20 m) horizontally. The intensity decreases concentrically until reaching a one sun effective equivalent between an approximate 14 to 16 inches (0.33 to 0.41 m) from the center point. The lower flux line shown horizontally across the center of the collection area is the seam in the high temperature insulation material that covers the entirety of the concentration area.

It is desirable for the solar receiver to cover the entire concentration area for maximum gain; however, optimization requires consideration of additional parameters. Radiation spectra along the near

central horizontal and near central vertical cross sectional lines of the receiver area are evaluated to provide more distinct solar mapping information for design size optimization. The near central location is expected to have a slightly lower maximum flux concentration; however, an off-center cross section is expected to avoid the seam in the receiver material, thus reducing larger material discrepancies and larger dips in the results. Slight increases and decreases are typical of solar radiation spectra. Larger dips are attributed to inconsistencies or seams in the receiver material. The resulting data are displayed for the horizontal cross section in Figure 8 and for the vertical cross section in Figure 9. Zero is the center point of the receiver area, corresponding to the central pixel location. Horizontally and vertically the data show a platykurtic Gaussian distribution. Taking a closer look, the data show a slightly negative, or left side, skew in both cross sections. A negative skew in the vertical direction is described by a downside skew in the overall receiver area. This means the central location of the concentration beam has a negative skew in both the vertical and horizontal directions. The skew is due to error in solar tracking. The SAIC dish concentrator tracks the sun using a connection to the Epply Normal Incident Pyroheliometer (NIP) located on the roof of the UNLV CER. The NIP has a typical accuracy of within 1%; however, the SAIC tracking mechanism adds error to this expectation.

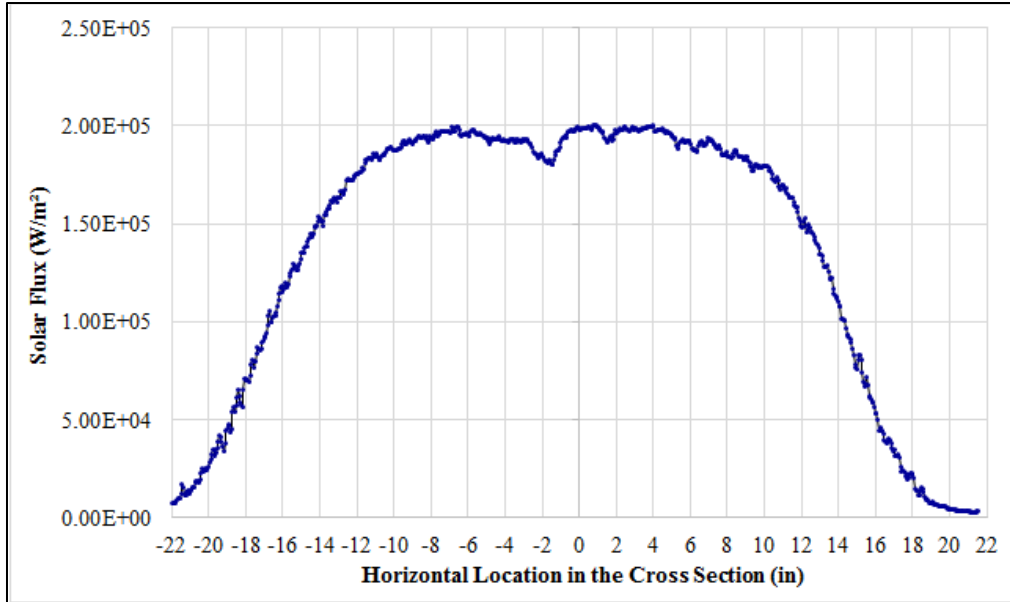


Figure 8. Solar Flux along a Horizontal Cross Section of the Receiver Area

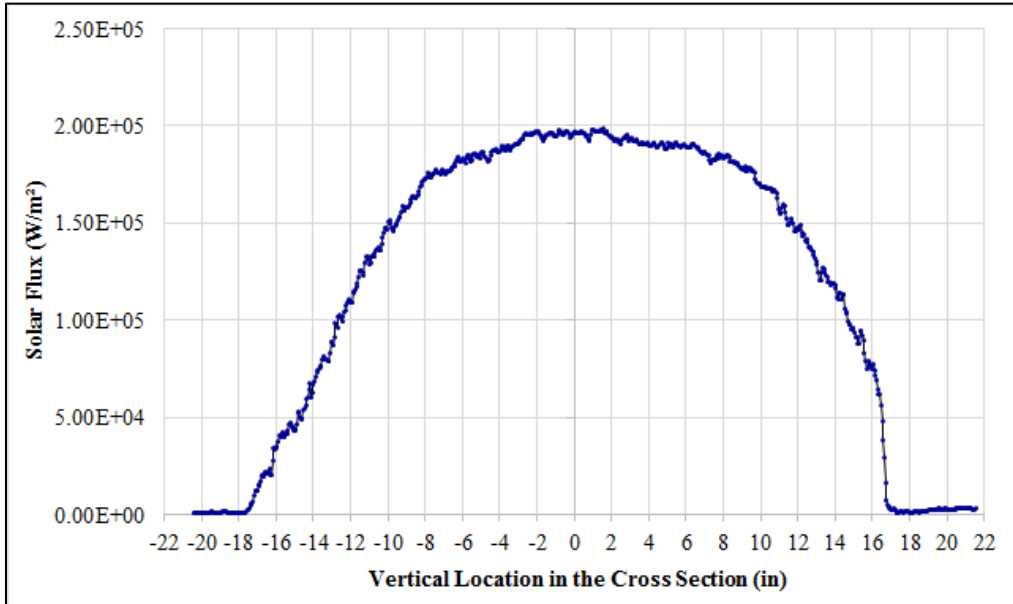


Figure 9. Solar Flux along a Vertical Cross Section of the Receiver Area

Cross section distributions are used to determine the optimal size for the final design of the solar receiver. The standard deviation is 70658.17 W/m² over the horizontal cross section and 74490.72 W/m² over the vertical cross section. These correspond to approximate horizontal and vertical locations on the receiver area, as displayed in Table 1. Approximate locations were determined based on their correspondence to critical values for one, 1.5, and two standard deviations.

Table 1. Statistical Analysis of the Horizontal and Vertical Cross Sections

Cross Section	Horizontal		Vertical	
Standard Deviation (W/m²)	70658.17		74490.72	
Median (W/m²)	176808.84		150951.45	
Deviation	1 σ			
Value	106150.67		76460.73	
Approximate Locations (in)	-16.3	14.1	-13.6	15.9
Average Location (\pm)	15.0			
Deviation	1.5 σ			
Value	70821.58		39215.37	
Approximate Locations (in)	-18.1	15.4	-15.8	16.6
Average Location (\pm)	16.5			
Deviation	2 σ			
Value	35492.49		1970.01	
Approximate Locations (in)	-19.6	16.9	-17.6	17.7
Average Location (\pm)	17.9			
Kurtosis	-0.993		-1.272	
Skew	-0.800		-0.595	

The average kurtosis for the receiver area, calculated in Excel by Equation 9, is -1.13. The kurtosis describes the platykurtic nature of the Gaussian distributions shown in Figure 8 and Figure 9. The skew, again, describes the amount horizontally and vertically off-center the center of the concentrated beam is from the center of the receiver area. These indicate that the beam is close to centered and, with shorter

distribution tails, the concentrated irradiance is flatter and drops off more quickly than a standard Gaussian distribution. Both provide valuable information for the design of the solar receiver.

$$\text{Kurtosis} = \frac{\sum \left(\frac{y - \bar{y}}{\sigma} \right)^4}{n} - 3 \quad [9]$$

Given both horizontal and vertical skews are between -2 and 2, it is statistically reasonable to assume the concentrated beam is centered for design purposes. Overall fabrication design diameter for the solar receiver is determined based on this and the standard deviation of the solar flux on the receiver area. Choosing a diameter consistent with two standard deviations is ideal, statistically covering 95% of the solar flux. This is a radius of 17.9 in and a diameter of 35.8 in. This value leaves an extremely small margin between the receiver and the edge of the mountable receiver area, a margin smaller than will allow a tube inlet at the outer diameter location when centered. The tube inlet is routed through the receiver area base, from the interior side of the package. There must be compensation for the structural rails, which remove otherwise allowable through-routing inches. For this reason, the one sun effective equivalent outer diameter estimation, shown in Figure 7, is considered. This estimates a radius of 16 in, or a diameter of 32 in. This value is just less than 1.5 standard deviations.

In the transition between data analysis and solar receiver fabrication, fluid flow, pressure drop, and ease of manufacturing are additional considerations. The receiver area flux distribution analysis shows a rounded square geometry; therefore, this geometry is considered. Fluid flows more freely in circular tubes than in tubes with square geometric paths, and fabricating concentric circles comes with greater ease than do concentric squares; therefore, circular geometry is also considered. Furthermore, pressure drop increases as tube length increases; thus, it is important to determine an optimal size that corresponds to minimal power loss, without oversizing the component. To establish power loss as a function of geometry and size, the efficiency report provided by SAIC, analyzing dish performance coupled with ideal receiver

units of different sizes, is used. These data are compared to varying radii and square side dimensions of receivers with round and square design geometries. The data comparison is analyzed up to a 16 inch half length; this is based upon the approximate one-sun outer perimeter resulting from the SAIC dish receiver collection area solar flux distribution analysis, Figure 7, and the flux spectra, Figure 8 and Figure 9. The resulting comparison, described in Figure 10, shows that a square receiver with a 15 inch square side half length, or that is 30 inches square, would result in negligible power loss compared to the expected efficiency the SAIC dish provides. Power loss is greater with a circular design of equivalent half length, as expected, due to geometric corner loss. At the 15 in effective equivalent efficiency for the square geometry design, the circular design is expected to experience a 20% power loss. At the one-sun perimeter half-length estimation of 16 inches, the circular design power loss expectation decreases by half to 10%.

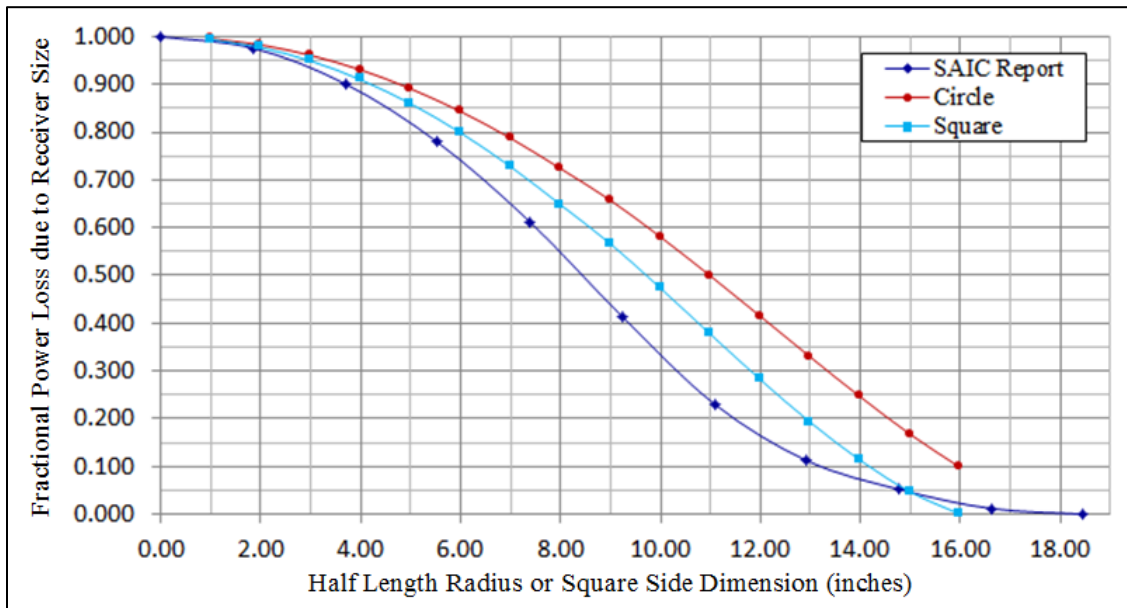


Figure 10. Fractional Power Loss as a Function of Receiver Design Size

Based upon the data collected and ease of fabrication, a circular geometry with a 16 inch radius is determined to be optimal. Given heat transfer behavior, greater surface area effects greater heat transfer, thus a stacked design is considered over a planar design to maximize this parameter. Thus, the final solar receiver design is a conical spiral with an overall diameter goal of 32 in.

Based upon the flux results, receiver material temperatures may reach up to 1000 °C or more; thus, tube material is chosen accordingly. Inconel provides extreme temperature tolerance, however is very difficult to manipulate. For this reason, thick wall stainless steel (SS) 316 is chosen. Swagelok SS 316 tube with outer diameter 0.5 in (12.7 mm) and wall thickness 0.083 in (2.11 mm) meets the temperature requirements and provides a standard pressure rating of 6700 psig (46.2 MPa). Accounting for 1000 °C temperature degradation, 76% of the standard value, the tube maintains a pressure rating of 5092 psig (35.1 MPa).

Bending tube of this diameter to thickness ratio cannot be done by hand; and, a typical tube bender is designed to create angles and elbows, not spirals. A custom bending tool is designed and fabricated to complete the task. The custom bender is capable of bending the tube in spirals with adjustable radii. A photograph of component fabrication using the UNLV Custom Radii Tube Bender tool is shown in Figure 11. This tool is used to create the predominant shape of the receiver, which is then secured using stainless steel wire, inset in a cylindrical housing of aluminum, and wrapped in insulation, producing the final product shown in Figure 12.



Figure 11. Component Fabrication using the UNLV Adjustable Radii Tube Bender Tool

(Workers shown are Roy Lookingbill and Danielle Nobles-Lookingbill.)



Figure 12. Solar Receiver

Figure 13 is a backside view of the solar receiver. In this view, the expansion loops are visible. These expansion loops serve two purposes: they are a method of connecting tube lengths, but also allow for expansion of the material under extreme heat conditions. The tubes shown in perpendicular orientation to the spiral tubes provide structural support and do not house flow.

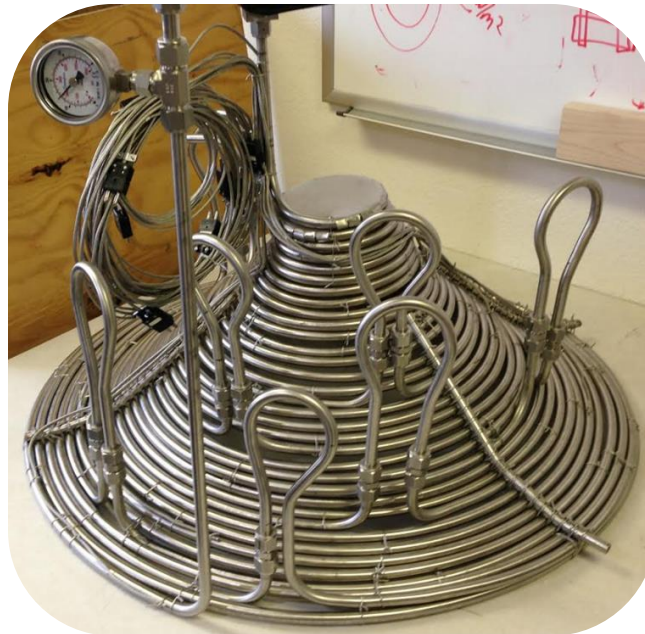


Figure 13. Backside View of the Solar Receiver

The final, fabricated, solar receiver is an overall 32.5 inches in diameter. Calculations establishing the percentage of the concentrated solar flux captured by the UNLV solar receiver are displayed in Table 2. As expected, the average critical value is just under 1.5 standard deviations at 1.424. The percentage of concentrated solar flux captured in the horizontal and vertical directions are found by using standard charts for calculating the critical probability from the critical value. Due to the platykurtic nature of the distribution and the normal distribution assumed in the critical value charts, these are likely minimum

estimations. Therefore, the minimum overall average percentage of the concentrated solar flux captured by the UNLV solar receiver is 81.5%.

Table 2. Percentage of the Concentrated Solar Flux Captured by the UNLV Solar Receiver

Horizontal Location	Critical Value	% from Median	Total %
-16.26	0.957	33%	79.9%
16.26	1.859	47%	
Vertical Location			
-16.26	1.751	46%	83.0%
16.26	1.128	37%	
Average:	1.424		81.5%

After on-sun testing, a flux distribution is displayed in the receiver material by means of differential temperature effects on stainless steel. The pattern reflects the results visible in the photographic flux mapping data. This is evident in a visual comparison of Figure 12 to Figure 7. The lack of significant color change in the outer two rings of the solar receiver provides evidence of design optimization success. This shows that the UNLV solar receiver does, in fact, encompass the receiver area with the greatest solar concentration.

3.2 Air Cooled Heat Rejection Heat Exchanger

The air cooled heat rejection heat exchanger (ACHEX) is designed to remove all of the heat accepted by the solar receiver. Although losses are expected, the goal is to reach a gas temperature as close to ambient as possible. Sizing of the ACHEX is estimated by an Engineering Equation Solver (EES) model. Once size is determined, it is decided that a circular spiral shape may provide a condensed design with decreased fluid friction losses compared to other designs. Additionally, this circular spiral shape will allow additional rings to be added, if needed, with ease. The custom bending tool fabricated for the solar

receiver is used to construct the ACHEX shown in Figure 14. Connections made between tube lengths are combined with expansion loops to allow flexibility in the component as well as to achieve the tube length required to reach the heat rejection goal.



Figure 14. Air Cooled Heat Rejection Heat Exchanger

3.2.1 EES Design Code for the Air Cooled Heat Rejection Heat Exchanger

A code based upon the effectiveness NTU method was written in two forms. One of these required a user defined desired outlet temperature to generate the length of tube required to reach that outlet temperature. The other requires a user defined tube length and determines the outlet fluid temperature. It is found that different formulas must be used for each type in order to provide a useful result. The second code is embedded in the Engineering Equation Software (EES) general system code. The maximum tube lengths provided by Swagelok are 20 ft (6.1 m). The original code estimated the need for slightly less than 21 m to reach the desired outlet fluid temperature of ambient. It was decided that 24 m would be used, in order to maximize heat rejection and tube length. When modeled with a 24 m input heat rejection tube

length, it is determined numerically possible to achieve outlet fluid temperatures around 21 °C. This value is experimentally limited by the actual ambient air, or cooling fluid, temperature during system operation. The finalization of the EES code is one of the goals of this doctoral research, as discussed in Chapter 4 of this document.

3.3 Recuperator

A recuperator is used to recuperate heat from the hot flow, upon turbine exit, to the cold flow, upon compressor exit, in an effort to reduce the work required to achieve the desired temperatures of both the hot and cold flow paths. In order to maximize positive heat exchange, mini and micro-channel heat exchangers are preferred. Xi'an Jiaotong University in China is developing a printed circuit mini-channel heat exchanger (XHEX) capable of withstanding fluid temperatures up to 450 °C. In collaboration with Dr. Qui-wang Wang, Dr. Ting Ma, Dr. Wenxiao Chu, and their research team at Xi'an Jiaotong University, two of these heat exchangers were custom fabricated for the UNLV supercritical carbon dioxide Brayton cycle, and were purchased by UNLV. Of these, one houses straight channel geometry, and the other houses zig-zag channels. The zig-zag channel XHEX is displayed in real and computer generated views in Figure 15 and Figure 16, respectively.



Figure 15. Xi'an Jiaotong University Printed Circuit Mini-Channel Heat Exchanger

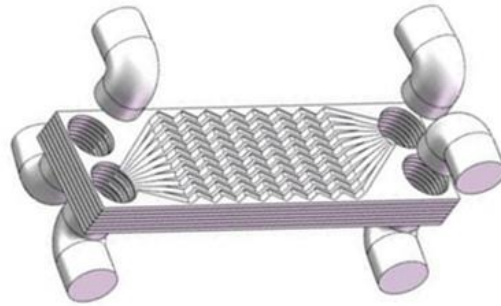


Figure 16. Zig-Zag Channel XHEX

3.3.1 Recuperator Design Considerations

Dr. Wenxiao Chu was the point of contact for the Xi'an Jiaotong University (XJTU) research team with regard to the majority of the recuperator design decisions. The preliminary parameters given to the XJTU team were based on a preliminary UNLV EES model. These starting point design parameters are displayed in Figure 17, with a mass flow rate of 0.16 kg/s. Though this mass flow rate has been determined low, it was part of an original set of parameters based upon various systems in the literature of similar size.

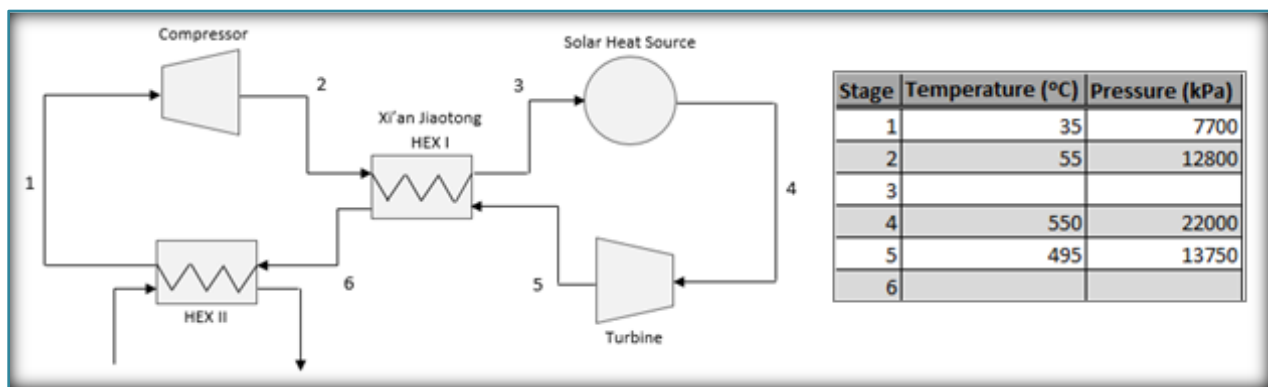


Figure 17. Preliminary Recuperator Design Parameters

Original heat transfer calculations were estimated by Equation 10. Given the preliminary design conditions, the heat transfer goal was calculated to be approximately 82 kW. Upon investigation and analysis between the two research teams, the temperature at stage two in Figure 17 was increased to 217.9°C. This increase in low temperature reduced the heat transfer goal to 55 kW for the recuperator. Upon inverse analysis by Dr. Wenxiao Chu that showed a discontinuity in cold outlet temperature, it was determined that a reliable heat transfer design goal for the printed circuit minichannel heat exchanger (XPCHE) is 35 kW. Thus, the XPCHE is designed to provide 35% recuperation for the 100kW system.

$$Q = \dot{m}C_p\Delta T \quad [10]$$

Numeric modeling completed by Dr. Wenxiao Chu and the XJTU research team provided the results for each XPCHE, as displayed in Table 3. These results determined the overall size of each XPCHE at the 35 kW design point. As designed, each XPCHE is expected to achieve an 83.1% thermal efficiency. The final design material is SS-316L, and each XPCHE has been pressure tested to 13.5 MPa by the XJTU team. Each XPCHE is also designed to receive hot side inlet temperatures of 495°C without degradation.

Table 3. XJTU Numerical Design Parameters for the XPCHE

Parameter	Straight Channel XPCHE	Zig-Zag Channel XPCHE
T _{in,hot} °C	495	
T _{out,hot} °C	311.8	
T _{in,cold} °C	218.2	
T _{out,cold} °C	403.1	
ΔP (hot side) kPa	0.8	2.1
ΔP (cold side) kPa	0.89	2.44

3.4 Turbomachinery Design

The turbo-compressor is the most complicated of the system components to design and fabricate. The turbo-compressor component was first completed in SolidWorks, where plate thicknesses are modified to assure proper placement of elements for subtractive manufacturing. The SolidWorks files are then converted to Mastercam computer automated design and manufacturing software files for fabrication.

3.4.1 Sonic Speed and Mach Number

In the design of the turbine and compressor impellers, the first consideration is given to the Mach number for the fluid. Due to the shock that occurs when fluids transition between supersonic to subsonic velocities, sonic velocity is avoided in the turbomachinery design. The sonic speeds for gases vary, and are typically computed by the following formula:

$$c_{\text{CO}_2}(\text{m/s}) = \sqrt{\frac{\gamma R(\text{J/mol K})T(\text{K})}{M(\text{kg/mol})}} \quad [11]$$

Carbon dioxide is not described by ideal gas parameters, specifically near the critical point. The thermophysical properties needed to calculate sonic speed, as well as sonic speed itself, must be determined for four main design points, compressor inlet, compressor outlet, turbine inlet, and turbine outlet. The estimated pressure and temperature values at these locations in flow are based on the combination of desired outcome and data published by Sandia National Laboratory on a similar system. Wright et al. (22) report approximately 32.0°C and 7.690 MPa at the compressor inlet, 48.9°C and 13.842 MPa at the compressor outlet, 536.9°C and 13.498 MPa at the turbine inlet, and 475.9°C and 7.886 MPa at the turbine exit of the Sandia National Laboratory supercritical carbon dioxide Brayton cycle. Operation just above the critical point can be difficult to maintain during system operation (43). A slightly

higher temperature and pressure is used as the design point, shown by Cho et al. (43) as a means to maintain system stability. The preliminary minimum design pressure for the UNLV system is 8.0 MPa, a design point providing a slightly larger margin to assure initial operations maintain the supercritical state of the fluid. This is slightly higher than the Sandia system and slightly higher than optimal to take advantage of the peak heat transfer properties nearest the critical point; however, this pressure is under the 8.2 MPa threshold for maximum specific work output found by Wang et al. (32).

Few single sources provide thermophysical property data for CO₂ under all four design points. Much of the research in the literature provides insight on a specific pressure and temperature region of interest to the particular research team. National Institute of Standards and Technology (NIST) provides data across the spectrum; however, access to this information is costly. Therefore, the literature is the first reference for these data, followed by free online resources, then by Engineering Equation Software (EES), which is also costly, but references the NIST database while providing other software capabilities.

Donna Price (44) (45) published two journal articles documenting thermal properties of carbon dioxide as a function of temperature and pressure, 100°C to 1000°C and 50 bars to 1400 bars, respectively. These values are used to calculate the sonic speed of carbon dioxide at expected temperature and pressure values corresponding to the turbine inlet. Thermophysical properties for temperatures from below ambient to 750 °C and pressures up to 10 MPa are calculated by the MegaWatSoft, Inc. online access calculator (46). These values are considered for the turbine exit and compressor inlet design points. These MegaWatSoft, Inc. data are compared with NIST data and are within an expected margin of error, with the exception of density and specific heat at the compressor inlet. At this design point, MegaWatSoft Inc. records a density of 1075.25 (kg/m³), where NIST reports 419.2 (kg/m³). MegaWatSoft, Inc. reports a 1.653 kJ/kg K isobaric specific heat, where NIST reports 29.61 kJ/kg K. Given that NIST is, by reputation and name, revered the standard for these types of data,

NIST values are used where there are significant discrepancies in data. Further, data voids in the literature are given by EES, which references the NIST database.

The sonic speed of CO₂ is known to measure highest far away from the critical point, exponentially decreasing toward the critical point (47). This yields the design points defining the minimum and maximum sonic speed for the system. The minimum sonic speed occurs at the compressor inlet, and the maximum sonic speed occurs at the turbine exit. The behavior of the fluid near and above the critical point does not follow the simplified sonic speed equation, Equation 11. This is due to the sensitive phase state changes which rapidly occur with very small changes in temperature and pressure. At temperatures near and above critical, velocity is greatly influenced by pressure. Experimental measurements by Han et al. (47) are described in a velocity/pressure curve for 35°C fluid over a pressure range from 7 MPa to 13 MPa. These data show a minimum velocity of approximately 180 m/s occurring at 8 MPa for 35°C fluid. From 8 MPa, decreasing to 7 MPa the velocity increases to approximately 210 m/s; the velocity also increases in a concave manner as pressure increases beyond 8 MPa. Han et al. attribute much of this behavior to an extreme decrease in density during the liquid to gas phase transition due to decreasing pressure. The change in density most strongly governs velocity from critical pressure to 8 MPa; however, as pressure increases beyond 8 MPa, velocity is governed more strongly by significant increases in bulk modulus occurring with increasing pressure from critical. For these reasons, near the critical point, simplified equations for sonic velocity do not apply; and, experimental data or differential and more complex equations must be used for sonic speed calculations. The mass balance equation for a steady flow process, shown in Equation 12, provides a more comprehensive method for calculating sonic velocity in a steady flow process.

$$\rho A c = (\rho + d\rho) A (c - dV_f) \quad [12]$$

The Redlich-Kwong-Soave equations of state (RKS EOS), shown in Equations 13-17, provide, with accepted accuracy, descriptions of the thermophysical properties of fluids in both the liquid and vapor phases, leading to better results for supercritical fluid. These equations can be expanded to the partial differential equation for sonic velocity with constant entropy given in Equation 18.

$$P = \frac{RT}{(v - b)} - \frac{a(T)}{v(v + b)} \quad [13]$$

Where,

$$b = 0.08664 \frac{RT_c}{P_c} \quad [14]$$

$$a(T) = 0.42748 \frac{(RT_c)^2}{P_c} \left(1 + m(1 - \sqrt{T_r})\right)^2 \quad [15]$$

$$T_r = \frac{T}{T_c} \quad [16]$$

$$m = 0.480 + 1.574\omega_a - 0.176\omega_a^2 \quad [17]$$

Giving,

$$c = \left(\frac{\partial P}{\partial \rho}\right)_s^{1/2} \quad [18]$$

This equation is expanded by Michaelides and Zisis (48) to improve the description of two-phase fluids. Equations 19 and 20 provide calculations based on the usual temperature and pressure conditions,

but also on the quality of the fluid and the thermophysical properties resulting from such a quality condition.

$$c^2 = \frac{v^2 \left(\frac{dP}{dT}\right)^2}{\frac{C_{p\text{liquid}}}{T} + \chi v_{fg} \frac{d^2P}{dT^2} - \frac{dP}{dT} \frac{dv_{\text{liquid}}}{dT}} \quad [19]$$

or

$$c^2 = \frac{v^2 \left(\frac{dP}{dT}\right)^2}{\frac{C_{p\text{liquid}}}{T} + \chi v_{fg} \frac{d}{dT} \left(\frac{h_{fg}}{Tv_{fg}}\right) - \frac{h_{fg}}{Tv_{fg}} \frac{dv_{\text{liquid}}}{dT}} \quad [20]$$

The experimental data given by Han et al. (47) are verified by the sonic speed calculations given by MegaWatSoft, Inc. (46). The sonic speed and the thermophysical properties at the four design points collected and calculated for this research are described and provided in Table 4.

Table 4. Thermophysical Properties of Carbon Dioxide at Four Design Points (44) (45) (46) (47)

System Location		Compressor		Turbine	
		Inlet	Exit	Inlet	Exit
Stagnation Pressure (MPa)	P	8.0	14.0	14.0	8.0
Stagnation Temperature (°C)	T	35	50	550	490
Isobaric Specific Heat (kJ/kg K)	Cp	29.61	3.363	1.386	1.350
Isochoric Specific Heat (kJ/kg K)	Cv	1.317	0.9542	1.082	1.017
Gas Constant (kJ/kg K)	R	28.293	2.409	0.304	0.333
Specific Heat Ratio $\gamma=Cp/Cv$	γ	22.483	3.524	1.281	1.328
Ultrasonic Velocity (m/s)	$c_{,co2}$	182.86	336.70	566.18	580.80
Density (kg/m ³)	ρ	419.20	672.2	88.14	55.11
Specific Volume (m ³ /kg)	v	0.00093	0.00149	0.01135	0.00222
Specific Enthalpy (kJ/kg)	h	-239.971	319.07	550.265	429.525
Specific Entropy (kJ/kg K)	s	-1.769	1.3559	-0.369	-0.411
Specific Exergy (kJ/kg) $ex=h-T_0*s$	ex	-103.77	214.7	578.7	461.157
Specific Internal Energy (kJ/kg)	u	-173.6	-208.5	374.0	321.0

When flow becomes supersonic, there is a corresponding subsonic condition which defines the flow after the flow passes through the shock wave. Corresponding supersonic and subsonic flow properties are related by the combined Fanno and Rayleigh lines on an h-s (enthalpy-entropy) diagram, as shown in Figure 18. The second law of thermodynamics, which defines the governance of entropy, dictates that a shock process, shown by the dotted red line in Figure 18, must proceed from point 1 to point 2. Given that the thickness of a shock wave propagating through a fluid is on the order of the mean free path, a molecular order, the adiabatic assumption is valid across the wave. Entropy of an adiabatic system increases and does not decrease; thus, a propagating shock wave will take a fluid from supercritical to subcritical as the fluid passes through the wave.

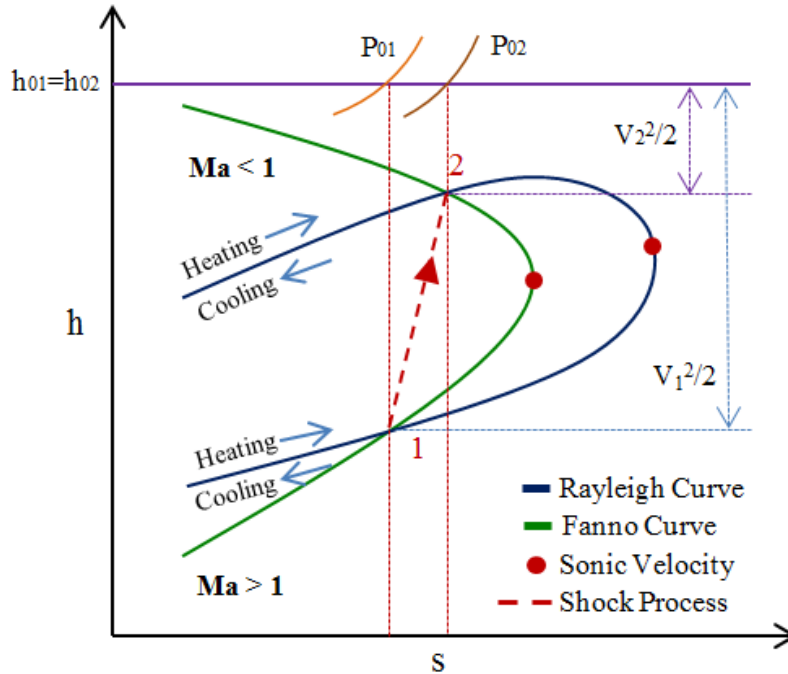


Figure 18. Fanno and Rayleigh Curve h-s Diagram

Shock waves result in supersonic flow as a result of the fluid moving with a greater velocity than the pressure wave, which propagates at sound speed with respect to the fluid. The fluid traveling in front of the wave causes discontinuity in flow as the pressure wave propagates through the fluid. This is illustrated by Som (49) for a moving control volume/point source moving at subsonic and supersonic speeds similar to that shown in Figure 19. In the case of subsonic flow, a control volume, shown in red, downstream of the wave propagation will encounter the disturbance prior to encountering the source of the disturbance. This allows smooth and controlled transition of properties within the fluid. In the case of supersonic flow, a Mach cone develops. The two dimensionally displayed, three dimensional Mach cone outlines the disturbance area, which is described by a Mach angle α and is defined by the motion of the fluid and wave propagation. Picturing this Mach cone in its three dimensional formation, the source is actually pulling in front of the wave propagation, creating the moving cone. In supersonic flow, the source is moving faster

than the wave propagation; thus, a control volume downstream, shown in red, will encounter the disturbance prior to encountering the source of the pressure wave. This causes discontinuity in the flow, resulting in a shock due to the inability of the fluid to smoothly pass through this transition.

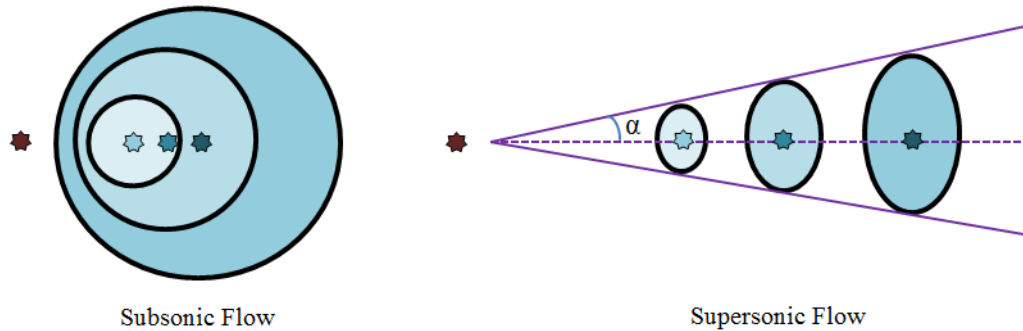


Figure 19. Illustration of Subsonic and Supersonic Flow (49)

Mach number (Ma) describes flow as subsonic, sonic, or supersonic, where Ma is, respectfully, less than, equal to, or greater than 1. It is a value determined by the relationship between the fluid velocity and the sonic, or acoustic, velocity given by a particular fluid under specific conditions, and described by Equation 21. Mach number limitations are typically 0.7 to 0.8 to avoid sonic flow and excess loss, while maintaining desirable efficiencies.

$$Ma \equiv \frac{V_f}{c} \quad [21]$$

3.4.2 Centrifugal Compressor Flow Conditions

After determining flow velocity constraints are based upon compressor inlet conditions, turbomachinery size design parameters begin with the compressor wheel. In order to avoid sonic velocity,

flow velocity at the compressor inlet, where the sonic velocity is a minimum, 182.86 m/s, is limited by a Mach number of 0.7 to provide a greater margin of desirable flow conditions.

$$V_f \leq Ma * c = 128.0 \text{ m/s at the compressor inlet} \quad [22]$$

The fluid velocity must then be converted into a mass flow rate, based upon the thermophysical properties of the fluid and the geometric flow area at the compressor inlet design point. The relationship between the mass flow rate and the geometric parameters can be numerically optimized. The mass flow rate is related to the flow velocity in the typical manner.

$$V_f = \frac{\dot{m}}{\rho A} \quad [23]$$

With this formula, the given maximum velocity, and the density of the fluid at the compressor inlet, the dimensional ratio of mass flow to cross sectional flow area must be less than or equal to 1.97E5. Similarly, the dimensional ratio of mass flow to cross sectional flow area of the fluid at the compressor exit must be less than or equal to 1.58E5.

Assuming the mass flow rate is constant at the inlet and exit for a steady state process, and the cross sectional flow area before and after the impeller is the same, a relationship can be estimated between the inlet flow velocity, 128.0 m/s, and the exit flow velocity by Equation 24, providing a compressor exit flow velocity of 79.95 m/s. This exit flow velocity is used to determine the Mach number for the flow at the compressor exit, using Equation 21, yielding 0.237, a value void of concern.

$$V_{f1}\rho_1 = V_{f2}\rho_2 \quad [24]$$

The inlet Mach number and the stagnation temperature at the compressor inlet design condition are used to calculate the inlet static temperature, T_{s1} , giving 13.43 K (21).

$$\frac{T_{01}}{T_{s1}} = \frac{1 + (\gamma - 1)}{2Ma_1^2} \quad [25]$$

3.4.3 Centrifugal Compressor Impeller Dimensions Design

Rotational speed is the second design consideration for decisions regarding turbomachinery hub and shroud diameters. Rotational speed is calculated by the desired design point conditions, including the inlet temperature and the desired pressure ratio, and the corresponding thermophysical properties. For axial flow entry and radial exit centrifugal compressors, the Euler turbine equation is modified to apply to centrifugal compressors by Equation 26 (50).

$$U_{2,c} = \sqrt{\frac{\gamma RT_{01}}{\mu_s(\gamma - 1)} \left(\frac{P_{02}}{P_{01}}\right)^{\frac{\gamma-1}{\gamma}}} \quad [26]$$

Yoon et al. determined the optimal pressure ratio for SCO₂ Brayton cycle turbomachinery is 2.6 (51). This is considered optimistic; therefore, the design points published by Sandia National Laboratory (22) are again used as a guide. The pressure ratio, given an inlet side pressure of 8 MPa and an exit side pressure of 14 MPa, is a calculated 1.75. The expected temperature at the compressor inlet is 550 °C. The difficulty is with providing an accurate specific heat ratio to define the flow over the entire compressor. As shown in Table 4, the specific heat ratio is radically different at the compressor inlet, compared to the compressor exit. This fact makes using Equation 26 unreliable. Slip factor, present in Equation 26, is typically estimated at 0.9. By definition, slip factor is given by Equation 27. With the exit fluid velocity calculated in the previous section, this definition yields an estimated exit blade velocity of 88.83 m/s.

$$\mu_{s,c} \equiv \frac{V_{f2}}{U_2} \quad [27]$$

Equation 28 describes exit blade velocity as a function of rotational speed and shroud diameter, also noted as compressor exit diameter. Rotational speeds for similarly sized systems in the literature range from 30,000 rpm to 75,000 rpm. One revolution per minute is equal to $\pi/30$ radians per second. Applying rotational speeds of 30,000 rpm and 75,000 rpm to Equation 28 yields exit radii of 0.0283 m (1.114 in) and 0.0113 m (0.4449 in), respectively.

$$U_2 = \omega r_2 \quad [28]$$

Thus, the compressor wheel is optimized for this 100 kW system at a calculated diameter between 0.0226 m (0.8898 in) and 0.0566 m (2.228 in), depending on the rotational speed. Fabrication capabilities are then considered. Wheels of extremely small size, particularly one with the complexity of a centrifugal compressor, are impossible to fabricate under the constraints of the Computer Numerical Control (CNC) machine located in the UNLV Machine Shop. Wheel sizes in the smaller end of the range are then dismissed. Conversely, larger wheel diameters couple with higher rotational speeds, which can lead to control concerns. A mean diameter of approximately 0.038 m (1.5 in) is the chosen design point. By Equation 28, this diameter corresponds to a rotational speed of 44,527 rpm, which is higher than desired. This mid-sized design point remains small and does present significant fabrication obstacles, though is possible. This diameter size is also similar to that present in the literature for similar systems, allowing for the increased ability to provide comparison analysis between the UNLV experimental SCO₂ system and other numerical and experimental models.

The impeller diameter, with thermophysical properties and flow velocity, determines the Reynolds number of the fluid by Equation 29. Boyce (50) describes the importance of continuity in the magnitude

of the Reynolds number throughout the flow path. This provides a relationship between the inlet and outlet impeller diameter. The expected Reynolds number for the compressor exit design point is a calculated $3.84E7$. Maintaining Reynolds number across the inlet and exit of the compressor provides a compressor inlet impeller diameter of 0.0214 m (0.8417 in) by Equation 30.

$$\text{Re}_c = \frac{\rho V D}{\mu} \quad [29]$$

$$\frac{\rho_1 V_1 D_1}{\mu_1} = \frac{\rho_2 V_2 D_2}{\mu_2} \quad [30]$$

Flow blockage is the blockage of the flow area contributed by the hub and blades. Given the small size of the compressor impeller, the blockage due to blade thickness can be considered negligible compared to the hub blockage. For this reason, hub blockage is estimated to define flow blockage. An accepted estimation for flow blockage, provided by Boyce (50), is 4% to 5% of the cross sectional area defined by the compressor eye diameter. Five percent of the area defined by the calculated eye diameter, or compressor inlet diameter, of 0.0214 m (0.8417 in) is 0.004785 m (0.1884 in). This is the estimated hub diameter. The eye and hub diameters provide a blade height calculation by Equation 31 (50). The blade height at the inlet of the compressor is then 0.008307 m (0.3270 in).

$$h_{b,\text{inlet},c} = \frac{D_{\text{eye}} - D_{\text{hub}}}{2} \quad [31]$$

The number of blades, $N_{b,c}$, can be estimated by using the Balje slip factor equation. This equation, shown as Equation 32, is valid for axial inlet and radial exit centrifugal compressors. The mean inlet diameter is 0.01336 m (0.5261 in), given by Equation 33. The Balje slip factor equation, again using an estimated slip factor of 0.9, estimates nearly 7 blades (6.889 blades) as optimal.

$$\mu_s = \frac{1}{1 + \frac{6.2}{N_{b,c} \left(\frac{D_2}{D_{1 \text{ mean}}} \right)^{2/3}}} \quad [32]$$

$$D_{1 \text{ mean}} = D_{\text{hub}} + h_{b, \text{inlet}, c} \quad [33]$$

Backward leaning blades are known to provide greater stability within a desirable pressure ratio and efficiency (50). Backward leaning blades are defined as blades with a beta angle less than 90° at the compressor exit, or hub, with exactly 90° and less than 90° referred as radial and forward leaning (21) (50). These angles are relative to the normal. Forward leaning blades encourage higher than desired exit fluid velocities and high diffuser losses. In the case of forward leaning blades, fluid velocity is more likely to reach sonic flow. Furthermore, boundary layer induced flow separation, which is a function of the velocity profile, is more likely. An estimation defining the exit blade angle can be calculated for a known design number of blades by Equation 34 or by using the Eck slip coefficient relation, Equation [35] (21). For blade angles between 20° and 45° relative to radial, Eck indicates the coefficient a is 0.9 and b is 3.7. Calculating with a blade number of 6 and a slip coefficient of 0.9, Equation 34 yields a positive blade angle of 17.96°, and Equation 35 yields a negative blade angle -10.82°. Though both may present an efficiency design point, the negative blade angle indicates a forward swept blade, which, as discussed, is not stable. Therefore, the 17.96° blade angle is the accepted design point. This approximately 18° angle is relative to normal against the direction of rotation, thus approximately 72° from the tangent line which increases in the direction of rotation.

$$N_{b,c} = 8.5 \frac{\sin \beta_{n2}}{\left(1 - \frac{r_1}{r_2} \right)} \quad [34]$$

$$\mu_s = \left(1 + \frac{a + b \frac{\beta^\circ n^2}{90}}{N_{b,c} \left[1 - \left(\frac{r_1}{r_2} \right)^2 \right]} \right)^{-1} \quad [35]$$

3.4.4 Centrifugal Compressor Performance Design Considerations

Specific speed is the nondimensional parameter used to estimate compressor efficiency. Boyce (50) provides a graph, displayed as Figure 20, to estimate adiabatic efficiency from specific speed, though he does note that these are approximations based on a wide variety of machines and are not necessarily specific to any single machine. This graph can similarly be used to define a specific speed range to achieve a desired efficiency range. In an attempt to achieve the highest possible efficiency, a specific speed between 80 and 90 is desired for this centrifugal compressor.

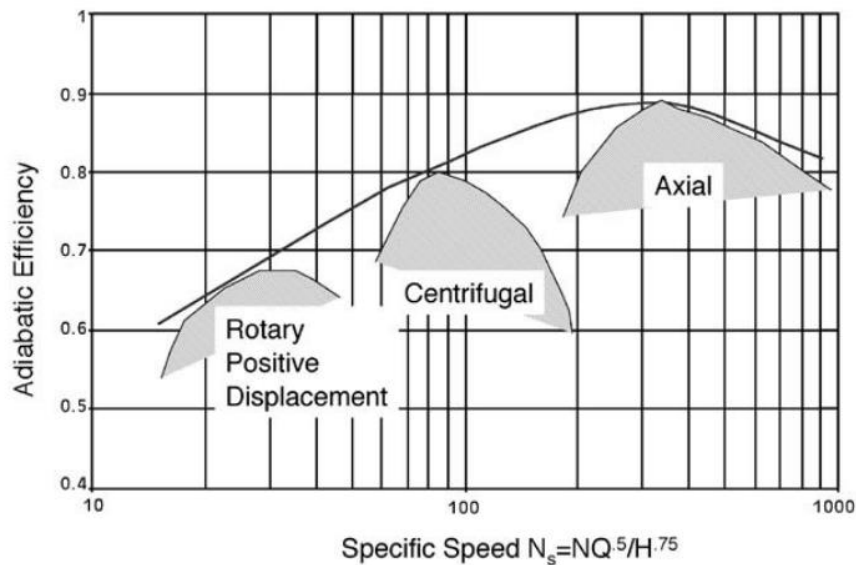


Figure 20. Boyce's (50) Adiabatic Efficiency Estimation Based on Specific Speed

The desired specific speed is used to provide a desired mass flow rate for the system. Specific speed is calculated by Equation 36, requiring specific units as shown. The rotational speed, N , calculated for the given design point diameter is 44,527 rpm. Adiabatic head is calculated by the second part of Equation 37 using the properties listed in Table 4. A specific speed of 85, corresponding to an estimated adiabatic efficiency for a centrifugal compressor near 80%, yields a volumetric flow rate of 115.52 cfm. The subsequent conversion of this value to a mass flow rate yields an inlet mass flow rate of 22.85 kg/s, given by the EES density at the compressor inlet. This value is compared to the mass flow rate calculated by Equation 38, using design point conditions previously discussed. The mass flow rate given by the latter is 18.34 kg/s. If this value is used to again calculate specific speed by Equation 36, the calculated specific speed is 76.14, corresponding to an adiabatic efficiency of approximately 77%.

$$N_s = \frac{N[\text{rpm}]\sqrt{Q_{v1}[\text{cfm}]}}{(H_{ad,t}[\text{ft lbf/lbm}])^{3/4}} \quad [36]$$

$$H_{ad,t} = h_{02} - h_{01} = Z_{ave} \frac{R}{M} \frac{\gamma}{\gamma-1} T_{01,c} \left[\left(\frac{P_{02,c}}{P_{01,c}} \right)^{\frac{\gamma}{\gamma-1}} - 1 \right] \text{kJ/kg} \quad [37]$$

$$\dot{m} = \rho_1 V_{f1,c} A_{1,c} = \rho_1 V_{f1,c} [\pi(r_{eye}^2 - r_{hub}^2)] \quad [38]$$

3.4.5 Radial Inflow Turbine Impeller Dimensions Design

The original brainstorming process for the design of the turbine impeller began with an anticipated mass flow rate of 0.18 kg/s and a rotational shaft speed of 30,000 rpm. These parameters were found as low value averages for similarly sized systems in various literature sources. Inlet flow velocity can be calculated by Equation 39 with turbine inlet properties listed in Table 4 and a flow area defined by inlet inner tube diameter 0.0106 m (0.417 in). The flow velocity with mass flow rate 0.18 kg/s is 23.14 m/s.

$$V_{2,t} = \frac{\dot{m}}{\rho_2 A_{\text{inlet},t}} \quad [39]$$

Boyce (52) suggests that the ratio of flow velocity to blade tip speed is generally 0.8. Using this suggestion with a 30,000 rpm rotational speed, Equation 40 yields a turbine inlet diameter of 0.01841 m (0.7248 in).

$$U_{2,t} = \frac{\pi D_{2,t} N}{60} \quad [40]$$

This diameter is much too small to fabricate using the UNLV CNC machine, therefore other parameters are considered. The parameters which result from the compressor impeller design process call for a rotational speed of 44,527 rpm and a mass flow rate of 18.34 kg/s. Based on Equation 40 and all else constant, a higher rotational speed would lead to a smaller diameter; therefore, mass flow rate changes are considered. According to Equation 39, the flow velocity given by a mass flow rate of 18.34 kg/s is 2357.97 m/s. With a turbine inlet sound speed of 566.18 m/s, this velocity is clearly higher than sonic. The maximum flow velocity given by Equation 21 with Mach number 0.8 is 452.9 m/s. By Equation 39, this maximum flow velocity yields a maximum mass flow rate of 3.52 kg/s; and by the 0.8 velocity ratio suggested by Boyce (52), this maximum flow velocity yields an impeller velocity of 362.4 m/s. The maximum impeller velocity at 30,000 rpm and 44,527 rpm yields a turbine inlet diameter of 0.2307 m (9.08 in) and 0.1554 m (6.12 in), respectively. Both of these diameters are much larger than that of the compressor, thus performance methods are reviewed.

3.4.6 Radial Inflow Turbine Performance Design Considerations

Ns-Ds diagrams provide a relationship between specific speed, Ns, and specific diameter, Ds, yielding an adiabatic efficiency profile as well. The dimensionless specific speed is calculated similar to that for the compressor, in Equation 36, with Q describing the exhaust flow rate in cubic feet per second and adiabatic head calculated by Equation 41. The specific heat for carbon dioxide does change over the flow path in the turbine, thus this is reflected and not considered constant in the equation. The properties listed in Table 4 are used in calculations leading to a 110.63 kJ/kg (37011.60 ft lbf/lbm) adiabatic head. The mass flow rate is limited through the turbine by the previous section; thus, the previously calculated 3.52 kg/s mass flow rate is used to calculate the flow rate Q with the density at the turbine exit (53). The flow rate at the turbine exit is calculated to be 0.0639 m³/s (2.26 ft³/s). The specific speed is then 25.1.

$$H_{ad,t} = h_{01} - h_{03} = C_{p1}T_{01} - C_{p3}T_{03} \quad [41]$$

The Ns-Ds diagram provided by Barber-Nichols, Inc. (54) is displayed in Figure 21. This chart provides general design parameter approximations for turbine impellers. The calculated specific speed of 25.1 yields a maximum efficiency above 70% with a specific diameter approximately between 1.5 and 3.5.

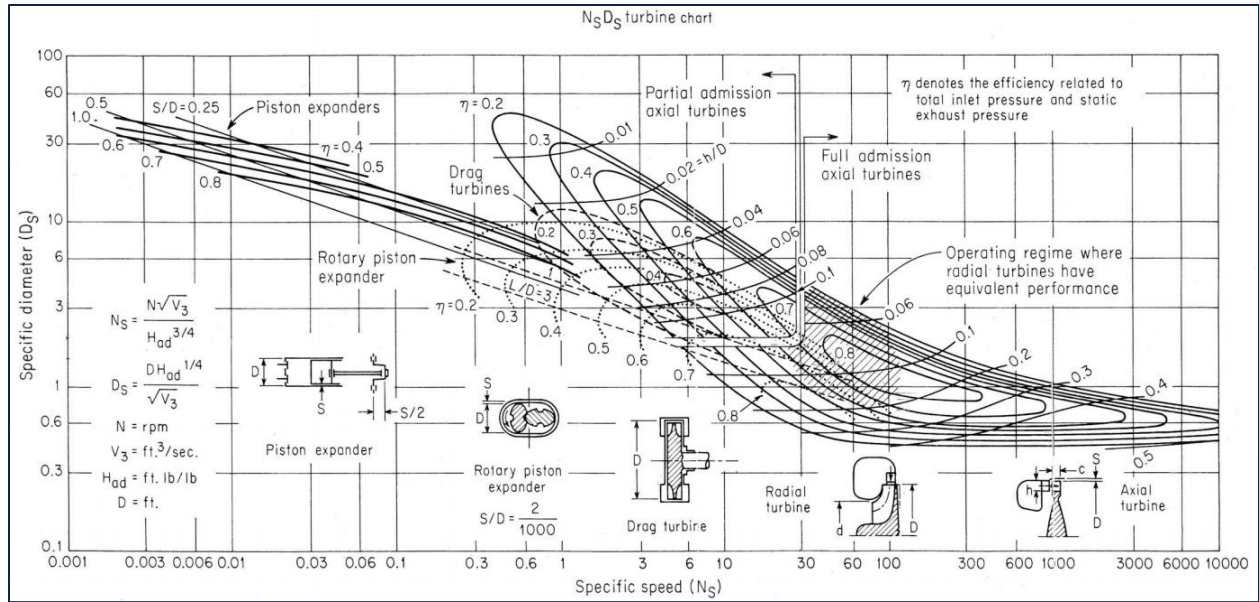


Figure 21. Barber-Nichols, Inc. Ns-Ds Turbine Chart (54)

The specific diameter corresponding to the calculated specific speed is used in Equation 42 to solve for the turbine inlet diameter. Specific diameters of 3.5 and 1.5 yield impeller diameters of 0.1156 m (4.55 in) and 0.0496 m (1.95 in), respectively.

$$D_s = \frac{D[\text{ft}](H_{ad}[\text{ft lbf/lbm}])^{1/4}}{\sqrt{Q_{v1}[\text{cfs}]}} \quad [42]$$

In order to reach efficiencies in the 80% range, Figure 21 suggests a specific speed between 40 and 60, with a specific diameter between 1.0 and 1.5. The diameter corresponding to a specific diameter of 1.5 has been calculated. At a 1.0 specific diameter, the impeller diameter is 0.0330 m (1.30 in). For a turbine and compressor on the same shaft, similar impeller diameters create ease of manufacturing. Due to expected differences in theoretical and experimental operation, the initial turbine impeller is designed for the highest possible efficiency with the lowest rotational speed. Further, there are turbine impeller designs

in the literature around the smaller, yet higher efficiency, size. The chosen inlet diameter design point for the turbine impeller is, therefore, 0.0330 m (1.30 in), a design point optimizing both ease of manufacturing and the ability to complete experimental comparison analysis with current research in the literature.

Boyce (52) suggests a typical inlet to tip diameter ratio of 2.2 for radial inflow turbines. This provides a basis for the exit impeller diameter. Given a 0.0330 m (1.30 in) inlet diameter, the relation suggests a 0.015 m (0.59 in) exit impeller diameter. Again, Boyce (52) suggests that the ratio of flow velocity to blade tip speed is generally 0.8. This can be used to estimate blade number by Equation 43, and yields approximately 14 blades (14.4), defined by the suggested velocity and diameter ratios.

$$\frac{V_{02,t}}{U_{2,t}} = 1 - \frac{\pi}{2N_{b,t}} \frac{D_2}{D_2 - D_3} \quad [43]$$

The small size of the wheel leaves little room for 14 blades. In anticipation of fabrication, other relationships are considered. Suggestions for the turbine impeller tip diameter to inlet diameter ratio vary from that of Boyce in the literature. McLallin and Haas (55) describe a design analysis for a 0.1504 m overall impeller diameter, suggesting a 1.6 turbine impeller inlet to tip diameter ratio, a 2.06 tip to hub ratio, and a 12 blade design. Vilim (20) and Wright et al. (22) describe a system more similar in size to the UNLV parameters. Vilim (20) describes a design process for a turbine impeller with an overall diameter of 0.0676 m, having a 2.12 inlet to tip diameter ratio, a 2.49 tip to hub ratio, and 11 blades. The turbine impeller shown in the report by Wright et al. (56) displays the final product, designed by Vilim (20), with 12 blades. The Vilim (20) report further notes a turbine impeller exit blade angle of 150°. Given the overall dimension similarity of these impellers to the calculated design parameters, these reports, which include additional detailed information, are used to provide insight to the final impeller design and fabrication.

3.5 Turbomachinery Fabrication

The increased complexity of this component in both geometry and coordination prompted a modular plate vane casing design. This modular design provides an enhanced capability for prototype and future fabrication, modification, and optimization. To clarify, the inlets, outlets, volutes, and vanes are specifically spaced to be broken into 11 sections or plates. The separated vane casing plates are displayed in Figure 22. Though the detailed machining on each plate is not shown in this document, each plate is unique in the machining it hosts and in its placement in the assembly. Plate dowels are used to secure each plate to the next and to maintain alignment when assembled. These dowels are visible as small cylindrical protrusions in Figure 22.



Figure 22. Turbomachinery Vane Plate Assembly

The bolt pattern is one of the most significant design aspects of the turbomachinery from a safety perspective. In the turbine side of the machinery, the pressure is expected to approach 14 MPa, but has numerically shown up to 22 MPa maximums, though unlikely and not desired. The bolts provide structure to the casing, and the pattern was designed with consideration given to both the expected size of the

impellers and the volute path plan dimensions. The bolt design is formulated with a 200 mm (8 in) initial plate diameter and a maximum pressure requirement of 22 MPa. The size of the final volute path is described by the blue arrow, and the inlet notch is shown at the end of the green line, both displayed in Figure 23. The inlet notch is squared off to allow for fitting thread addition and proper tightening tool allowance.

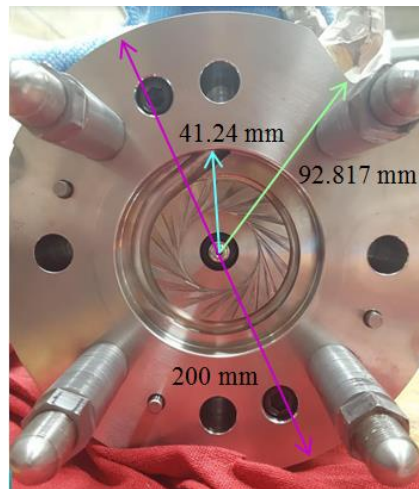


Figure 23. Bolt Pattern Design in a Modular Casing Plate

The initial guess for the bolt pattern was six bolts, evenly spaced. Recalculations were made for bolt numbers from six to eleven bolts. The deciding factor is based upon the combination of three factors: the thickness requirement for each bolt, the ability to allow the proper amount of space between the bolt and both the plate edge and the plate hollowed paths, and the overall bolt thickness to plate radius ratio. A general rule is for the edge of the bolt hole to be placed no less than the length of the bolt thickness away from the edge of the plate. For example, if a $\frac{3}{4}$ " bolt is chosen, the bolt hole must allow a minimum of $\frac{3}{4}$ " clearance between it and the edge of the plate or any hollowed path. The overall distance requirement in

this 3/4" bolt example is 1.5 in (57.15 mm) from the plate edge. Subtracting the hollowed space and volute edge, shown in blue in Figure 23, from the plate radius yields 58.76 mm. This is the distance between the hollowed space and the plate edge, and is only slightly larger than the 57.15 mm required by the use of a 3/4" bolt. The 3/4" bolt is the maximum bolt thickness allowed by the 8 inch plate design. To allow for additional clearance, a 5/8" bolt thickness is desired.

Assuming that the hollowed space is the pressure cavity, the force requirement per bolt is calculated by Equation 44. The calculation uses the maximum pressure in the cavity and the 41.24 mm cavity described. The equation is solved from six to eleven bolts.

$$F_{bt} = \frac{P_{max} \pi r_{cav}^2}{N_{bt}} \quad [44]$$

The force requirement per bolt is then used to determine the bolt thickness capable of achieving this goal. This calculation is completed by Equations 45 and 46, where sigma is given by the yield strength, S_y , 240 MPa (3.48E7 psi), in this case. Bolt thickness greater than the minimum requirement, along with a factor of safety yield eight, stainless steel 316, 5/8" bolts oriented in a revolved, evenly spaced pattern are chosen for the final bolt design.

$$F_{bt} = \sigma_s A_b \quad [45]$$

$$r_{bt} = \sqrt{\frac{F_{bt}}{\sigma_s \pi}} \quad [46]$$

To assure success, deformation and tensile force required to yield the entire threaded contact surface are cross checked against design conditions. The main deformation equation considered is shown as Equation 47 Young's Modulus, E_b , for stainless steel 316 is approximately 193 GPa (2.80E7 psi).

$$\delta_b = \frac{F_{bt}L}{A_b E_b} \quad [47]$$

With significant work contributed by Trevor Rose, UNLV ME undergraduate, and Terry Kell, UNLV Machine Shop Director, the SolidWorks drawings were created. The design guidelines calculated by the previous sections were set as the basis for the SolidWorks parts and assembly drawings. As the research team developed the drawings in SolidWorks, dimensions were altered. Initial alterations were made as a result of the design process within the software. For example, feasible extruded cut patterns affect expected hub dimensions due to curvature definitions of the impeller base. Furthermore, the drawings were run through MasterCam Simulator to illustrate fabrication issues to avoid encountering them in machining. During these simulations, some dimensions and angles were modified to avoid foreseen fabrication issues. The final prototypes are a combination of the calculated design parameters and the drawing and fabrication design modifications. The final turbine impeller drawing is displayed in Figure 24; the final compressor impeller drawing is displayed in Figure 25; and, two final assembly views are displayed in Figure 26, where the impellers are shown encased by the modular plates.

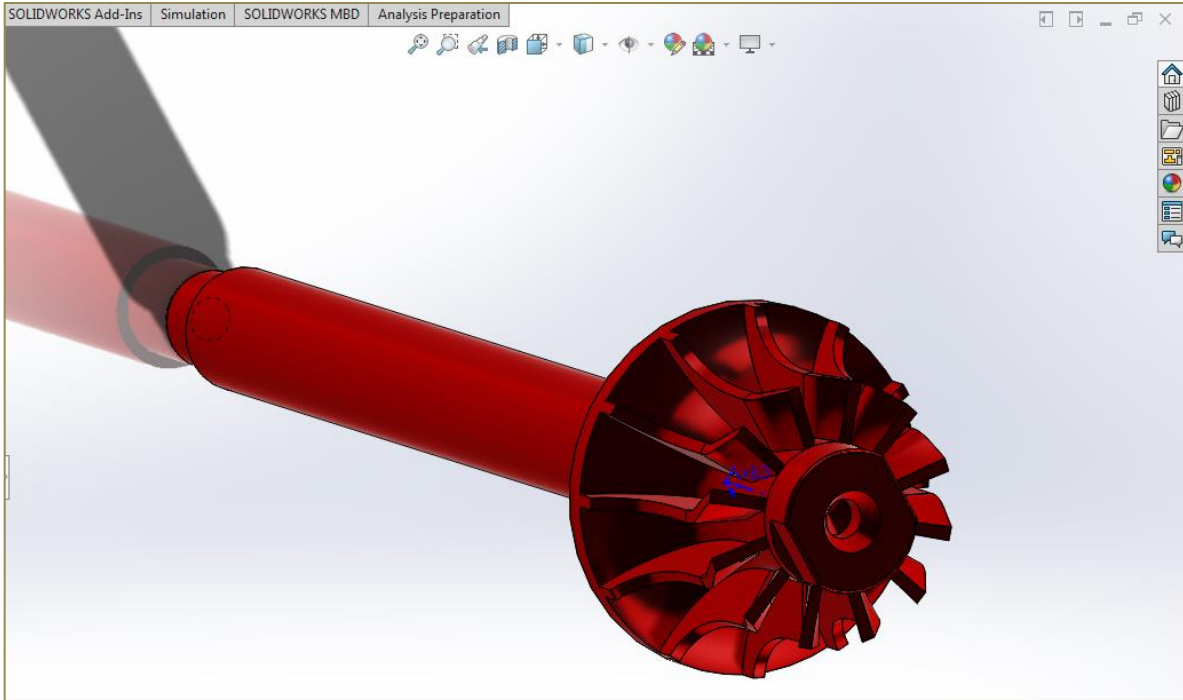


Figure 24. Final SolidWorks Turbine Impeller Drawing

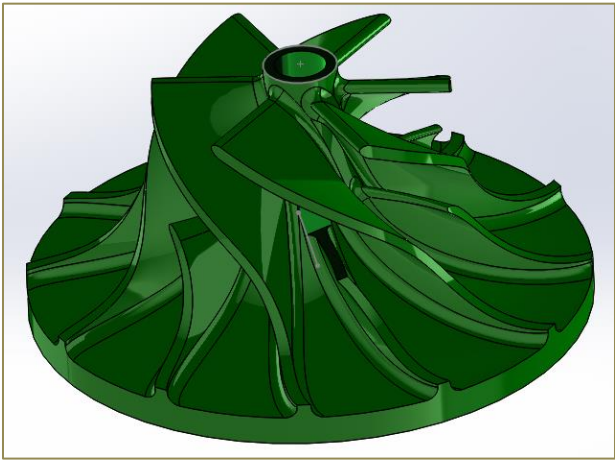


Figure 25. Final SolidWorks Compressor Drawing

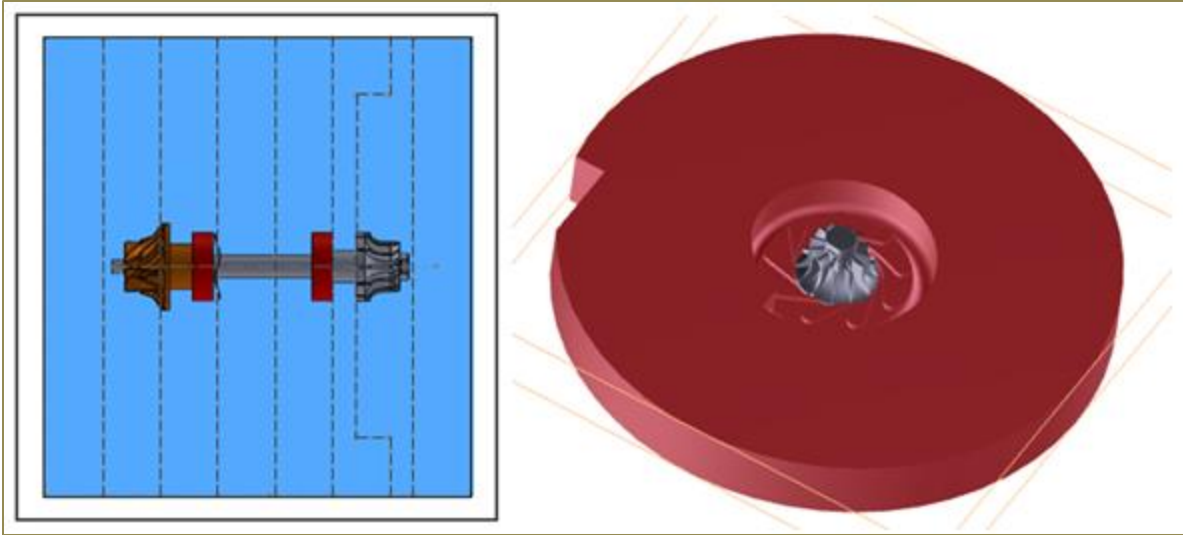


Figure 26. Turbomachinery SolidWorks Assembly

Final prototypes of the turbine and compressor impellers are displayed in Figure 27.

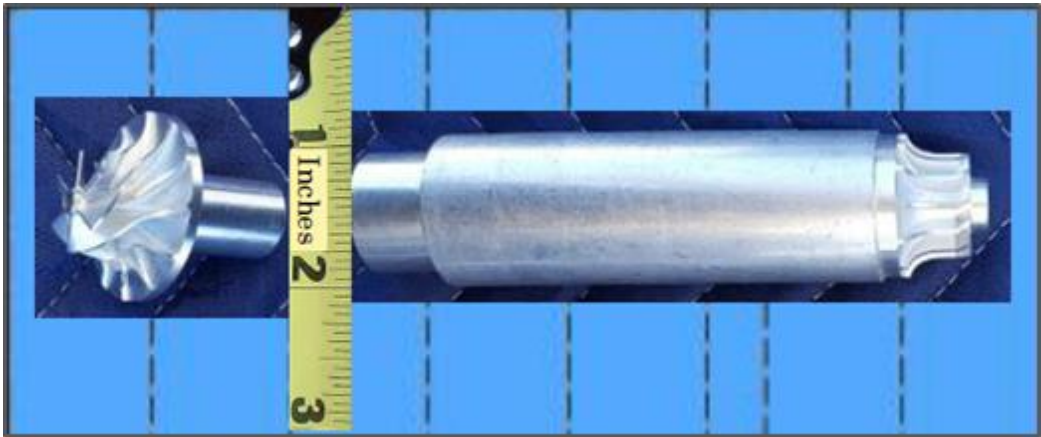


Figure 27. Turbine and Compressor Wheel Prototypes

CHAPTER 4. ENGINEERING EQUATION SOLVER (EES) COMPUTER MODELING

In an effort to estimate some design parameters and basic expectations, a general model of the system using EES was established. Due to the use of primary characterization approximations in most of the system components, certain simplifications in the general code are determined acceptable. In particular, the specific heat of CO₂ was averaged across each component. The general code begins with defining starting points for the system. These include the maximum heat in, provided by the sun to the receiver. The system has a maximum concentrated heat value of approximately 113 kW. After photographic flux mapping analysis, it is estimated that the actual heat in is about 100 kW. The temperature out of the receiver can be controlled via the system being on and off of sun. The maximum temperature through the system is limited by material properties. For this reason, the general code allows the user to define the outlet temperature of the receiver. In this iteration, the receiver outlet temperature is set at 500 °C. In order to maintain carbon dioxide in the supercritical state, the lowest pressure in the system must be above critical pressure, 7389 kPa. This pressure value is defined by the user as a determinant value for the rest of the system. In the general code, the compressor inlet pressure is set to 7700 kPa, a small factor of safety above critical. Other defined variables include ambient temperature, fan speed across the air cooled heat exchanger, tube dimensions, and the experimentally controlled mass flow rate.

4.1 Receiver/Turbine Interface

After defining system parameters as described, the general code begins with the receiver/turbine interface. This portion of the code includes receiver analysis to estimate the receiver outlet pressure. An assumption is made that the temperature in the receiver escalates quickly; therefore, the properties of carbon dioxide are determined at the user defined maximum receiver temperature. This assumption is determined to be valid based on initial receiver testing, during which data show the receiver temperature

approaching a maximum within five minutes. The inlet pressure is integrated with and set by the outlet pressure of the XHEX.

4.2 Turbine

The inlet conditions to the turbine are determined by the outlet conditions from the receiver. The outlet pressure of the system is determined by the numerically calculated pressure ratio. The user defined pressure ratio and turbo-compressor efficiency are estimated by the literature. Yoon et al determined the optimal pressure ratio for SCO₂ Brayton cycle turbomachinery is 2.6 (51). This numerical model can be run with this optimized pressure ratio for improved results; however, these results would likely be optimistic. Thus, a more modest pressure ratio of 1.6 is used. This is a slightly improved pressure ratio than that of the published test results of a similar sized turbine wheel published by Sandia National Laboratory of 1.2 (57). The outlet temperature for the turbine in the general code is estimated by using the assumed temperature and following formula:

$$T_{2,t} = T_{1,t} \left(\frac{P_{2,t}}{P_{1,t}} \right)^{\gamma-1/\gamma} \quad [48]$$

An isentropic assumption is made in the general code calculations, although the process is not reversible. Some of the loss is accounted for in the actual work calculations by using a reasonable efficiency multiplier of 0.75. A universally accepted efficiency range for radial turbomachinery is between 0.70 and 0.85. Here, an assumptive isentropic specific heat ratio of 1.289 is used for the working fluid. After collecting experimental temperature and pressure data, appropriate corrections will be made.

The turbine work is estimated by using the enthalpy values calculated in EES with the inlet and outlet temperatures and pressures. The mass flow rate and assumptive turbine efficiency are also factors in ideal and actual turbine work estimations.

4.3 Recuperator – Xi’an Jiaotong University Printed Circuit Heat Exchanger (XHEX)

The inlet conditions to the XHEX are initially set to the corresponding temperature and pressure outlet conditions of the previous component. The pressure drop and temperature change across the heat exchanger are taken from data collected and provided by the collaborating university. Prior to shipment, experimental data were collected on the straight channel component and numerical data were collected on both the straight and zig-zag channel models. The experimental data were collected at much lower temperatures and lower hot side pressures than the UNLV system intends; however, this test was predominantly for leak testing. Therefore, the numerical simulation of the XHEX performance under operating conditions is used. An assumption is made that the average temperature drop across both the hot side and cold side remains the same for inlet temperatures close to that in the numerical model. The modeled temperature drop and the hot and cold inlet temperatures in the model loop are used to solve for the XHEX outlet temperatures. Exchanging heat between the two yields an average temperature drop of 184 °C. The XHEX outlet pressures are calculated in a similar manner, using the turbine and compressor outlet pressures and the pressure drop provided by the XHEX numerical model by Xi’an Jiaotong University for this heat exchanger. The pressure drop used is 0.8 for the hot side flow and 0.89 for the cold side flow across the straight channel XHEX.

4.4 Air Cooled Heat Rejection Heat Exchanger (ACHEX)

The effectiveness NTU method is used to estimate the outlet temperature of the working fluid. The working fluid is cooled by ambient air in a crossflow, open fan configuration. The fan speed is estimated by using the specifications of an industrial fan of similar size. This speed may be modified with air flow data collection. In this iteration, the air velocity is calculated from the estimation. An average summer ambient air temperature of 40 °C is used, and the inlet temperature of the working fluid is taken from the XHEX cold side outlet. Fluid properties are calculated in EES using the inlet temperature and pressure to the ACHEX. The Prandtl number is also determined by EES, giving rise to the Reynolds number

calculation. These are used to estimate the heat transfer coefficient using a formula published by Oh and Son of a macrochannel heat exchanger model similar to the ACHEX design (38).

The pressure drop across the ACHEX is estimated by using standard calculations for laminar flow in a smooth pipe. A friction factor is used based upon the approximate Reynolds number. A side code is first written for calculating the flow properties in the ACHEX. This code added to the general code, and is used to estimate this determinant Reynolds number.

4.5 Compressor

The compressor code begins with an input temperature from the ACHEX. The computer cannot inherently determine temperature discontinuities. The minimum ACHEX outlet temperature is physically limited to ambient. The code will continue to reduce the temperature based upon the math and the length of the tube. Therefore, a caveat is added into the code to set the compressor inlet temperature to ambient, if the outlet temperature of the ACHEX yields a temperature below ambient. If the ACHEX outlet temperature is at or above ambient, this value is used as the compressor inlet temperature. The compressor inlet pressure is the calculated ACHEX outlet pressure, which accounts for the pressure drop across the ACHEX component. The outlet pressure of the compressor is based upon the assumed pressure ratio discussed in the turbine section of this report. The outlet temperature is calculated by again using an isentropic assumption with the inlet temperature, inlet and outlet pressures, and the assumed specific heat ratio in this general system code. The compressor inlet entropy and enthalpy are determined using corresponding temperature and pressure calculations. Compressor work is calculated by the enthalpy difference determined in EES by the inlet and outlet temperatures and pressures.

CHAPTER 5. SENSING DEVICES

The primary measurements in the system are mass flow rate, temperature, and pressure. This section describes each of the sensors and their connectivity to electronic monitoring. Although pressure is respected, temperature tolerance is the constraining factor in sensor selection. Sensors used in the system were chosen based on their position in the system and the expected temperature at the installation point. All sensors were chosen to withstand a pressure of $1.379E7$ Pa [2000 psi] or more.

5.1 Omega High Temperature J Type Thermocouple Model XCIB-J-1-3-10

The Omega XCIB-J-1-3-10 high temperature J type thermocouples operate continuously up to 980 °C and up to 1038 °C in short term applications. The sensing metals are iron/constantan. Constantan is copper/nickel, which appears as 55% copper and 45% nickel in this sensor. The sensor is constructed with Nextel fiber insulation covered by an Inconel overbraid. The accuracy of an Omega J type thermocouple is the greater of 2.2 °C or 0.75%, or, for lists special limits of error, the greater of 1.1 °C or 0.4%. Although Omega does not specify, the linearity of thermocouples increase above 100 °C (58). This suggests that at the expected solar receiver operating temperature, well above 100 °C, the accuracy may be within the special limits of error.

These sensors are used for estimating the internal temperature of the solar receiver by measuring the perimeter tube temperature. RTDs inserted into the flow provide a more accurate temperature measurement of fluid temperature; it is also extremely valuable to measure the temperature of component material, as certain heat conditions derate material properties. In an initial solar receiver test case, a small segment of the solar receiver was measured to reach 950 °C without mass flow. Although the system is designed to operate at temperatures much lower than 950 °C, measuring temperature with Omega J type thermocouples provide a versatile, high temperature solution. Eight thermocouples are fixed along the

rings of the receiver, spaced in an even approximation in the conical direction. The thermocouples are sequenced starting from the smallest ring and moving toward the larger rings.

The sensors are shipped with type NXHX ceramic male connectors. To connect to the CSI CR1000 data logger, the male connectors are unscrewed, removed, and saved for other applications. The revealed leads both appear silver in color; however, one is swiped with red color. This two lead configuration supports an analog signal, thus, all of these thermocouples are connected in matched sequence to a CSI Model AM16/32 multiplexer to save space on the CSI CR1000. The red lead of JType (1), the first sequential thermocouple, connects to the 1H (1 high) signal port and the silver color (aka white) wire connects to the 1L (low) signal port. The remaining seven thermocouples are connected in the same sequential manner. The multiplexer is then connected to the data logger. Campbell Scientific catalogs J type thermocouples in their temperature sensor database. There is little variation in accuracy by brand for thermocouples, thus the Campbell Scientific J type code is used with these sensors. No additional adjustment is deemed necessary.

The expected accuracy is confirmed in an ambient temperature operational test of the sensor in the data logger test box. Three thermocouples are connected in the manner described. The resulting data read all three thermocouples at the same 24.6 °C and the reference temperature at 25.9 °C. Given that the reference temperature is located within the electronics of the logger, this temperature is expected to be slightly higher; however, even neglecting that likely difference, the accuracy is within 2.2 °C.

5.2 Omega High Temperature R Type Thermocouple Model XIN-P13R-U-187-26-M-TJ-BX-4

The Omega XIN-P13R-U-187-26-M-TJ-BX-4 high temperature R type thermocouples use Platinum-13% Rhodium versus Platinum sensing metals. These thermocouples continuously operate up to 870 °C and are rated up to 1450 °C. The probe style sheathing material is Inconel 600, which is able to withstand

1150 °C, with a 1400 °C approximate melting point. Type R thermocouples are known for high accuracy, with standard limits of error being 1.5 °C or 0.25%, whichever is higher.

These thermocouples are installed at the interface defining the solar receiver exit and the turbine inlet, and also at the exit of the turbine. The connections are completed in similar fashion to the J type thermocouples, previously described. There is little variation in accuracy by brand, thus the Campbell Scientific R type code is used. No additional adjustment is deemed necessary.

5.3 Omega High Temperature Resistance Temperature Detector Model CFTF-000-RTD-2-60-1-CC

To measure the temperature of the gas near the flow, Omega CFTF-000-RTD-2-60-1-CC high temperature resistance temperature detectors (RTDs) are used. The CFTF series are PT100, class B, thin-element DIN platinum. PT100 refers to a platinum element where 100 ohms corresponds to 0 °C. The class refers to the resistance tolerance of the PT100, with this class B element having $\pm(0.3 + 0.005*t)$ °C, where t is the measured temperature, or $100.00 \pm 0.12 \Omega$ at 0 °C. DIN is an acronym referring to the European standard as opposed to the American standard. This sensor meets the European standard within 0.1% DIN 43760. The 000 refers to the bend angle, which is zero, 2 is the probe length in inches, 60 is the cable length in inches, 1 refers to spade lugs, and CC refers to the high temperature option. The temperature range of the RTD is -50 C to 500 °C. The sensor has a three wire configuration per IE/ASTM-E-1137 code.

RTDs follow nonlinear sensing relationships. Proper resistance calibration dictates the overall accuracy of the sensor. Temperature range is the main factor in the determination of a proper curve fit. The high possible operation temperatures require a greater response range than a quadratic fit, up to 200 °C, or a cubic fit, up to 400 °C, allows. A rational polynomial function allows decreased error in temperature ranges up to 800 °C. The following rational polynomial function and coefficient table are used for this RTD:

$$T = c_0 + \frac{R_x(c_1 + R_x(c_2 + R_x(c_3 + c_4 R_x)))}{1 + R_x(c_5 + R_x(c_6 + c_7 R_x))} \quad [49]$$

Table 5. High Temperature RTD Rational Polynomial Function Coefficients

Coefficients							
C0	C1	C2	C3	C4	C5	C6	C7
-245.19	2.5293	-0.066046	4.0422E-03	-2.0697E-06	-0.025422	1.6883E-03	-1.3601E-06

Rational polynomial RTD calibration data, published by Mosaic Industries (59), provide calibrated temperature versus resistance measurements, as well as absolute error, per degree Celsius. Using these data, average error over the sensor range from -50 °C to 500 °C is 0.0144 °C. This value is lower than the 0.0151 °C from the overall range for this fit. The alpha number, 0.003850 Ω/Ω/°C, for the European standard RTD, is provided in these data as well as in Omega literature. The alpha number refers to the average relationship between temperature and resistance, also known as the temperature coefficient of resistance.

The sensors are shipped standard with spade lugs. To connect to the CR1000 data logger, the spades are cut and the remaining wire end is stripped. The color code is red/red/white. It is determined by means of excitation and measurement that the two red wires are branches of the same leading wire.

A half bridge command is used with the CSI CR1000 to describe the sensing mechanism in data logger communications. This means that an external resistance is added to the wiring arrangement, thereby using a known resistance to determine the unknown, measured resistance. To determine the appropriate external resistance to use in the circuit, operational and maximum current must be considered

in order to protect the logger. Excitation voltage and external resistance may be adjusted, within the constraints of the logger, to optimize measurement. Mosaic Industries data are again used as expected measured resistances at the minimum sensing temperature of $-50\text{ }^{\circ}\text{C}$, an ambient temperature of $23\text{ }^{\circ}\text{C}$, maximum sensing temperature of $500\text{ }^{\circ}\text{C}$, and higher than maximum operating temperature of $800\text{ }^{\circ}\text{C}$. These correspond to $80.31\ \Omega$, $108.96\ \Omega$, $280.98\ \Omega$, and $375.5\ \Omega$, respectively. In the following manner, it is determined that an excitation voltage of 1250 mV coupled with an external resistance of $20\text{k}\Omega$ provides an optimal combination over the operational temperature range.

$$V_x = IR_{x,\text{total}} \quad [50]$$

$$R_{x,\text{total}} = R_{x,\text{external}} + R_{x,\text{internal,meas}} \quad [51]$$

$$R_{x,\text{total}} = 20,000\ \Omega + (80.31, 108.96, 280.98, 375.5)\Omega \quad [52]$$

$$I = V_x/R_{x,\text{total}} \quad [53]$$

$$I = \frac{1.250\ V_x}{20,000\ \Omega + (80.31, 108.96, 280.98, 375.5)\Omega} \quad [54]$$

$$= 6.2250\text{E} - 5, 6.2161\text{E} - 5, 6.1634\text{E} - 5, 6.1348\text{E} - 5\ \text{Amps}$$

$$I_{\text{short}} = \frac{1.250\ V_x}{20,000\ \Omega} = 6.2500\text{E} - 5\ \text{Amps} \quad [55]$$

These measurements are then used to determine the step size in the logger measurement.

$$V_{x,\text{drop}} = IR_{x,\text{internal,meas}} \quad [56]$$

$$V_{x,\text{drop,min,-50C}} = (6.2250\text{E} - 5 \text{ Amps})(80.31 \Omega) = 0.004999 \text{ V} = 4.999 \text{ mV} \quad [57]$$

$$V_{x,\text{drop,maxop,500C}} = (6.1634\text{E} - 5 \text{ Amps})(280.98 \Omega) = 0.01732 \text{ V} = 17.32 \text{ mV} \quad [58]$$

$$V_{x,\text{drop,max,800C}} = (6.1348\text{E} - 5 \text{ Amps})(375.5 \Omega) = 0.02304 \text{ V} = 23.04 \text{ mV} \quad [59]$$

The voltage drop range is used to determine the voltage range in the three-wire half bridge code. Options embedded in the CR1000 include 10 mV, 25 mV, 250 mV. The 25 mV range is chosen. This voltage range covers the expected and extreme cases, without causing excessive step size. The final wiring schedule is shown in Figure 28.

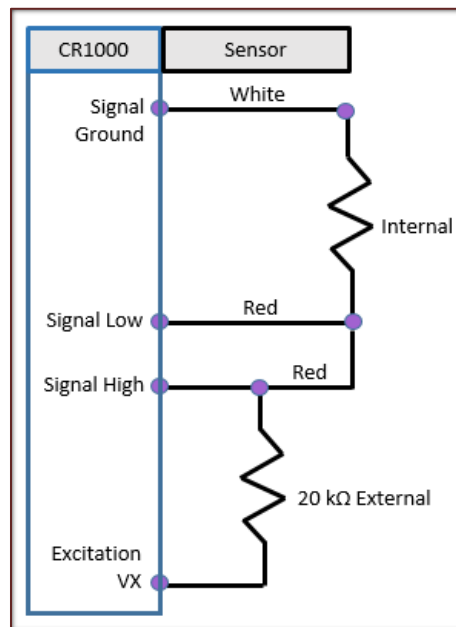


Figure 28. Omega CFTF-000-RTD-2-60-1-CC Resistance Temperature Device Wiring Schedule

There is no maximum excitation voltage or current published by Omega for this RTD. To assess self-heating in the sensor, the maximum voltage drop and associated current is used. The resulting power is $1.413\text{E-}6$ Watts. Self-heating is considered negligible at this very low level of power.

This sensor was tested in using the CSI CR1000 test box. Given the configuration described, the resulting measurement for the RTD was $108.60\ \Omega$ and $22.1\ ^\circ\text{C}$. The reference temperature measured $22.4\ ^\circ\text{C}$. This sensor is found to measure within the margin of error, $\pm(0.3 + 0.005*T)\ ^\circ\text{C}$, $0.41\ ^\circ\text{C}$ at this measurement temperature, or $2.8\ ^\circ\text{C}$ for the full temperature sensing range.

The RTD sensors are denoted sequentially based on each location in the system as RTD1, RTD2, etcetera, in reference to the system diagrams. They are located throughout, however, only at the inlet and outlet of the solar receiver.

5.4 Omega Pressure Transducer Model PX309-3KG5V

The Omega PX309 pressure transducer series is a stainless steel pressure transducer with a high-performance silicon strain gage bonded to the stainless steel diaphragm molecularly. The pressure of 3000 psig is denoted by 3KG, and the output of 0-5 Vdc is denoted by 5V. The sensor has an excitation of 9-30 Vdc and is reverse polarity and overvoltage protected. The accuracy is $\pm 0.25\%$ FS BSL (Full Scale Best Straight Line) measured at $25\ ^\circ\text{C}$, with hysteresis, linearity, and repeatability included in this calibration. The overall operating temperature range is $-40\ ^\circ\text{C}$ to $85\ ^\circ\text{C}$.

Due to the large excitation range this sensor allows, it is connected to the switched 12V channel in the CSI CR1000, allowing sensors with greater excitation sensitivity to be on open channels. The specifications denote a zero offset with a $\pm 2\%$ FSO (Full Scale Output), equivalent to the total error band. The measurement path is that of a single ended voltage, meaning that the ground is also used as the reference. The wiring schedule for the PX-309-3KG5V pressure transducer is displayed in Figure 29.

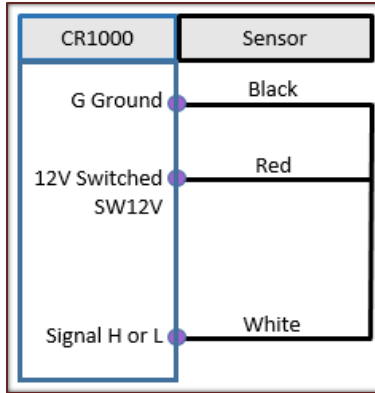


Figure 29. Omega PX309-3KG5V Pressure Transducer Wiring Schedule

This sensor requires a multiplier to achieve desired accuracy. This is calculated by plotting the output voltage range versus the designed pressure range of the sensor. The PX309-3KG5V sensor has an output voltage range of 0-5 V, and a pressure sensing range of 0-3000 psi. The resulting plot is displayed in Figure 30.

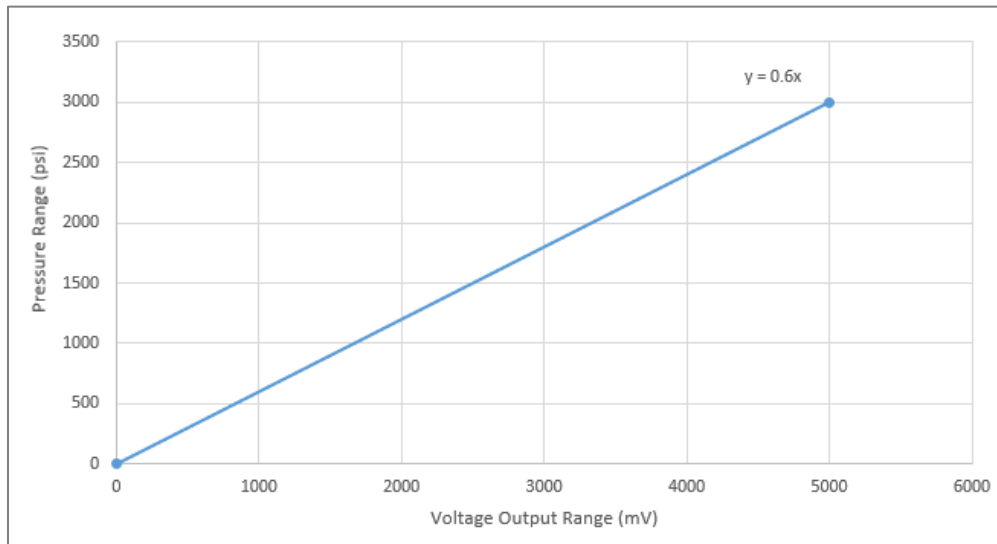


Figure 30. Omega PX-309-3KG5V Pressure Transducer Multiplier

The equation of the line is also given, showing a multiplier of 0.6. This multiplier is valid for units of psi. The unit psi is referenced to atmospheric pressure, where Pa is referenced to a vacuum; therefore, converting to Pa requires a multiplier that considers atmospheric pressure. In the calculations described by Equation 60, a reflective conversion factor is used.

$$M_{PX309} = 0.6 \frac{\text{psi}}{\text{mV}} * \frac{108219.76 \text{ Pa}}{1 \text{ psi}} = 64932 \frac{\text{Pa}}{\text{mV}} \quad [60]$$

These sensors are denoted as Om309_1c, Om309_2c, and Om309_2h, referenced for each location respective to the recuperators in the system drawings, and Om309_7 referenced to the installation location. The subscripts c and h refer to cold and hot flow.

5.5 Kulite Super High Temperature Pressure Transducer Model XTEH-10L-190SM

Very few sensors are capable of operating in the temperature range desired of this SCO₂ system. The Kulite super high temperature pressure transducer (SHTPT) provides a pressure sensing solution for fluid flow with temperatures between -54 °C and 500 °C. Although the sensor operates to temperatures up to 500 °C, life limitations are disclosed with constant operation above 454 °C. This sensor, designed by the manufacturer for turbine engine testing, possesses a fully active four arm Wheatstone bridge with patented dielectrically isolated silicon on silicon leadless technology. The rated excitation is 10 Vdc, with a maximum of 12 Vdc and damage to the sensor occurring with excitation exceeding 15 Vdc. The full scale output is 100 mV nominal. The accuracy is typically ±0.1% FSO BFSL (Full Scale Output Best Fit Straight Line) with a maximum of ±0.5% FSO.

A Kulite sensor is installed at the interface between the solar receiver outlet and the turbine inlet. In order to protect the device from higher than expected temperatures, it is installed in the system at the

terminal end of a four inch pigtail. Regarding pressure, this sensor is rated at 200 bara (20 MPa or 2900.75 psia) with a maximum pressure of 300 bara (30 MPa or 4351.13 psia). Different sensors were used due to availability and cost. The wiring designation is provided in the specification documentation. This designation, in relationship to the CSI CR1000, is displayed in Figure 31.

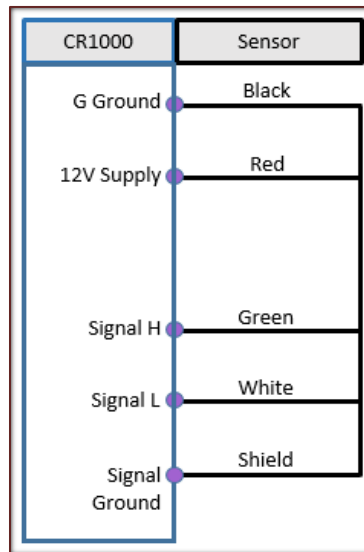


Figure 31. Kulite Super High Temperature Pressure Transducer Wiring Schedule

The calibration sheets indicate a 0.492 mV/bar sensitivity over a compensated temperature range of 80 °F (26.7 °C) to 850 °F (454 °C), with an excitation of 10 Vdc. The multiplier for this sensor is given by these sensitivity measurements and is calculated as follows:

$$M_{\text{Kulite1;200 Bara}} = \left(0.492 \frac{\text{mV}}{\text{bara}}\right)^{-1} = 2.0325 \frac{\text{bara}}{\text{mV}}$$

[61]

$$2.0325 \frac{\text{bara}}{\text{mV}} \left(\frac{100000 \text{ Pa}}{1 \text{ bara}}\right) = 203252 \frac{\text{Pa}}{\text{mV}}$$

The multiplier calculated based upon the calibration sheet, thus at 10 V excitation. In cases with excitation voltages other than 10 Vdc, multipliers may be calculated graphically. The sensor, however, yielded results with less accuracy when tested with a 12 Vdc supply. The reference pressure is estimated by using National Weather Service Data at McCarran International Airport (60). It was found that a 10 Vdc excitation is required to maintain the best expected accuracy of the device, where 0.5% FSO is 1 bara for this model.

5.6 Optical Rotational Speed Sensor Model

The optical rotational speed sensor is designed using a combination of a receiver and a laser. The receiver is a Photologic slotted optical switch, model OPB931W55Z. This is a photo integrated circuit switch with an opaque injection-molded plastic housing and a sensing shell of infrared transmissive plastic. The housing provides sensor resistance to ambient interference in the form of unwanted light in the visible and near infrared spectra. Both the sensor aperture and the emitter aperture measure 1.27 mm (0.05 in). The sensor has a buffered open collector output, requiring the electrical configuration displayed in Figure 32, as provided by Photologic (61).

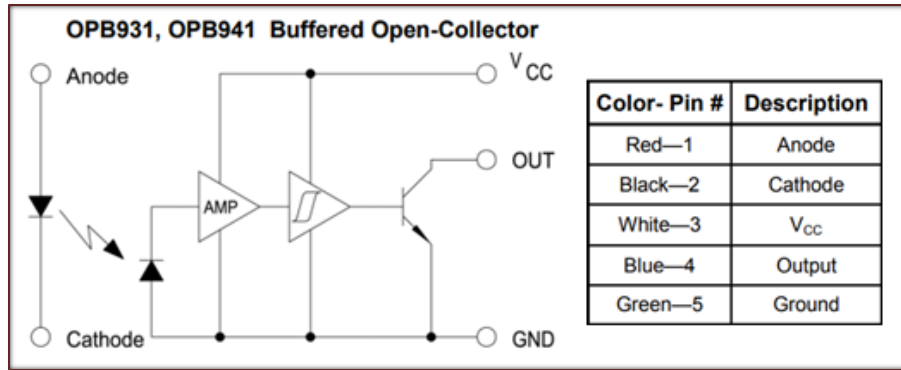


Figure 32. Photologic Slotted Optical Switch Wiring Schedule (61)

A 10 Vdc supply voltage is recommended, but not to exceed three minute intervals. Due to data collection intervals longer than three seconds, tests were conducted for longer operation at lower voltages. It was found that appropriate data collection intervals are possible with a 5 Vdc supply voltage with negligible sensitivity loss when coupled with a green light laser. The operating temperature is up to 70 °C, requiring sensor mounting in the shade and surrounded by minimally obstructed air flow.

The coupled laser is a Q-Baihe Green Laser Dot Diode Module, model 532MD-30-TTL-LM. The green laser is defined by a 532 nm wavelength, receives a 5 Vdc working voltage, and has a 30 mW power output. The dot laser style couples well with the receiver module. There is a recommended duty cycle of 45 seconds on and 15 seconds off. Through testing, it is found that longer duty cycles are possible with a 3 Vdc input, while maintaining the capability of the receiver to detect the light.

In order to allow this optical pair to count shaft rotations, a Rayotek sight window, model 722-High Pressure-Fused Glass, part number 101012, provides the light pathway. This is a 4000 psi rated, glass window fused into a stainless steel 316 housing with a ¼” NPT fitting. A window is installed on the turbomachinery casing, 180° apart, allowing light to pass through a passage fabricated through the casing

and shaft. The passage through the shaft creates two counts per rotation; therefore, this is adjusted in the final rotational speed measurement.

5.7 Rheonik Coriolis Flow Meter Model RHE08

The Rheonik Coriolis Flow Meter is used to calculate mass flow rate, the total mass passing through the device, and the density. As is typical of Coriolis flow meters, this device calculates mass flow by measuring the force resulting from a generated Coriolis acceleration. The mass flow rate and density are set to analog outputs of 4-20 mA, using a 250 ohm precision resistor. This resistor yields a 1-5 Vdc logger output range. The wiring schedule is displayed in Figure 33, where mass flow rate is loop 1 and density is loop 2. The mass totalizer uses a pulse output.

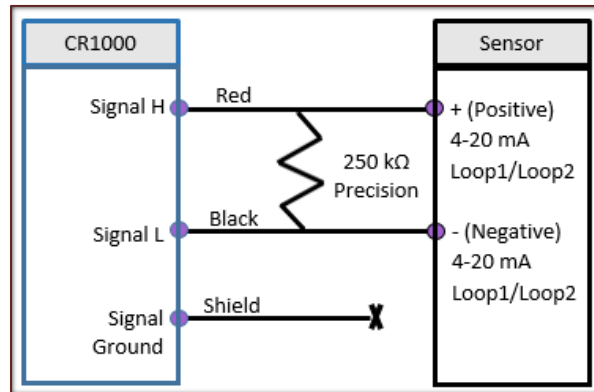


Figure 33. Rheonik Coriolis Mass Flow Meter 4-20 mA Output Wiring Schedule

The flow meter has two components, an RHM Coriolis flow sensing device and an RHE flow transmitter control module. The sensing device is installed with a minimum 5 in straight tube on entry and exit, in the cold side flow path. Maximum fluid temperature cannot exceed 210 °C, and the system is sensitive to temperature shocks. The manufacturer recommends that temperature increases occur at a

maximum rate of 1 °C per second, and a maximum temperature difference across the sensor of 50 °C.

The control module is powered by 115 Vac. The accuracy of the flow meter is 0.1% of the flow rate.

5.8 Sensing System Overview

The notations used in the code relate to sensor model or specific positions of each in the system, or both. Table 6 is a comprehensive list of the sensing devices in the overall system. This table can be cross-referenced with the system drawing, Figure 1, to provide an outline of the overall sensing system.

Table 6. Full System Sensor List

Sensing	Drawing Notation	Type	Sensor Model
Pressure	PA	Pressure Transducer	Omega PX309-3GK5V
	PB	Pressure Transducer	Omega PX309-3GK5V
	PC	Pressure Transducer	Omega PX309-3GK5V
	PD	Pressure Transducer	Omega PX309-3GK5V
	P1	Pressure Transducer	Omega PX309-3GK5V
	P2	Pressure Transducer	Omega PX309-3GK5V
	P3	Pressure Transducer	Omega PX309-3GK5V
	P4	SHT Pressure Transducer	Kulite XTEH-10L-190SM-200BARA
	P5	Pressure Transducer	Omega PX309-3GK5V
	P6	Pressure Transducer	Omega PX309-3GK5V
P7	Pressure Transducer	Omega PX309-3GK5V	
Temperature	TC	Resistance Temperature Device	Omega CFTF-000-RTD-2-60-1-CC
	T1	Resistance Temperature Device	Omega CFTF-000-RTD-2-60-1-CC
	T2	Resistance Temperature Device	Omega CFTF-000-RTD-2-60-1-CC
	T3	Resistance Temperature Device	Omega CFTF-000-RTD-2-60-1-CC
	T4	R-Type Thermocouple	Omega XIN-P13R-U-187-24-M-TJ-BX-4
	T5	R-Type Thermocouple	Omega XIN-P13R-U-187-24-M-TJ-BX-4
	T6	Resistance Temperature Device	Omega CFTF-000-RTD-2-60-1-CC
	T7	Resistance Temperature Device	Omega CFTF-000-RTD-2-60-1-CC
Tc1-Tc8	J-Type Thermocouple	Omega XCIB-J-1-3-10	
Rotational Speed	RPM	Optical Switch	Photologic OPB931W55Z
	RPM-L	Laser	Q-Baihe 532MD-30-TTL-LM
Mass Flow Rate	RHE08-MF	Coriolis Device	Rheonik Coriolos RHE-08
Density	RHE08-D	Coriolis Device	Rheonik Coriolos RHE-08

CHAPTER 6. DATA COLLECTION METHODS

Preliminary data have been collected on the solar receiver and air cooled heat rejection heat exchanger. These data were collected by specifically chosen temperature and pressure sensors and a mass flow meter, connected to a Campbell Scientific Incorporated Model CR1000 Data Logger (CSI CR1000). The sensor network includes temperature and pressure between every segment of the system, as well as mass flow and density, as described in Chapter 5 of this document. Actuated valve flow control has been added to the system for full system testing. Full system testing is to take place with Programmable Logic Controller (PLC) data collection and system control.

6.1 Campbell Scientific Incorporated Model CR1000 Data Logger (CSI CR1000)

A CSI CR1000 test box was connected to test the connection and functionality of each of the sensors. As the software of the CSI CR1000, LoggerNet code contains data logger communication requirements that vary for each sensor and sensor type. The test box provided a means to test code performance and to evaluate the accuracy of multiplier calculations for each sensor. The test box is shown with one of the test connection configurations in Figure 34. In the test case shown in this figure, three J type thermocouples are wired and coded in series, one RTD 3 wire bridge, and three different pressure transducers are tested. This test box was used to verify the multipliers and measurement accuracy of nearly every sensor.

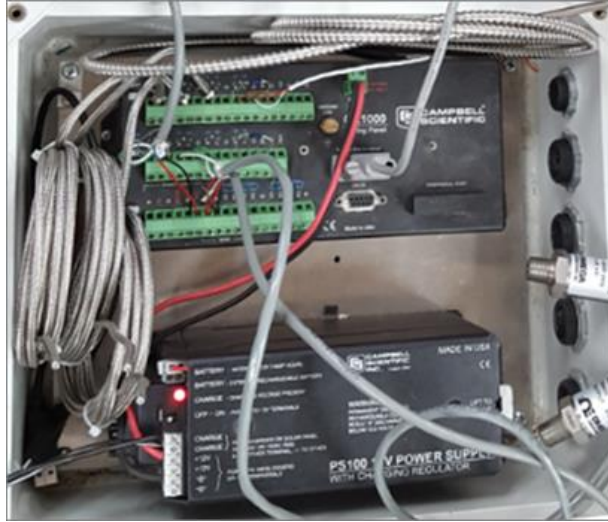


Figure 34. Campbell Scientific Inc. CR1000 Sensor Test Box

Preliminary system data were also collected with a CSI CR1000 collection system. In system testing, a similar configuration was used, with the addition of a Campbell Scientific AM16/32 Multiplexer. The multiplexer housed all thermocouple sensing devices, allowing room for other sensors to be connected directly to the CSI CR1000.

6.2 Siemens Model S7-1200 Programmable Logic Control (PLC)

Programmable Logic Controllers provide great flexibility in data collection and system control, with much faster scan times compared to other systems. The default scan time for the S7-1200 PLC is 150 ms; the minimum and maximum scan times are 1ms and 6000 ms, respectively. For comparison, the scan time for the Campbell Scientific CR-1000 is drastically limited to 30 s when combined with an AM16/32 Multiplexer. This is not an issue for temperature and pressure data collection under steady state operation, however, is much too slow to measure the rotational motion of the shaft. Furthermore, the PLC allows for system control, which is required to assure the fluid remains in the supercritical phase. Initial PLC base configuration was completed with significant work from Paolo Ginobbi. Initial design conditions,

sensor connections, safety measures, additional thermocouple modules, the specialized 10 V power supply, and other modifications were made by this research team. The final PLC, with connections, is displayed in Figure 35. The PLC is designed to control the start-up sequence, maintain the minimum pressure of the system by a feedback loop combined with control of a CO₂ booster pump, monitor and control system operation by valve control, and both supply power to and collect data from all sensors.

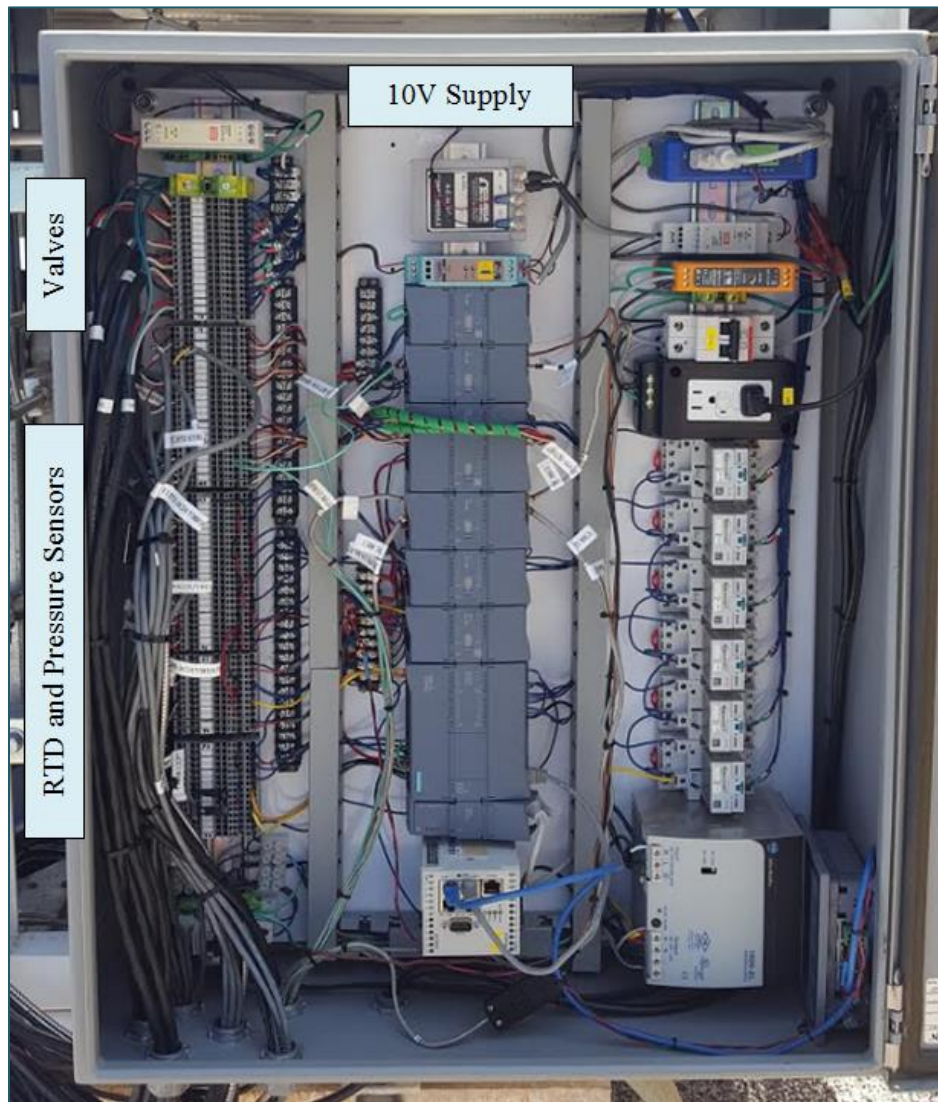


Figure 35. Completed Programmable Logic Controller Hardware View

CHAPTER 7. RESULTS

Results for this system are multifaceted, as is expected for a system composed of many parts. Turbine and compressor impeller performance are analyzed using both ANSYS software, as well as a mathematical approach, backed by the resulting velocity diagrams, which are also included. The solar receiver is experimentally analyzed, coupled with the performance of the air cooled receiver. Each analysis provides insight to the expected outcome of the overall system.

7.1 ANSYS Compressor and Turbine Velocity Profile

ANSYS software provides analysis of fluid flow in their Fluent suite. Fluent uses a finite difference method to analyze and describe the flow. Chen and Liu (62) relate finite difference to a LEGO build. The finite element model breaks the flow into a number of finite elements, as a LEGO robot is a number of LEGO pieces. The number of elements, or pieces, must be such to realistically define the goal, without the need to go beyond that number. In Fluent, the number and distribution of the elements are called the mesh. The software is capable of generating a mesh based on the flow geometry. This mesh can be used or optimized for a particular need or application.

7.1.1 ANSYS Model Framework and Results

The flow geometry must be defined in the software. ANSYS provides a design modeler workspace where geometry can be created or imported. The CAD capabilities are found to be less user-friendly than software designed specifically for computer animation. However, imports must be in compatible file formats, like IGS. Additionally, the key is to define the flow area, and not the solid area as is generated in SolidWorks, for example. One way to resolve this is to create a fluid space beyond the solid space, using a Boolean in the ANSYS design modeler to subtract one from the other. This works well as long as the solid is one part and not an assembly of parts. The very small space existing between the components in an assembly create fluid space that is recognized by Fluent. Furthermore, it is best to trim the solid to

avoid any tiny fluid spaces that may be recognized. An example of this is shown in Figure 36. In this figure, the flow area is shown in gray and the solid is displayed in green. The compressor blade, viewed on the left, shows an integration of green and gray at the base. This is a visual display of leakage in that part of the geometry. In order to remove this, the parts and flow geometries must be altered as shown in the turbine visual on the right. The modification is completed for each impeller geometry within SolidWorks, and is then saved and imported as an IGS file.

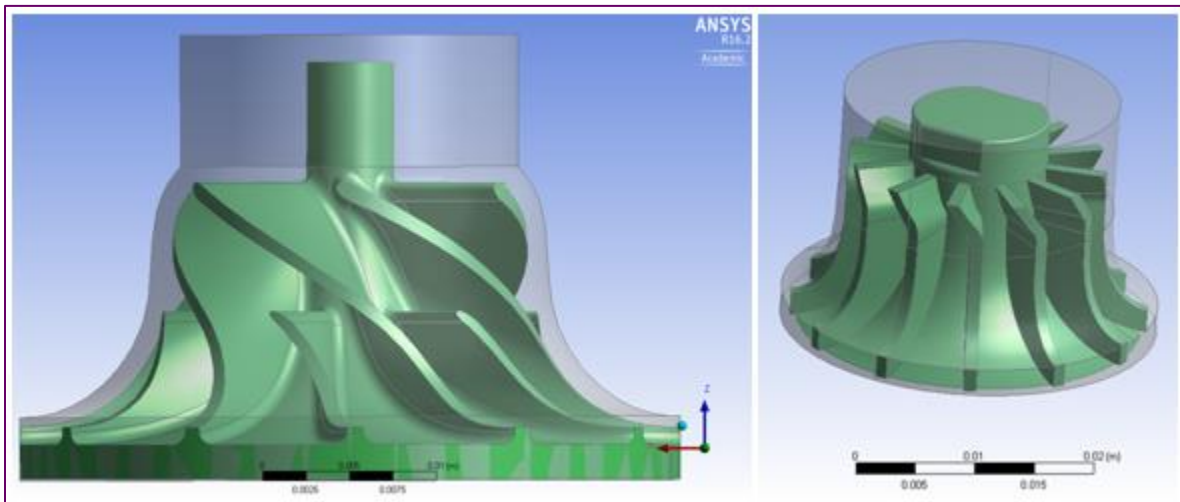


Figure 36. ANSYS Flow Area as Defined for the Compressor (left) and Turbine (right)

Once the flow area is defined, the project is updated and the mesh is generated. The mesh defining the elemental distribution of the flow area is shown in Figure 37. Overall, the mesh is denser in the compressor, shown left, than in the turbine, shown right. This is due to the increased geometric complexity of the compressor blade. Additionally, the mesh in both blades is denser near the flow boundaries.

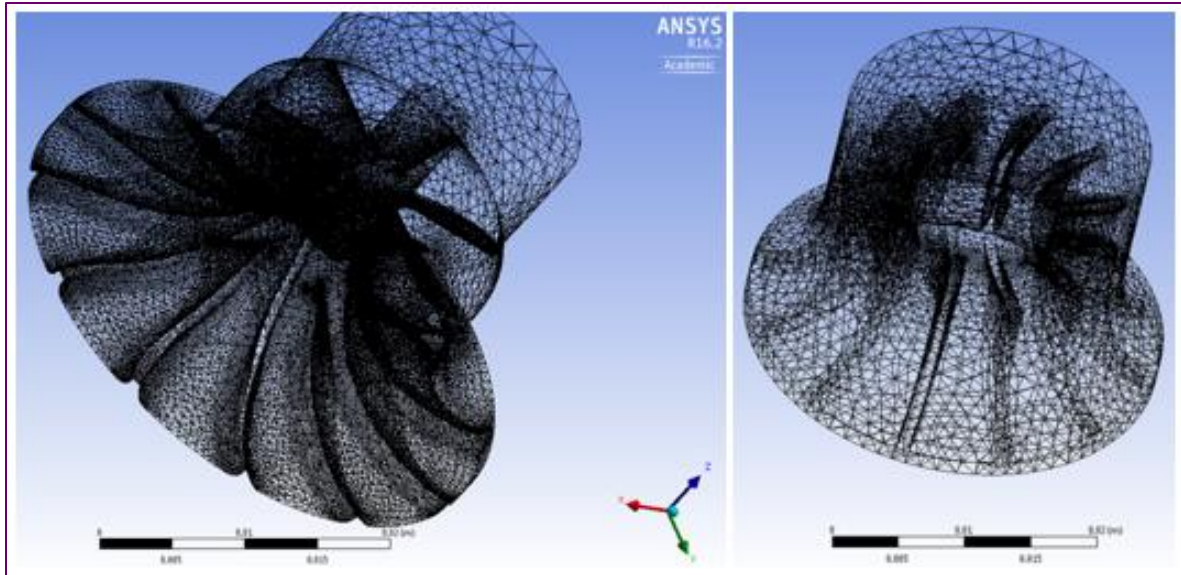


Figure 37. Compressor Mesh (left) and Turbine Mesh (right)

The inlet and outlet modes are defined, with the inlet being the datum for both blade analyses. Carbon dioxide is chosen as the working fluid and the properties are user defined. ANSYS provides limited property values, specifically for those under a non ideal gas assumption at standard temperature and pressure. The values entered were provided by EES, and in turn NIST. The boundary condition defining the inlet is mass flow rate for both impellers, and a pressure outlet defines the boundary condition at the exit. The inlet for both blades is described by a mass flow rate of 0.16 kg/s and 1.22 kg/s, providing information for both a low flow condition and the design point condition. The velocity/mass flow based entrance and pressure based exit allows the system to adhere to balance equations. The actual inlet and outlet surfaces are selected and named, and the entrance angle can be defined by a degree value or as normal to the inlet surface. The interior surface and the wall surface are defined as solid surface boundary conditions.

Solutions were generated using a viscous model and laminar flow. Verification of the laminar flow assumption is given by the design point, calculated Reynolds number. Calculated at the compressor inlet and the turbine exit, the Reynolds numbers are $8.68E5$ and $1.91E6$, respectively. Both of these describe laminar flow.

The solution method used is a simple pressure-velocity coupling. The spatial characteristics are defined by a second order pressure, a least squares cell based gradient, and a second order upwind momentum discretization. ANSYS allows results to be displayed in a variety of ways. For this model, the focus was on the velocity and streamline profiles. Both graphical solutions allow the user to reduce or increase the number of data points shown in each graph, regardless of the amount of data generated.

The velocity profile for the compressor is shown in Figure 38 and Figure 39, for 0.16 kg/s and 1.22 kg/s mass flow rates. These mass flow rates are the original low flow initial value and the design point condition. For the low flow condition, the maximum velocity is 15.68 m/s , and for the design point, the maximum velocity is 118.1 m/s , both occurring near the compressor inlet and at the blade interface. The flow here is defined as entering normal to the surface, where the larger circle minus the smaller circle, defining the shaft, is the flow inlet area. According to the graph, flow build-up occurs most significantly at each half-blade. The flow velocity also shows a greater decrease just past the right side half-blade transition area when compared to the left. Zero or near zero velocity is demonstrated in this flow regime as well, where zero velocity is noted by darker blue velocity vectors. Zero or near zero flow in the mid region is undesirable; however, this is expected at the blade surface. Reduction in this phenomenon could be achieved by shortening the half-blade length; though, the trade-off would be a reduction in flow guidance. At the blade exit, the velocity, in general, flows around a mean value of 7.84 m/s for the low flow condition, and around a mean value of 50 m/s . Using ANSYS modeling, it becomes clear that control of the mass flow rate provides strong control of the system.

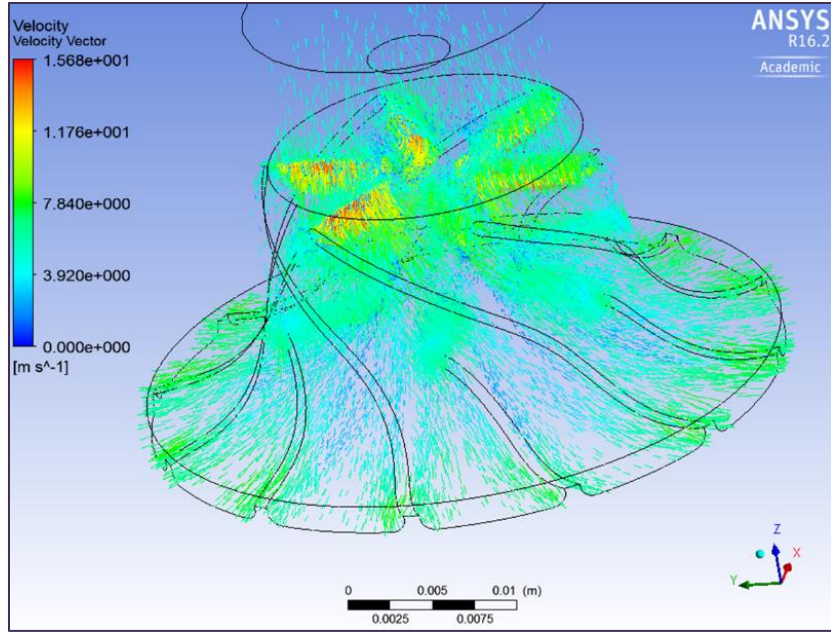


Figure 38. Compressor Flow Area Velocity Profile for Mass Flow Rate 0.16 kg/s

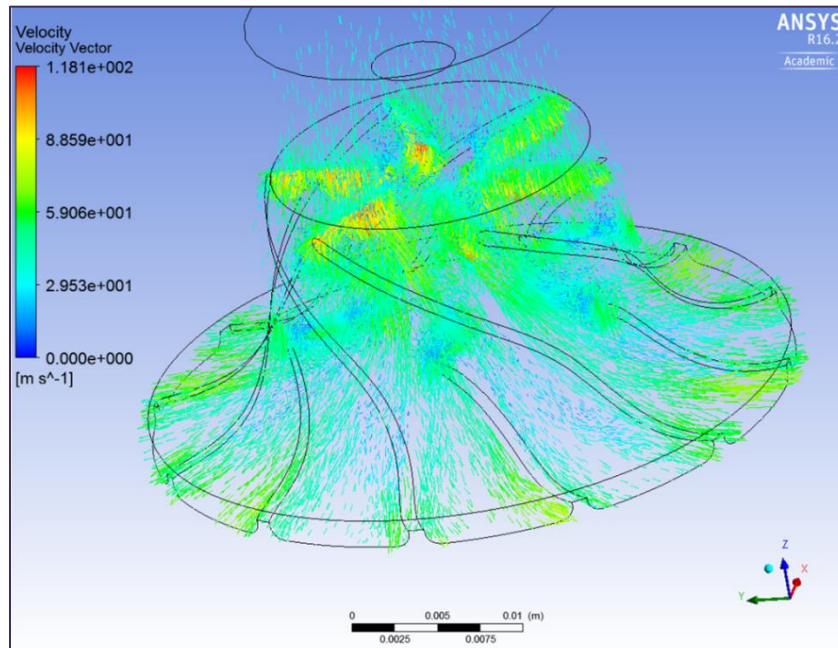


Figure 39. Compressor Flow Area Velocity Profile for Mass Flow Rate 1.22 kg/s

The streamline graph is used to verify flow patterns. The compressor streamline profile for the low flow condition is displayed in Figure 40. This graphical analysis reiterates the flow interruption located around the half-blade interface. Optimization of flow should include an engineering analysis of the location and size of the compressor half-blades.

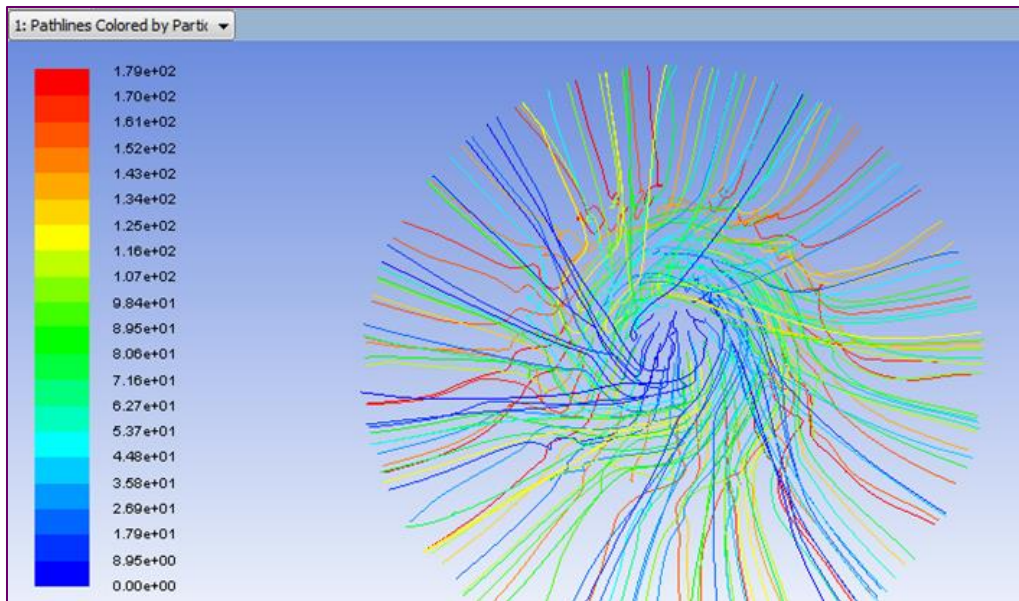


Figure 40. Compressor Flow Area Streamline Profile

The velocity profile for the turbine is shown in Figure 41 and Figure 42, for the low flow condition of 0.16 kg/s and the design condition of 1.22 kg/s, respectively. The profile displays an increase in velocity as the fluid enters the blade, shown by yellow and minimal red vectors at the blade interface. Red vectors define the maximum velocity in the flow area, valued 11.64 m/s for the low flow condition and 89.2 m/s for the design flow condition. Zero velocity is not significant in this flow regime, though the streamline profiles display flow interruption at the blade surface, as described below. The exit velocity, being eclectic, can be viewed as the velocity closer to the geometric end of the model. In this space, the

estimated bulk velocity appears to be rather consistent, yielding 5.8 m/s and 44.6 m/s for the low flow and design conditions. There exists obvious flow congestion at the blade curvature; however, it does not appear to have a detrimental effect. It may be beneficial to redesign the curvature slightly to maximize functionality of the flow.

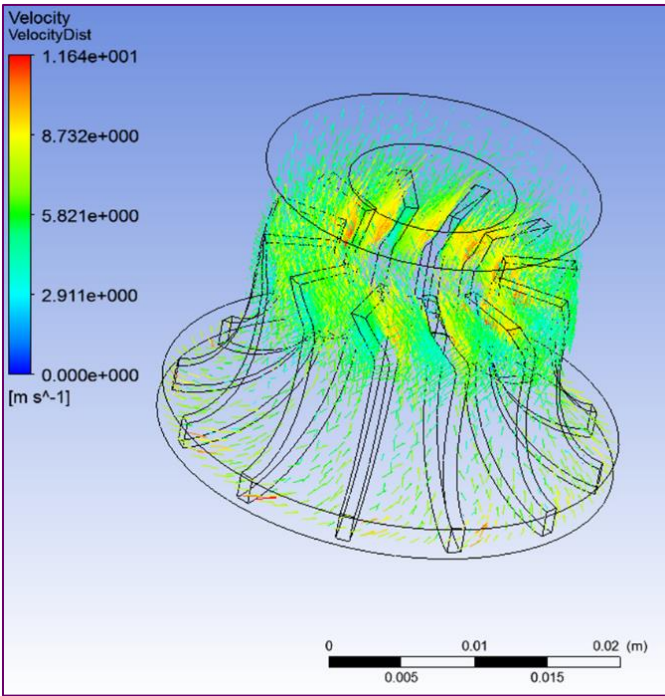


Figure 41. Turbine Flow Area Velocity Profile for Mass Flow 0.16 kg/s

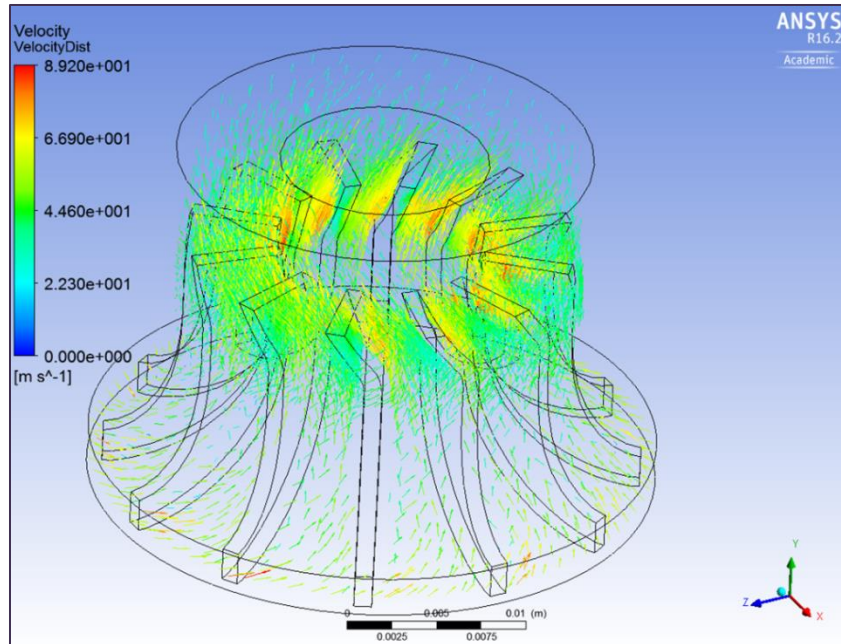


Figure 42. Turbine Flow Area Velocity Profile for Mass Flow 1.22 kg/s

The streamline profile for the turbine under the design condition is displayed in Figure 43. Zero or near zero velocity streamlines are shown. These zero streamlines occur at the blade boundary. This flow regime is different from that displayed for the compressor. The majority of these zero magnitude streamlines end at the blade surface geometry and may be viewed as force exerted on the blade. The lines also display some flow interruption at the blade curvature, though the overall velocity profile is similar to that which is expected.

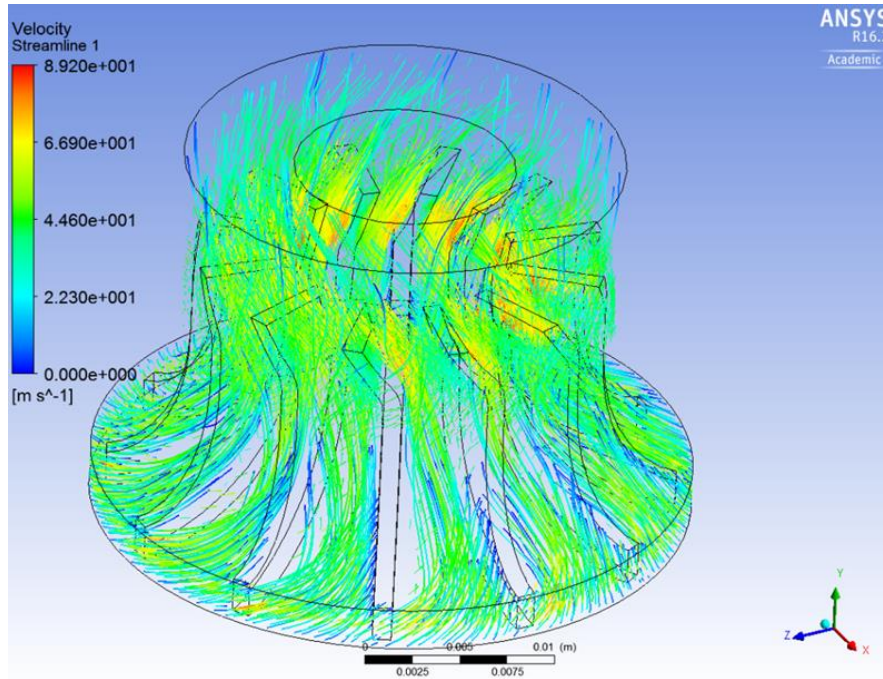


Figure 43. Turbine Flow Area Streamline Profile

7.1.2 ANSYS Conclusions

The overall system model for both the compressor and the turbine was successful. ANSYS provided the velocity profile in vector and streamline form, presenting a method of internal analysis for both impellers. The general flow pattern in both analyses is as expected, where flow changes correspond to geometrically induced path changes. The turbine blade shows a more evenly distributed increase, decrease, and then increase in flow velocity, as compared to the compressor blade. This is due to the geometric difference in the blades. The density of mass flow vectors near the smaller diameter side of each blade, regardless of flow direction, show that the fluid is being compressed through the compressor and expanded through the turbine. The limitation of ANSYS modeling is the lack of thermophysical fluid property data near and above the critical point for carbon dioxide.

The low mass flow rate for the model provides a baseline for velocity profiles in the system. The maximum fluid velocity is noted by the model 15.68 m/s and 11.64 m/s across the compressor and turbine, respectively. This indicates that there is a large margin to increase the mass flow rates across each impeller, while maintaining low Mach number flow. The maximum fluid velocity for the design condition, 1.22 kg/s, is 118.1 m/s and 89.2 m/s across the compressor and turbine, respectively. As previously mentioned, these results show that control of the mass flow rate provides significant system operational control.

The ANSYS results will be used to optimize any blade redesign. New designs will be modeled in Fluent and analyzed prior to machining. Additionally, ANSYS provides software solutions for calculating the dynamics of turbomachinery at the next level. Design rotation conditions can also be modeled to provide an expectation of power generation.

7.2 Solar Receiver Preliminary Material and Temperature Test Results

The solar receiver was tested in two phases. The first was with a small test segment of receiver tubing in a two coil pass configuration for material temperature tolerance. The receiver test section was connected onto the solar receiver area, unaccompanied by any other components. Thermocouples were placed on the outer wall and hanging inside the tube of the small receiver test segment. The SAIC dish was then positioned on-sun. The results, displayed in Figure 44, show that all three thermocouples reach 900 °C in less than five minutes. In the figure, the quick increases occur as soon as the SAIC dish is placed on sun, declining when it is returned to the off-sun position. The near horizontal line shows the direct normal irradiance during the time of the test, approximately 930 W/m².

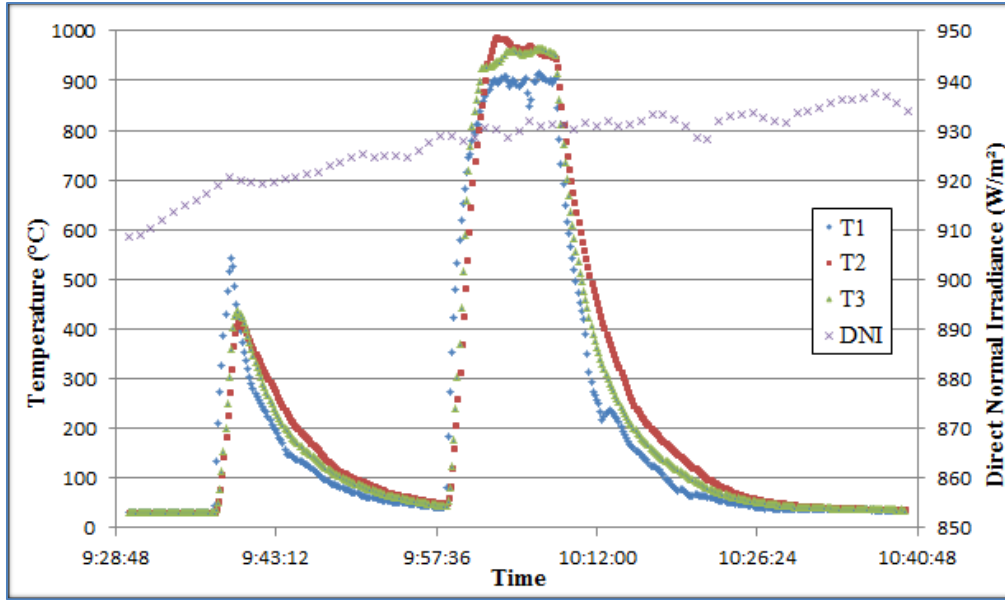


Figure 44. Solar Receiver Segment Material Test

These results indicate that the thick-walled, stainless steel tube is capable of withstanding the high temperatures the high solar flux of the SAIC dish concentrator provides. The test segment displayed discoloration; however, the segment did not display visible deflection or evidence of material integrity loss. Secondly, this test shows that the system is able to reach desired temperatures, controlled by mass flow. Additionally, these high temperature responses show promise for transient cloud compensation.

7.3 Solar Receiver and Heat Rejection Test Results

The second phase of solar receiver testing occurred in conjunction with a heat rejection test of the ACHEX. In this test, an open loop configuration with nitrogen gas was used. The goal was to determine the high temperature capabilities of the receiver and to determine whether then designed size of the ACHEX sufficiently rejects heat. RTDs and pressure transducers were used at the receiver inlet, receiver outlet, which feeds the ACHEX, and ACHEX outlet. The pressure transducer placed at the exit of the

receiver is unique due to the expected temperature. A Kulite high temperature pressure transducer is used at this location.

The results show that both components are able to reach the desired goals. The nitrogen gas passing through the UNLV receiver reaches a recorded temperature over 700 °C. The outlet temperature of the air cooled heat rejection heat exchanger is able to cool the gas to within the margin of error of the receiver inlet temperature, or ambient conditions. These data are collected at low flow rates, which are both driven and limited by pressurized nitrogen tanks. The flow rate, measured by a Coriolis flow meter, is shown on the right vertical axis, and in yellow. These and the three RTD data results are displayed in Figure 45. As shown in the figure, the blue and green lines, corresponding to the receiver inlet and the ACHEX outlet temperatures respectively, maintain a similar temperature throughout the duration of the test. This shows the ACHEX is capable of sufficiently cooling the solar heated, high temperature gas. Further, it is shown that once the system is in the on-sun position, a high receiver gas temperature can be achieved in less than 7 minutes. This temperature may be controlled with mass flow once the system is tested in a closed loop.

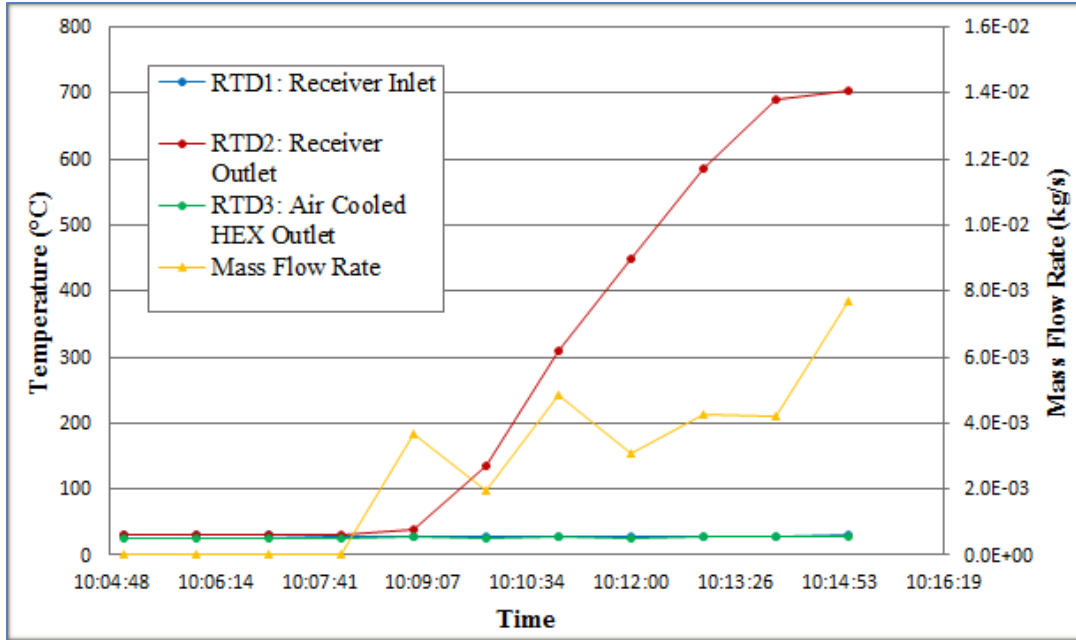


Figure 45. On-Sun Solar Receiver Temperature, ACHEX Temperature, and Mass Flow

7.4 Turbomachinery Velocity Diagram and Performance Analysis

In closed systems with no forced fluid flow, the actual mass flow rate and rotational speed are connected, and are dependent on operational conditions. Operational conditions and performance evaluation of a centrifugal compressor is fundamentally expressed by means of the velocity diagram for the impeller. A centrifugal compressor transfers mechanical energy to the fluid in the form of a static pressure rise by means of angular momentum. Smaller changes in temperature and fluid velocity are also results of the energy conversion, though they are less desirable. In an effort to achieve additional static pressure gains, a diffuser vane section at the impeller outlet provides a gradual increase in flow area, decreasing the velocity of the fluid and increasing the static pressure rise, while directing flow. Similarly, the velocity triangle provides information characterizing the power output by the machine. Velocity triangles for both components can be used to describe angular momentum and energy transfer.

7.4.1 Turbine Velocity Triangles

Impeller radii dimensions and the rotational speed of the shaft determine the base calculations for the velocity triangle and turbine analysis. The rotational speed, ω , used for the shaft is the design point calculation 44,527 rpm. The defining radii are as follows: hub radius, $r_{h,t}$, 0.23 in (0.00584 m); impeller eye, or exit, radius, $r_{3,t}$, 0.43 in (0.01092 m); and impeller inlet radius, $r_{2,t}$, 0.59 in (0.01499 m). The impeller velocity at the inlet, $U_{2,t}$, and exit, $U_{3,t}$, are calculated in Equations 62 and 63. The mean exit blade velocity is also useful for the impeller analysis. The mean blade exit velocity is the average velocity across the blade releasing the fluid. This is computed in Equation 64.

$$U_{2,t} = 2\pi r_{2,t} \omega = 2\pi(0.01499 \text{ m})(44,527 \text{ rpm}) \left(\frac{1 \text{ min}}{60 \text{ s}} \right) = 69.9 \text{ m/s} \quad [62]$$

$$U_{3,t} = 2\pi r_{3,t} \omega = 2\pi(0.01092 \text{ m})(44,527 \text{ rpm}) \left(\frac{1 \text{ min}}{60 \text{ s}} \right) = 50.9 \text{ m/s} \quad [63]$$

$$U_{3m,t} = 2\pi r_{3m,t} \omega = 2\pi(0.00838 \text{ m})(44,527 \text{ rpm}) \left(\frac{1 \text{ min}}{60 \text{ s}} \right) = 39.1 \text{ m/s} \quad [64]$$

The flow at the inlet of the turbine enters in the radial direction for radial inflow turbines such as this one. The velocity triangle defining the turbine inlet is displayed in Figure 46, and shows this relationship. As a result, mathematically, any reasonable blade speed can be combined with any reasonable fluid velocity without discontinuity or mismatch with the geometry of the blade. Flow discontinuity or mismatch results in off-design operation. Off-design operation reduces efficiency due to undesirable flow conditions and can cause additional stress on the impeller. In order to match flow conditions with the turbine geometry, the velocity triangle at the turbine exit is analyzed.

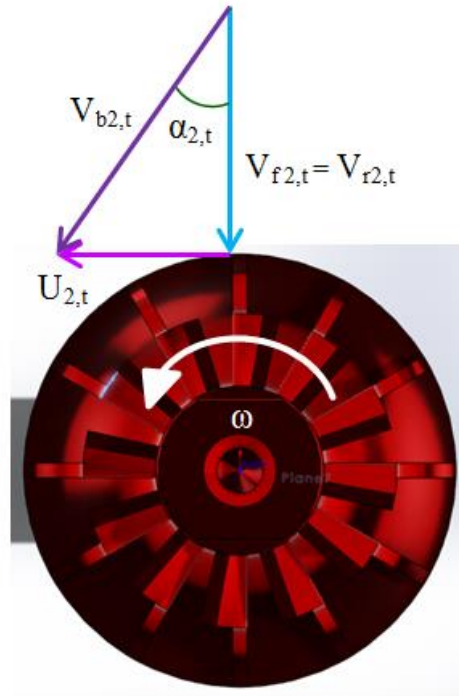


Figure 46. Radial Inflow Turbine Inlet Velocity Triangle

The velocity triangle describing the turbine impeller exit is displayed in Figure 47. The flow velocity at the exit of the turbine is calculated by using the flow area defined by the difference between the impeller eye diameter and the impeller hub diameter. The exit flow velocity is designed at 239.2 m/s, the impeller tip velocity at the exit is 50.9 m/s, and the mean impeller velocity at the exit is 39.1 m/s.

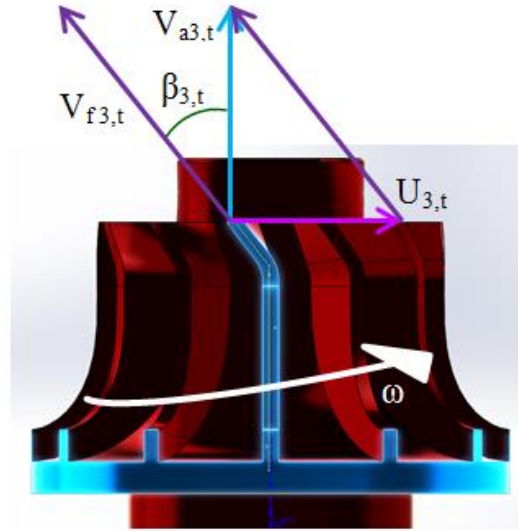


Figure 47. Radial Inflow Turbine Exit Velocity Triangle

Backward curved blades at the impeller exit can reduce the stress exerted by the fluid along the length of the blade tip. The curved blade at the impeller exit yields a 37.8° beta angle. The fluid is released from the turbine at this angle. Mathematical analysis using impeller tip speed, fluid velocity and the standard Pythagorean Theorem yields a 233.74 m/s axial flow velocity, V_{a3t} . Upon verification, the beta angle required for the described flow is 12.3° . It is clear that there exists a mismatch.

Reevaluation of the rotational speed using the beta angle and the fluid velocity is as follows:

$$U_{3,t} = V_{f3,t} \sin \beta_{3,t} = \sin(37.8^\circ) 239.2 \text{ m/s} = 146.6 \text{ m/s} \quad [65]$$

$$N = \frac{60U_{3,t}}{\pi D_{eye}} = \frac{60 * 146.6 \text{ m/s}}{\pi * 0.02184 \text{ m}} = 128,202 \text{ rpm} \quad [66]$$

This rotation speed is much too high for the designed machinery; thus, reevaluation of the fluid velocity is calculated using the impeller tip speed, 50.9 m/s, and the beta angle given by the impeller

geometry. Reorganization of Equation 65 yields a fluid velocity of 83.1 m/s. Fluid velocity is defined by the mass flow rate, density, and cross sectional flow area. Density is determined by the temperature and pressure conditions at the turbine exit, and cross sectional area is determined by the fabricated geometry. Therefore, for a given fluid velocity, the mass flow rate must be altered, and is calculated by Equation 67 to be 1.22 kg/s. Similarly, the mean exit blade speed yields a mass flow rate of 0.939 kg/s. The exact beta angle at the midpoint between the eye and hub of the turbine impeller is not accurately measured in SolidWorks due to the inability to reasonably create accurate relations at that point; therefore, in order to maintain continuity between flow and impeller geometry, the 1.22 kg/s flow rate will be used further analysis.

$$\dot{m} = V_{f3,t} \rho A_{3,t} = 83.1 \text{ m/s} * 55.11 \text{ kg/m}^3 * 2.67\text{E} - 4 \text{ m}^2 = 1.22 \text{ kg/s} \quad [67]$$

Flow at the inlet of the turbine enters in the pure radial direction in a radial inflow turbine. The velocity triangle describing the fluid entering the turbine is displayed in Figure 46. The angle labeled alpha between the radial and the absolute flow velocities is defined by the radial flow velocity and the blade speed. The fluid velocity relative to the impeller at the inlet is calculated using the tube diameter for design conditions; however, this does not define the actual total flow path area. The shroud diameter also does not characterize the flow area due to the fact that the fluid enters through a volute into small directed channels that are not characterized by the relatively large diameter of the impeller. Therefore, when blade geometry is known in its entirety, the characteristic flow area is determined by the impeller shroud, or inlet, diameter and the blade height, by Equation 68.

$$A_{s,t} = \pi D_{2,t} b_{h2,t} \quad [68]$$

The exact blade height for the fabricated turbine shroud is determined by the dimension tool in SolidWorks, and is 0.079 in (0.002007 m). The radial flow velocity entering the turbine can be described

by the geometric characteristic flow area calculated from Equation 68, $1.89\text{E-}4 \text{ m}^2$, the density at the inlet, 88.14 kg/s , and the mass flow rate, 1.22 kg/s . The inlet flow velocity, calculated by these parameters, is 73.2 m/s . This is much lower than the previously designed maximum inlet velocity of 452.79 m/s , predominantly reduced by the lower mass flow rate, but also by the accuracy of the characteristic flow area. Calculations using the inlet velocity triangle yield an alpha angle of 43.7° , and an absolute velocity, $V_{b2,t}$, of 101.2 m/s . An alpha angle very close to 45° mathematically shows nearly pure radial inlet flow, as desired. This very small off-design influence, coupled with inlet conditions based upon on-design outlet conditions, shows continuity in flow across the turbine.

7.4.2 Further Turbine Analysis

The relationships between states and fluid velocities that define a radial inflow turbine are shown by a T-s, or temperature-entropy, diagram. A standard T-s diagram is shown in Figure 48. As shown, V_t is the resultant or absolute velocity, V_f is the fluid velocity whose direction is defined by the blade angle, and U is the impeller velocity. Numerically, state 1 is the nozzle entry, state 2 is the nozzle exit and impeller entry, state 3 is the impeller exit and diffuser entry, and state 4 is the diffuser exit.

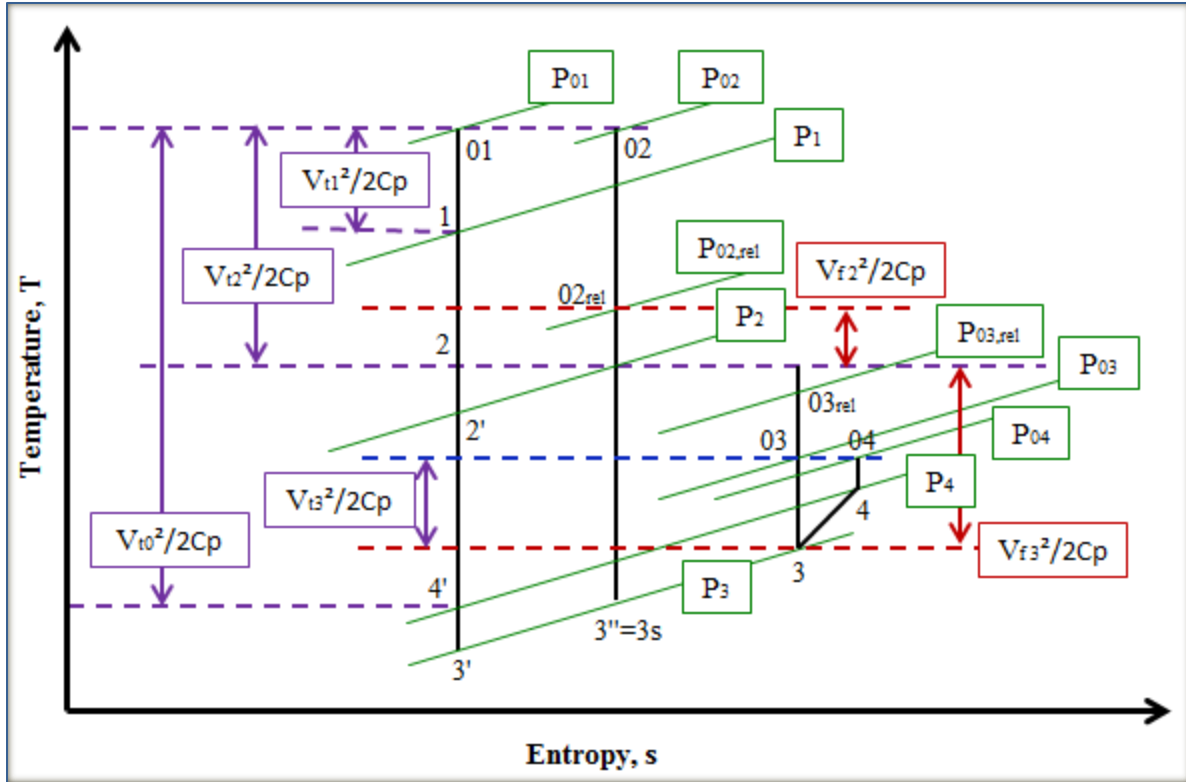


Figure 48. T-s Diagram for a Radial Inflow Turbine

Given design condition operation, as described, inlet relative fluid velocity is purely radial and discharge absolute fluid velocity is purely axial. This yields a tangential inlet fluid velocity equal to the impeller inlet velocity, simplifying the specific work output calculation, as given in Equation 69. The inlet impeller velocity is 69.9 m/s and the mass flow rate is 1.22 kg/s. The resulting specific work per kg of fluid is 4.89 kJ/kg. The specific power output given by the turbine is 5.96 kW.

$$w_{s,out,t} = U_{2,t}V_{t2,t} = U_{2,t}^2 = \frac{1}{2}[(U_2^2 - U_3^2) - (V_{f2}^2 - V_{b3}^3) + (V_{b2}^2 - V_{a3}^2)] \quad [69]$$

$$P_{s,out,t} = \dot{m}w_{s,out,t} = \dot{m}(Cp_2 T_{02,t} - Cp_3 T_{03,t}) = \dot{m}U_{2,t}V_{t2,t} = \dot{m}U_{2,t}^2 \quad [70]$$

The relationships shown in Figure 48 are used to define majority of the temperature states through the turbine, as shown in the series of equations below. The specific heat at the turbine inlet is used to provide an acceptable estimate in the calculations. The entropy at the turbine inlet is calculated by EES using NIST data by entering the temperature and expected pressure at the inlet.

$$T_{2,t} = T_{02,t} - \left(\frac{V_{b2,t}^2}{2Cp} \right) \quad [71]$$

$$T_{3,t} = T_{2,t} - \left(\frac{V_{f3,t}^2}{2Cp} \right) \quad [72]$$

$$T_{03,t} = T_{3,t} + \left(\frac{V_{t3,t}^2}{2Cp} \right) \quad [73]$$

Figure 48 shows points across the turbine where the change in entropy is zero. Thus, entropy at state 02 equals entropy at the isentropic state 3s. The pressure at state 3s is the same as the pressure at state 3. The pressure at state three can be determined in EES by knowing the temperature at 3, which is known, and the entropy at 3, which is equal to the entropy at state 03. Given that the ideal temperature is being calculated, the ideal pressure at state 03 is used. This ideal pressure at state 03, 8 MPa, is the counterpart to the inlet of the compressor. A simple EES code is used to connect the states, as described, providing the ideal temperature at state 3s. The temperature results at the states described are listed in Table 7. This table shows a large difference between the stagnation temperature at state 03 and the ideal outlet temperature at stage 3s. This means that the discharge pressure is likely higher than that designed for the compressor inlet condition. Experimental testing and analysis will provide accurate measurements that

will resolve this issue. EES code written to estimate actual discharge pressure based on temperature and entropy calculations yields 11.9 MPa, a very small change.

Table 7. Turbine Stage Temperature Results

Turbine State Temperatures	
State	Temperature (°C)
02	550
2	546
03	544
3	543
3s	480

The efficiency can be estimated by the Ns-Ds diagram displayed in Figure 21. The specific speed and specific diameter are calculated with Equations 36 and 42. The actual turbine dimensions at the exit, the mass flow rate of 1.22 kg/s, and a rotational speed of 44,527 rpm are used. If the pressure ratio matches the compressor, but the temperature changes only to 544 °C, the fluid density used to calculate the volumetric flow rate will be 38.15 kg/m³. On the other hand, if the performance of the turbine reaches only 11.9 MPa and 544 °C upon exit, the density will be 56.23 kg/m³. Other thermophysical properties needed to calculate Ns and Ds are also taken under these two conditions. The resulting efficiency estimates given by each of these are very low due to the small temperature difference in either case. The H_{ad} value is much too low to produce high efficiency, particularly in the specific diameter calculation.

7.4.3 Compressor Velocity Triangles

The compressor velocity triangles are defined by flow conditions, impeller velocity, and impeller geometry. Impeller radii dimensions and the rotational speed of the shaft determine the base calculations. The rotational speed, N, used for the shaft, is the design point value of 44,527 rpm. The defining radii are

as follows: hub radius, $r_{h,c}$, 0.20 in (0.00508 m); impeller eye, or outer inlet, radius, $r_{2,c}$, 0.39 in (0.009906 m); and impeller outlet radius, $r_{3,c}$, 0.73 in (0.018542 m). The mean inlet blade radius is 0.295 in (0.007493 m). The inlet blade height is 0.0011 m. The impeller velocity at the inlet, $U_{2,c}$, the mean inlet impeller velocity, $U_{2m,c}$, and the impeller velocity at the exit, $U_{3,c}$, are calculated as follows:

$$U_{2,c} = 2\pi r_{2,c} N = 2\pi(0.009906 \text{ m})(44,527 \text{ rpm}) \left(\frac{1 \text{ min}}{60 \text{ s}} \right) = 46.2 \text{ m/s} \quad [74]$$

$$U_{2m,c} = 2\pi r_{2m,c} N = 2\pi(0.007493 \text{ m})(44,527 \text{ rpm}) \left(\frac{1 \text{ min}}{60 \text{ s}} \right) = 34.9 \text{ m/s} \quad [75]$$

$$U_{3,c} = 2\pi r_{3,c} N = 2\pi(0.018542 \text{ m})(44,527 \text{ rpm}) \left(\frac{1 \text{ min}}{60 \text{ s}} \right) = 86.5 \text{ m/s} \quad [76]$$

The compressor exit blade angle is defined by the use of the SolidWorks drawing. A tangent line is created perpendicular to a radius line through the center origin. Linear interpolation is used to estimate the exit blade angle using a chosen point near the end of the blade curve, shown as a blue dot on the blade curve in Figure 49, along with the point defining the exit tip of the blade curve. This line is also displayed in blue, extending past the impeller from the chosen point described. The dimension tool is used to define the magnitude of the angle, rounded to 66.8° for calculation purposes and acknowledging linear estimation error. This angle is denoted $b_{3,c}$ in the compressor exit velocity diagram, shown in Figure 49.

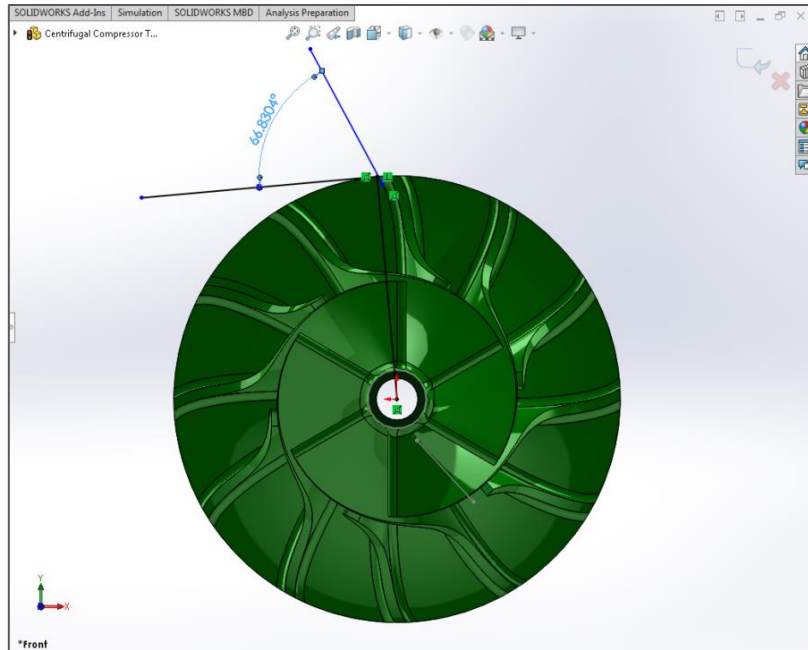


Figure 49. Compressor Exit Blade Angle Definition using SolidWorks

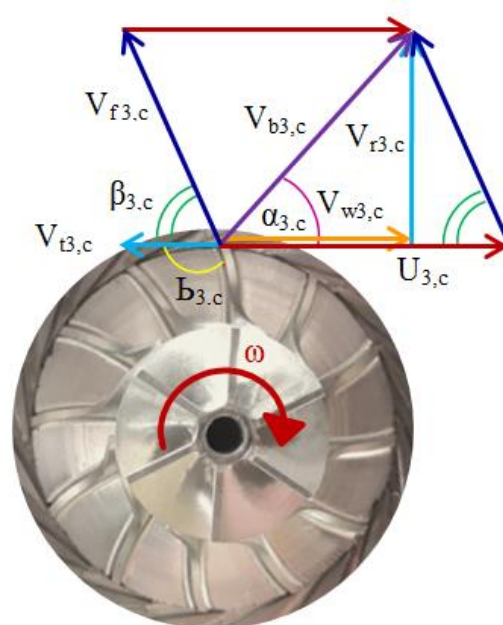


Figure 50. Velocity Diagram for the Compressor Exit

The fluid velocity relative to the impeller at the exit is calculated using the tube diameter for design conditions. However, when blade geometry is known in its entirety, the characteristic flow area is determined by the impeller shroud, or exit, diameter and the blade height by Equation 68. Given this characteristic flow area, $1.282\text{E-}4\text{ m}^2$, the mass flow rate, 1.22 kg/s , and the density at the expected compressor outlet conditions, 672.2 kg/s , the fluid velocity relative to the impeller at the exit is 14.2 m/s .

The remaining components in the velocity diagram are calculated with geometric and trigonometric identities, and are summarized in Table 8.

Table 8. Compressor Exit Velocity Triangle Results

Compressor Exit Velocity Triangle Results			
Description	Label	Value	Unit
Exit Impeller Velocity	$U_{3,c}$	86.5	m/s
Relative Fluid Velocity	$V_{f3,c}$	14.2	m/s
Absolute Fluid Velocity	$V_{b3,c}$	81.9	m/s
Tangential Fluid Velocity	$V_{t3,c}$	5.6	m/s
Radial Fluid Velocity	$V_{r3,c}$	13.0	m/s
Whirl Velocity	$V_{w3,c}$	80.9	m/s
Absolute Flow Angle	$\alpha_{3,c}$	9.1	Degrees
Flow Exit Angle	$\beta_{3,c}$	66.8	Degrees
Exit Blade Angle	$b_{3,c}$	113.2	Degrees

The inlet velocity triangle is displayed in Figure 51. Fluid flows into the compressor in the axial direction. The axial inlet fluid velocity is calculated by the characteristic flow area at the inlet, defined by the difference between the hub and eye diameters, $2.27\text{E-}4\text{ m}^2$, the density at the expected compressor inlet conditions, 419.2 kg/m^3 , and the flow rate, 1.22 kg/s , and yields 12.8 m/s . At the tip of the blade eye,

using the impeller velocity at the outer edge of the impeller eye, the beta angle describing the absolute velocity direction is 74.5° , and the absolute fluid velocity, $V_{b2,c}$, is 47.9 m/s. Using the mean impeller velocity to calculate the flow, the beta angle is 69.9° and the absolute fluid velocity at the midpoint, $V_{bm2,c}$, is 37.2 m/s.

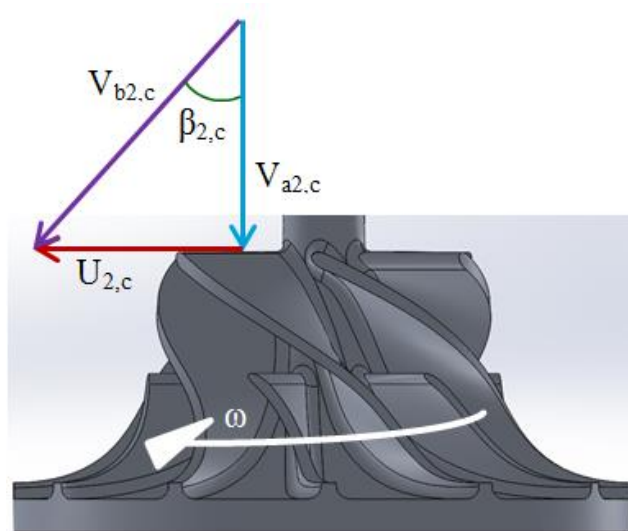


Figure 51. Velocity Diagram for the Compressor Inlet

7.4.4 Further Compressor Analysis

The velocity diagrams provide the bases for further analysis of the compressor output, requirement, and efficiency. The work per unit of mass is given by Euler as Equation 77. As discussed, the whirl velocity at the inlet of the compressor is zero for radial inflow. Thus, the work per unit mass of fluid provided by the compressor is given by the product whirl velocity and the impeller velocity, and is 7.00 J/kg. With a 1.22 kg/s mass flow rate, the compressor power is 8.54 kW.

$$w_c = V_{w3,c}U_{3,c} - V_{w2,c}U_{2,c} \text{ [J/kg]} \quad [77]$$

The flow coefficient is the ratio of exit radial component of the fluid velocity to the exit impeller velocity, given by Equation 78. The flow coefficient of the compressor is 0.15.

$$\varphi_c = \frac{V_{r3,c}}{U_{3,c}} \quad [78]$$

The static pressure rise expected from the compressor is 2.23 MPa, given by Equation 79. The average density is typically used in this equation; however, carbon dioxide is responsive to changes in pressure and temperature. Therefore, the density at the expected inlet and exit conditions are used to calculate the change in both static pressure, here, and stagnation pressure. Furthermore, the velocity profile at the midpoint of the entry blade width is used to better characterize flow over the entire entry. The inlet blade velocity used in the calculation is the midpoint blade speed, $U_{2m,c}$. Inlet relative fluid velocity, which is axial at the inlet, does not change across the blade width; this is reflected in equation [79] as well.

$$\Delta P_c = P_{3,c} - P_{2,c} = \frac{1}{2}(\rho_{3,c}U_{3,c}^2 - \rho_{2,c}U_{2m,c}^2) + \frac{1}{2}(\rho_{2,c}V_{2f,c}^2 - \rho_{3,c}V_{f3,c}^2) \quad [79]$$

The stagnation pressure rise expected from the compressor is 4.19 MPa, given by Equation 80. In the latter part of this equation, the inlet absolute velocity at the midpoint is used to better estimate the entire flow at the entry. The density specific to the expected inlet and exit conditions are again used to provide a more accurate estimate.

$$\Delta P_{0,c} = \frac{1}{2}(\rho_{3,c}U_{3,c}^2 - \rho_{2,c}U_{2m,c}^2) + \frac{1}{2}(\rho_{2,c}V_{f2,c}^2 - \rho_{3,c}V_{f3,c}^2) + \frac{1}{2}(\rho_{3,c}V_{b3,c}^2 - \rho_{2,c}V_{bm2,c}^2) \quad [80]$$

This means that for an inlet pressure of 8.0 MPa, the outlet pressure provided by the compressor is more likely to be 12.19 MPa. The UNLV compressor impeller yields a pressure ratio 1.52, less than the 1.75 discussed in Section 3.4.3 for a system of similar size; however, this compressor does provide a significant pressure increase.

Compressor stage efficiency, given by Equations 82, is the ratio of the stagnation pressure per density of fluid to the product of the exit blade velocity and the exit whirl velocity. This equation requires the density be removed from the standard stagnation pressure equation. Due to the fact that the density at each condition is used, and this value is not averaged, the density removed stagnation pressure, $5775.1 \text{ m}^2/\text{s}^2$, is calculated by Equation 81. The UNLV system is a single stage system. The stage efficiency is 82.5%. This calculation shows the UNLV system has the potential to create the high stage efficiency desired.

$$\frac{\Delta P_{0,c}}{\rho} = \frac{1}{2}(U_{3,c}^2 - U_{2,c}^2) + \frac{1}{2}(V_{f2,c}^2 - V_{f3,c}^2) + \frac{1}{2}(V_{b3,c}^2 - V_{bm2,c}^2) \quad [81]$$

$$\eta_{s,c} = \frac{\Delta P_{0,c}}{\rho} \frac{1}{U_{3,c}V_{w3,c}} \quad [82]$$

In addition to stage efficiency, polytropic and isentropic, or adiabatic, efficiency are used to evaluate the performance of centrifugal compressors. A polytropic process describes a reversible process through which both work and heat transfer occur. This process is defined by Equation 83, where C_1 and C_2 are constants, and C_1 goes to zero when the process is also adiabatic. Polytropic efficiency compares the ideal work to the actual work given by the same system described by a specific pressure difference under

polytropic conditions. An isentropic process is an adiabatic process, which is defined by zero heat transfer into or out of a system, described by Equation 84.

$$\text{Polytropic Process} \rightarrow T \frac{ds}{dT} = C_1 \text{ and } PV^n = C_2 \quad [83]$$

$$\text{Adiabatic Process} \rightarrow P_2 V_{12}^\gamma = P_3 V_{13}^\gamma \quad [84]$$

Although adiabatic efficiency is widely used, it is not as accurate as polytropic efficiency when predicting centrifugal compressors (63). TMI (63) claims adiabatic efficiency is known to be more accurate in predicting the performance of air compressors. In completing efficiency calculations, it is found that adiabatic efficiencies range from 30.6% to 99.5% for different methods of calculation. This large discrepancy invalidates the confidence in adiabatic efficiency calculations. As a result, this compressor is described by stage efficiency and polytropic efficiency.

In order to evaluate polytropic efficiency, the ideal and the expected actual discharge, or exit, temperature values are calculated. In lieu of using the compressor outlet conditions based on the literature and listed in Table 4, the discharge pressure calculated in this section is used. The ideal discharge temperature, 55.75 °C, denoted T_{3s} , is calculated in EES using NIST data. An EES code determines the discharge temperature by using the pressure expected at the exit, 12.19 MPa, and the entropy at the compressor inlet, describing the zero entropy change condition. Conversely, if the ideal discharge temperature is calculated by the polytropic assumption, as shown in Equation 85, the discharge temperature is 52.3 °C. The latter uses the assumption that the specific heat ratio is constant over the compressor. Though only 3.45 °C lower, this assumption yields less accurate results; thus, the more accurate, former discharge temperature is used.

$$\frac{T_3}{T_2} = \left(\frac{P_2}{P_3}\right)^{(\gamma-1)/\gamma} \quad [85]$$

The actual discharge temperature is estimated using the stage efficiency, $\eta_{s,c}$, from Equation 82, with the ideal discharge temperature and the inlet temperature. This estimation is suggested by Peng (21), is specified in Equation 86, and yields an estimated actual discharge temperature of 60.15 °C.

$$T_{03} = \frac{1}{\eta_{s,c}} (T_{3s} - T_{01}) + T_{01} \quad [86]$$

Polytropic efficiency is calculated by Equation 87 using the temperature and pressure values described. The polytropic efficiency using this equation is 69.6%. A relational method for estimating polytropic efficiency of centrifugal compressors is displayed in Equation 88, given by J.P. Rollins and reprinted by Guo et al. (64). This relationship suggests that polytropic efficiency is a function of inlet volumetric flow rate. Per Equation 88, higher volumetric flow rates yield higher polytropic efficiencies. This relationship is consistent with the Ns-Ds diagram, shown in Figure 21. The equations calculating specific speed, Ns, and specific diameter, Ds, are affected by the volumetric flow rate. All else constant, higher volumetric flow rates result in lower Ds and higher Ns values. Referencing Figure 21 and noting the 80% efficiency zone compared to the lower efficiency zones, it is clear that, up to a certain limit, higher efficiencies correlate to lower Ds and higher Ns values. Polytropic efficiency calculated by Equation 88 is 63.4%. Generally, expected polytropic efficiency ranges are 70% to 85%, given by TMI (63), and 70% to 75%, given by Guo et al. (64). Both calculated efficiencies are very close to lying within the expected range.

$$\eta_{p,c} = \frac{dW_i}{dW_a} = \frac{dh_i}{dh_0} = \frac{\gamma - 1}{\gamma} \frac{(P_{03} - P_{02})/P_{02}}{(T_{03} - T_{02})/T_{02}} \quad [87]$$

$$\eta_{pRollins,c} = 0.61 + 0.03 \log(Q_{v2,c}) \quad [88]$$

The gas horsepower requirement by the compressor is calculated by Equation 91. As described by Guo et al. (64), the resulting unit is hp, given by the volumetric flow rate in cfm and the pressure in psi. The greater polytropic efficiency, 69.9%, is used; however, the average specific heat ratio is also used with the goal of achieving a more accurate result. The average specific heat ratio, $R_{pm,c}$, is 0.8662. The compressibility factors at the inlet and exit conditions are calculated in an EES code, again using NIST data. The compressibility factor at the inlet, $z_{2,c}$, is 0.3278; the discharge compressibility factor, $z_{3,c}$, is 0.4331. The gas horsepower requirement of the compressor is 39.82 hp, or 24.47 kW.

$$R_{p,c} = \frac{\gamma - 1}{\gamma} \quad [89]$$

$$R_{pm,c} = \frac{2R_{p2}R_{p3}}{R_{p2} + R_{p3}} \quad [90]$$

$$H_{pg,c} = \frac{Q_{v2,c}P_{02}}{229 \eta_p} \left(\frac{z_{2,c} - z_{3,c}}{2 z_{2,c}} \right) \left[\frac{\left(\frac{P_{03}}{P_{02}} \right)^{R_{pm}/\eta_p} - 1}{R_{pm}/\eta_p} \right] \quad [91]$$

The work done is estimated by the velocity diagram and Equation 92. In the case of axial inflow, there is none to negligible whirl velocity at the inlet; therefore, the work is based upon the exit impeller velocity and the exit whirl velocity. The work done by the compressor is 8.54 kW.

$$W_{\text{out},c} = \dot{m}(U_{3,c}V_{w3,c} - U_{2,c}V_{w2,c}) \quad [92]$$

Shaft work received by the gas, $W_{s,c}$, is given by Equation 93. The right portion of the equation can be further reduced, however, is not to allow for different specific heat ratios to be included. The specific heat ratio in the denominator and the absolute fluid velocity at the inlet are given by mean values. This equation is rearranged to yield 13.82 kW of shaft work to the fluid by the compressor.

$$-\int_1^2 Pdv = W_{s,c} + \frac{V_{2m}^2}{2} - \frac{V_3^2}{2} + P_{02}v_{02} - P_{03}v_{03} = \frac{P_2v_2}{1 - \gamma_m} \left(\frac{v_3^{(1-\gamma_3)}}{v_2^{(1-\gamma_2)}} - 1 \right) \quad [93]$$

7.5 System Analysis Summary

The resulting analysis of all of the components described in this chapter show that the UNLV system is a viable prototype, with some components operating exactly as desired and others likely benefiting from design optimization. The solar receiver and heat rejection systems yield results that support their current design. Both of these components are performing as desired. The compressor analysis shows the expected performance is close to the expected outcome. Operating at the given design points of 1.22 kg/s and 44,527 rpm, the compressor is expected to yield a pressure ratio of 1.52, allowing the pressure to rise from 8.0 MPa to 12.19 MPa. As previously discussed, this pressure ratio is not far from the 1.75 published for similar sized systems in the literature. Furthermore, the compressor impeller alone has high efficiency potential. The turbine analysis shows less favorable results when compared to the compressor, however, is in operational condition and results from future progress will confirm or deny this expectation. Additionally, the compressor and turbine are connected by a shared shaft during system operation. This means that one will affect the other. This should also be considered in full system data analysis, as results show optimization of the turbine will provide more improvement than optimization of the compressor.

CHAPTER 8. RECOMMENDATIONS FOR FUTURE WORK

Future work is already in progress on the UNLV concentrated solar power supercritical carbon dioxide Brayton cycle. Current work is largely related to the rotational capability of the turbomachinery. Once the rotational capability of the turbocompressor shaft, rotating inside the modular plate casing, reaches and is capable of maintaining the design condition of 44,527 rpm, experimental testing of the entire system can proceed. Work toward this goal is summarized in the following section.

Full system on-sun testing will provide the anticipated results required to experimentally characterize the turbocompressor and the XJTU recuperators. The turbine and compressor impellers will be evaluated as one turbocompressor unit, as they share one shaft. These data can be used in conjunction with the analysis in this research to compute an appropriate optimization cost-benefit. The experimental data collected across each of the recuperators will provide experimental characterization of these components, and efficiency gains can be calculated. These data can also be compared to the experimental data using carbon dioxide and water collected by the Xi'an Jiaotong University research team, advancing the existing international collaboration between UNLV and XJTU.

Beyond this phase, the power generation system will be added. Plans have been made to incorporate power generation using strong magnetic rotation across the end plate. This is likely best completed in a split, secondary loop, which is a common solution in the literature for reaching this goal. Though there are various configurations, a split loop separates the flow out of the solar receiver and into two turbine flow paths, one to power the compressor and the other purely for power output. The flow reconvenes prior to the entry of the recuperator, where the flow already enters through a slightly larger tube diameter.

8.1 Current Progress toward Future Work

8.1.1 Bearings

Rotational capability is both limited by and permitted by bearings. In this case, standard bearings cannot be used, as the temperature of the fluid, and, subsequently, the bearings are extremely high. The initial trials were completed with ceramic ball bearings. These bearings were assured by the manufacturer to allow the desired rotational speed without degradation due to temperature. Unfortunately, initial tests revealed small amounts of powder residue. This means that the rotation was causing ceramic degradation of the ceramic balls. It could be that these bearings work better under steady conditions; however, this system is operational with the presence of the sun and will have daily start-up and shut-down conditions. The elimination of rubbing between ceramic balls is typically achieved by caged designs. Again, unfortunately, the caged designs available on the market are not able to withstand the high temperature conditions.

The solution currently being optimized and tested is the use of air bearings. Air bearings use air or another gas to provide an interface between the shaft and the casing by means of pressure adjustments. The bearings are designed to provide pressure in the radial direction to hold the shaft in a central location, and pressure in the form of thrust to center the turbine and compressor wheels between the housing ends. Figure 26 provides a visual reference for the need for pressure in both the radial and the thrust directions. Testing is currently being conducted using air as the balancing fluid. The rotational speed is measured using the optical rotational speed sensor described in Section 5.6 of this document and a small PLC. The test configuration is displayed in Figure 52. The tubes entering the side of the casing are the feed tubes, and the pressure is visually monitored with the gage shown. The filter connected to the feed tubes assures that no foreign elements enter the flow space. The very small tolerances throughout the turbocompressor unit require extreme care in this regard.

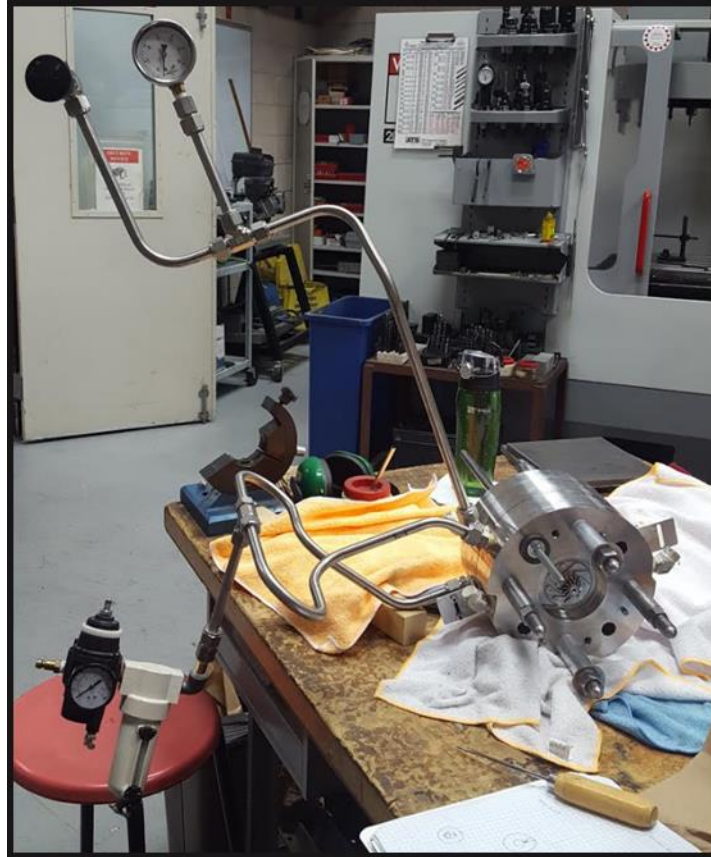


Figure 52. Air Bearing Test Configuration

The initial air bearing iteration featured a combined flow path to the exit holes. Tests using this configuration did not perform as desired. It was found that the combined exit flow path limited operation by prohibiting individual control of the radial and thrust pressure. In other words and for example, as the shaft dropped to the bottom of the shaft space, the path of least resistance bypassed that required to rebalance the shaft to the center of the space. The current iteration separates the radial and thrust flows, and has optimized the size of the thrust holes to more efficiently center the component in the thrust direction. The current iteration is shown in Figure 53 alongside the drill bits used to fabricate the holes. The radial and thrust holes are 0.020 inches in diameter, and the channel feed and through holes are 0.0625 inches in diameter. The radial holes are nearly unseen in the figure due to their small size, though

they do pass through the bearing. An angled view of this bearing is displayed in Figure 54. This view shows the air channel.

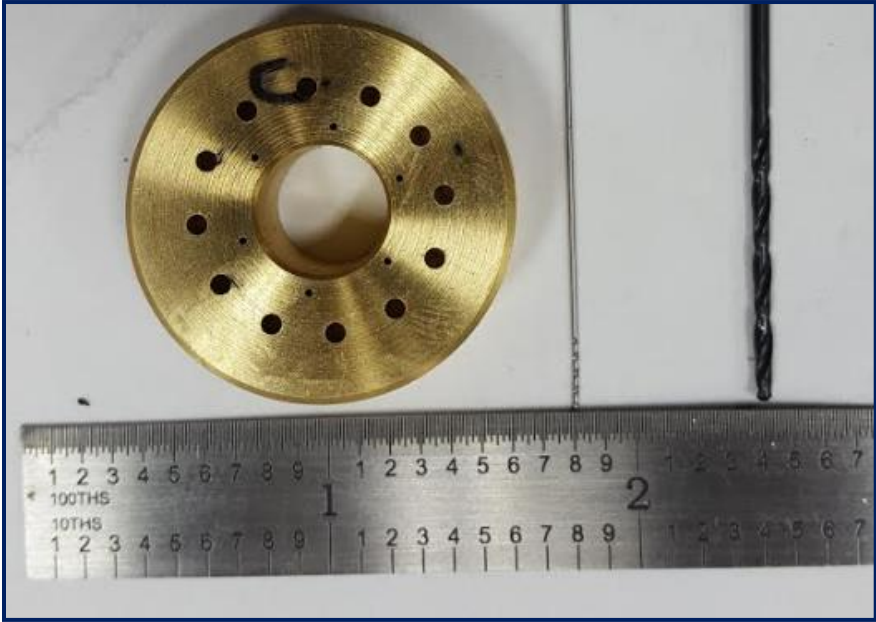


Figure 53. UNLV Air Bearing



Figure 54. Angled View of a UNLV Air Bearing

Tests using this second iteration show greatly improved results, displayed in Figure 55. Start-up was done by increasing air flow slowly through the filling channel. The results show oscillation between 15,000 and 20,000 rpm, after which the rotation quickly reached 43,170 rpm, very near the 44,527 rpm design condition. Once reached, the air flow pressure was slightly decreased before the system was permitted to float without flow. Subsequent tests reveal rotational restriction near but below 20,000 rpm. This restriction appears neat the oscillation rotational speed given by the first trial. This rotational speed may correspond to a resonant frequency. Modifications are currently being discussed, and additional tests will be conducted.

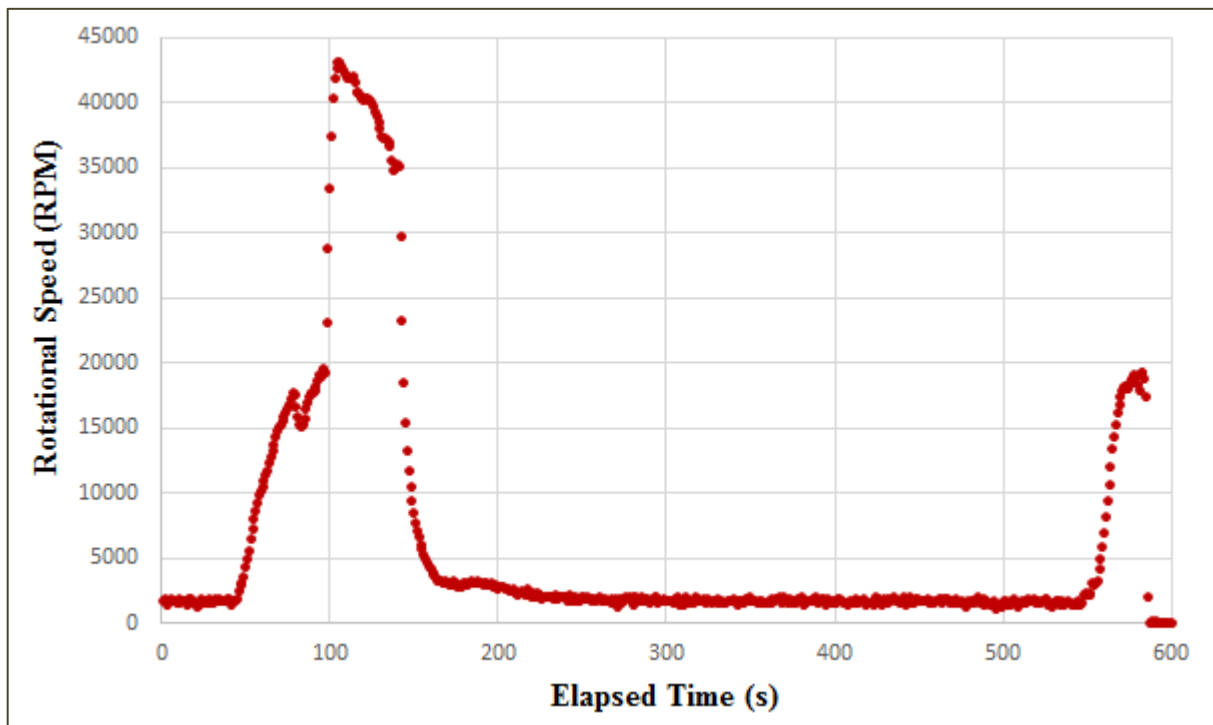


Figure 55. Rotational Speed Measurements using a UNLV Separated Channel Air Bearing

APPENDIX A.

8.2 EES Raw Full System Code

'SYSTEM STARTING POINTS'

```
q=113000[W]
mdot=0.16[kg/s]
RecT2=500[C]
CompP1=7700[kPa]
Tamb=30[C]
"Pressure at Turbine Outlet, Optimal Pressure Ratio for SCCO2 Brayton is found to be 2.6, ref: Yoon, Sandia use 1.6"
CompPratio=1.6
CompEff=0.75 "assumed from radial machinery range 0.70-0.85"
TurbPratio=1.6
TurbEff=0.75
```

"AClengthNTU defined by component"

```
AClengthNTU=20[m]
```

"Fan Speed"

```
"Given Fan Speed, Conversion 1 m^3/s = 2118.88 CFM, Air Density 1.185 kg/m^3"
ACVfanm3s=6000 "Standard 24 in fan at lowes is 7860 cfm; at 6000 CFM Tfout=33.78 C"
ACVfanm3s=ACVfanm3s/2118.88
ACmdotAir=ACVfanm3s*1.185
```

"1/2 Tube"

```
Do12=0.0012[m]
Df12=0.0105918[m]
rf12=Df12/2[m]
Af12=pi*(rf12^2)
```

'RECEIVER/TURBINE INTERFACE'

```
Reclength=54.884[m]
"Receiver Outlet, Estimate Pressure inlet to Turbine by pressure drop"
"Pressure Calculations HT text p861"
"Friction factor based on Moody HT text p480 in a smooth tube laminar flow=f/64/Red"
"...for turb Red<=2E4 f=0.316Red^-0.25, for turb Red>=2E4 f=0.184Red^-0.2"
"...for high Re using Petukhov form f=(0.790 ln Red-1.64)^-2"
"Estimating Re by using inlet pressure and outlet temp"
RecP1=X*P2o
Recmuf=Viscosity(CarbonDioxide, T=RecT2, P=RecP1)
Recrho=Density(CarbonDioxide, T=RecT2, P=RecP1)
RecRe=4*mdot/(3.1415*Df12*Recmuf)
"Friction Factor using Re calculation"
Recf=(0.79*LN(RecRe)-1.64)^(-2)
"Fluid velocity um=4*mdot/(rho*pi*D^2)"
Recum=4*mdot/(Recrho*3.1415*Df12^2)
"deltaP=friction factor*density*fluid velocity^2*char length/(2D) in [Pa]"
RecdeltaP=Recf*Recrho*Recum^2*Reclength/(1000*2*Df12) "in kPa for dividing by 1000"
"Defining AC Outlet Pressure, where P1rec is the outlet of the XJHEX"
RecP2=RecP1+RecdeltaP "*****Add or Subtract*****"
```

"For test using high estimate"

```
"RecP2=20000[kPa]"
```

'TURBINE'

```
TurbP1=RecP2
TurbT1=RecT2
Turbh1=ENTHALPY(CarbonDioxide,T=TurbT1,P=TurbP1)
```

Turbs1=ENTROPY(CarbonDioxide,T=TurbT1,P=TurbP1)
 "Determine P2turb with Pratio in System Starting Points"
 TurbP2=TurbP1/TurbPratio
 "Determine Outlet Temperature by using specific heat ratio $k=Cp/Cv=1.289$; Assume Isentropic"
 $TurbT2=TurbT1*((TurbP2/TurbP1)^{((1.289-1)/1.289)})$
 Turbh2=ENTHALPY(CarbonDioxide,T=TurbT2,P=TurbP2)
 Turbs2=ENTROPY(CarbonDioxide,T=TurbT2,P=TurbP2)
 "Work Output of Turbine per unit mass"
 $WorkTurbOutperkgmass=Turbh1-Turbh2$
 $WorkTurbOutIdealkW=WorkTurbOutperkgmass*\dot{m}$
 $WorkTurbOutActkW=WorkTurbOutIdealkW*TurbEff$

XIAN JIAOTONG UNIVERSITY HEX (XJHEX)
 "Inlet Parameters h=hot turbine side, c=cold compressor side, Pressure in kPa"
 XT1h=TurbT2
 XT1c=CompT2
 XP1h=TurbP2
 XP1c=CompP2

"Outlet Parameters, Pressure in kPa where $dPhot=0.8$ and $dPcold=0.89$ for straight finned model"
 "dT_s determined from XJ model"
 $XT2h=XT1h-(495-311.8)$
 $XT2c=XT1c+(403.1-218.2)$
 $XP2h=XP1h*0.8$
 $XP2c=XP1c*0.89$

AIR COOLED SYSTEM
 "Set Estimated Parameters"
 ACTw=40[C] "Wall Temp"
 ACPw=101.325[kPa] "Wall or Air Pressure"
 ACTf=XT2h "From XJHEX"
 "Desired fluid outlet temp to be calculated below, based on specified q"
 ACPf=XP2h "Bulk Fluid Pressure, based on outlet of XJHEX at 13500 ACP2=13154"

"Fluid Props"
 AChf=enthalpy(CarbonDioxide,T=ACTf,P=ACPf)
 ACrhof=density(CarbonDioxide, T=ACTf, P=ACPf) "Approx Density CO2"
 ACrhow=density(Air, T=ACTw, P=ACPw) "Density of Air"
 ACCpfh=Cp(CarbonDioxide, T=ACTf, P=ACPf) "Spec Heat CO2 at hot (inlet) temp"

ACCpw=Cp(Air, T=ACTw)
 ACnuf=KinematicViscosity(CarbonDioxide, T=ACTf, P=ACPf)
 ACmuf=Viscosity(CarbonDioxide, T=ACTf, P=ACPf)
 ACalphaf=ThermalDiffusivity(CarbonDioxide, T=ACTf, P=ACPf)
 ACKf=Conductivity(CarbonDioxide, T=ACTf, P=ACPf)

"Characteristic Values"
 ACPPr=Prandtl(CarbonDioxide, T=ACTf, P=ACPf)
 $ACVf=\dot{m}/(ACrhof*Af12)$
 $ACRe=ACVf*Df12/ACnuf$
 $ACReD=4*\dot{m}/(3.1415*Df12*ACmuf)$
 "Nusselt Number from Hoo-Kyu Nu-5 for $Tb/Tpc>1$ and forced convection in horizontal macro-tubes"
 "Use Inlet Temp ACCpfh"
 ACa=0.023
 ACb=0.7
 ACCc=2.5

ACd=0
 ACe=-3.5
 ACNuHooFC=ACa*ACRe*ACb*ACPr*ACc*(ACrhof/ACrhow)^ACd*(ACCpfn/ACCpw)^ACe
 AChtcHooFC=ACNuHooFC*ACk/Df12
 ACNuHooGen=0.023*ACRe*ACb*ACPr*ACc*(ACCpfn/ACCpw)^ACe "General Eq"
 AChtcHooGen=ACNuHooGen*ACk/Df12
 AChtcAir=200 "Given in google for FC, mod speed, cross-flow over a cylinder"

 "Effectiveness NTU p.649"
 ACU=1/((1/AChtcHooFC)+(1/AChtcAir)) "Choose an h value?????"
 "Determine Cmin for determining effectiveness (eta)"
 "Using Defined Value of q to determine outlet temp: qNTU=eff*Cpmin*(Tf-Tw) and eff=(Cpfn*(Tf-Tfout))/(Cpmin*(Tf-Tw))"
 "ACeff=q/(ACCpfn*(ACTf-ACTw))" "add mdot"
 "eff=Cpfn*mdot*(Tf-Tfout)/(Cpc*(Tf-Tw))"
 ACCpmin=if(ACCpw,ACCpfn,ACCpw,ACCpw,ACCpfn)
 ACCpc=ACCpmin*mdot
 ACCpmax=if(ACCpw,ACCpfn,ACCpfn,ACCpfn,ACCpw)
 ACCph=ACCpmax*mdot
 "For Cross-Flow Single Pass, both fluids unmixed ACeff=1-exp((1/ACCpr)*(ACNTU)^0.22*(exp(-ACCpr*(ACNTU)^0.78)-1))"
 ACCpr=ACCpc/ACCph "Cr=Cmin/Cmax"
 "Cross flow single pass air mixed and CO2 unmixed"
 ACeff=if(ACCpw, ACCpfn,ACeffminmix, ACeffminmix,ACeffmaxmix)
 ACeffmaxmix=(1/ACCpr)*(1-exp(-ACCpr*(1-exp(-ACNTU))))
 ACeffminmix=1-exp(-ACCpr*(-1)*(1-exp(-ACCpr*ACNTU)))
 "Second Eqn for ACTfout and ACTwout in previous ACeff Eqn"
 "*****Conflicting with Below, larger AC size values, but reasonable ACTfout= +128"
 ACeff=ACCpfn*(ACTf-ACTfout)/(ACCpmin*(ACTf-ACTw))
 "AClengthNTU defined in System Conditions"
 ACAreaNTU=ACNTU*ACCpc/ACU
 AClengthNTU=(ACAreaNTU-(2*pi*r12^2))/(2*pi*r12) "Using Surface Area of a Cylinder A=2pi r h+2pi r^2"
 "Determine Tair outlet using effectiveness formulas"
 ACTwout=(ACeff*ACCpc*(ACTf-ACTw)/(ACCpw))+ACTw "add mdotAir, try Cpc-Cpmin changes mdotAir=mdot"
 "Determine Tfout"
 "*****Conflicting with Above - This one provides 20 m ACHEX, but: ACTfout= -188"
 "ACmdotAir=mdot*ACCpfn*(ACTf-ACTfout)/(ACCpw*(ACTwout-ACTw))"
 "Determine Pressure Drop"
 "Pressure Calculations HT text p661"
 "Friction factor based on Moody HT text p460 in a smooth tube laminar flow=64/Red"
 "...for turb Red<=2E4 f=0.316Red^-0.25, for turb Red>=2E4 f=0.184Red^-0.2"
 "...for high Re using Petukhov form f=(0.790 ln Red-1.64)^-2"
 "Running code named Air Cooled HEX given Fan Speed Final, Re=670626"
 ACf=(0.79*LN(ACRe)-1.64)^(-2)
 "Fluid velocity um=4*mdot/(rho*pi*D^2)"
 ACum=4*mdot/(ACrho*3.1415*Df12^2)
 "deltaP=friction factor*density*fluid velocity^2*char length/(2D) in [Pa]"
 ACdeltaP=ACf*ACrho*ACum^2*AClengthNTU/(1000^2*Df12) "in kPa for dividing by 1000"
 "Defining AC Outlet Pressure"
 ACP2=ACPF-ACdeltaP

COMPRESSOR

"Limiting the inlet temperature to ambient"
 CompT1=if(ACTfout,30,30,30,Tamb)

"P1comp and effcomp defined in System Starting Points"

CompH1=ENTHALPY(CarbonDioxide,T=CompT1,P=CompP1)
 CompS1=ENTROPY(CarbonDioxide,T=CompT1,P=CompP1)
 "Determine P2 comp with Pratio in System Starting Points"
 CompP2=CompPratio*CompP1
 "Determine Outlet Temperature by using specific heat ratio k=Cp/Cv=1.289; Assume Isentropic"
 CompT2=CompT1/(((CompP1/CompP2)^((1.289-1)/1.289)))
 CompH2=ENTHALPY(CarbonDioxide,T=CompT2,P=CompP2)
 CompS2=ENTROPY(CarbonDioxide,T=CompT2,P=CompP2)
 "Compressor Work=enthalpy out-enthalpy in"
 WorkCompInperkgmass=CompH2-CompH1 "per kg mass"
 WorkCompInIdealkW=WorkCompInperkgmass*mdot
 WorkCompInActkW=WorkCompInIdealkW/CompEff

PERFORMANCE CALCULATIONS

"Percentage of Turbine Work Generated that is used by the Compressor, rbw, solved as a percentage"
 rbwpercent=WorkCompInActkW/WorkTurbOutActkW*100
 "Net Work"
 WnetkW=WorkTurbOutActkW-WorkCompInActkW
 effThermalSysqdefined=WnetkW/q
 qinturbcomp=Turbh1-CompH2
 effThermalSysqincalwh=WnetkW/qinturbcomp

REFERENCES

1. *A Photographic Flux Mapping Method for Concentrating Solar Collectors and Receivers*. **Clifford K. Ho, Siri S. Khalsa**. November 2012, Journal of Solar Energy Engineering, Vol. 134.
2. **Incropera, Frank P., et al., et al.** *Introduction to Heat Transfer*. 5th. Hoboken : John Wiley & Sons, Inc., 2007.
3. *Measurements of Heat Transfer Coefficients from Supercritical Carbon Dioxide Flowing in Horizontal Mini/Micro Channels*. **Liao, S.M. and Zhao, T.S.** June 2002, Journal of Heat Transfer, Vol. 124, pp. 413-420.
4. **National Weather Service Forecast Office**. Observed Weather Reports. *Annual Climate Report*.
[Online] January 1, 2018. [Cited: August 15, 2018.]
<https://w2.weather.gov/climate/index.php?wfo=vef>.
5. **Las Vegas Valley Water District**. Where your water comes from. *Las Vegas Valley Water District*.
[Online] 2018. [Cited: August 15, 2018.] <https://www.lvvwd.com/water-system/where-your-water-comes-from/index.html>.
6. **Braken, Nathan, et al., et al.** *Concentrating Solar Power and Water Issues in the U.S. Southwest*.
The Joint Institute for Strategic Energy Analysis, Operated by the Alliance for Sustainable Energy. Golden, CO : National Renewable Energy Laboratory, U.S. Department of Energy, 2015.
Technical Report. NREL/TP-6A50-61376.

7. *Analyzing land and water requirements for solar deployment in the Southwestern United States.* **Bukhary, Saria, Ahmad, Sajjad and Batista, Jacimaria.** 2018, Renewable and Sustainable Energy Reviews, Vol. 82, pp. 3288-3305.
8. *The Supercritical Thermodynamic Power Cycle.* **Feher, E.G.** s.l. : Fergamon Press, U.K., January 1968, Energy Conversion, Vol. 8, pp. 85-90.
9. *Benchmarking supercritical carbon dioxide cycles against steam Rankine cycles for concentrated solar power.* **V.T. Cheang, R.A. Hedderwick, C. McGregor.** March 2015, Solar Energy, Vol. 113, pp. 199-211.
10. *Thermodynamic Study of Advanced Supercritical Carbon Dioxide Power Cycles for Concentrating Solar Power Systems.* **Craig S. Turchi, Zhiwen Ma, Ty W. Neises, Michael J. Wagner.** November 2013, Journal of Solar Energy Engineering, Vol. 135.
11. *Comparison of Supercritical CO₂ Gas Turbine Cycle and Brayton CO₂ Gas Turbine Cycle for Solar Thermal Power Plants.* **Yaushi Muto, Masanori Aritomi, Takao Ishizuka, Noriyuka Watanabe.** Pittsburgh, Pennsylvania : s.n., September 2014. The 4th International Symposium - Supercritical CO₂ Power Cycles.
12. *Supercritical Carbon Dioxide turbomachinery design for water-cooled Small Modular Reactor application.* **Lee, Jekyoung, et al., et al.** 2014, Nuclear Engineering and Design, Vol. 270, pp. 76-89.
13. *A Review of Using Supercritical CO₂ Brayton Cycle in Renewable Energy Applications.* **Chu, Wen-xiao, et al., et al.** 1, June 2018, Journal of Renewable Energy and Sustainable Development (RES-D), Vol. 4, pp. 14-20. ISSN 2356-8569.

14. *Second law analysis of supercritical CO2 recompression Brayton cycle.* **Sarkar, Jahar.** 2009, Energy, Vol. 34, pp. 1172-1178.
15. *Review of Supercritical CO2 Power Cycle Technology and Current Status of Research and Development.* **Ahn, Yoonhan, et al., et al.** 2015, Nuclear Engineering Technology, Vol. 47, pp. 647-661.
16. *Summary of the Sandia Supercritical CO2 Development Program.* **Wright, Steven A.** Boulder, Colorado : s.n., May 2011. SCO2 Power Cycle Symposium.
17. **Dostal, V., Driscoll, M.J. and Hejzlar, P.** *A Supercritical Carbon Dioxide Cycle for Next Generation Nuclear Reactors.* Advanced Nuclear Power Technology Program, Massachusetts Institute of Technology. 2004. Annual and Progress Report. MIT-ANP-TR-100.
18. *Fast and reliable flux map on cylindrical receivers.* **Collado, Francisco J. and Guallar, Jesus.** 2018, Solar Energy, Vol. 169, pp. 556-564.
19. *Visual HFLCAL- A Software Tool for Layout and Optimization of Heliostat Fields.* **Schwarzbozl, Peter, Pitz-Paal, Robert and Schmitz, Mark.** Berlin, Germany : SolarPACES, 2009.
20. **Vilim, Richard B.** *Development and Validation of a Radial Inflow Turbine Model Simulation of the SNL S-CO2 Split-Flow Loop.* Nuclear Engineering Division, Argonne National Laboratory. Argonne, IL : U.S. Department of Energy, 2011. Technical Report. ANL-ARC-195.
21. **Peng, William W.** *Fundamentals of Turbomachinery.* Hoboken : John Wiley and Sonc, Inc., 2008.

22. **Wright, Steven A., et al., et al.** *Operation and Analysis of a Supercritical CO₂ Brayton Cycle*. s.l. : Sandia National Laboratories, 2010. Sandia Report. SAND2010-0171.
23. *Gas Turbines: Axial and radial turbines*. **TMI Staff and Contributors**. December 27, 2012, Turbomachinery International.
24. *Supercritical CO₂ Brayton Cycles for Solar Thermal Energy*. **Brian Iverson, et al.** s.l. : Applied Energy, 2013, Vol. 111.
25. *Advanced Supercritical Carbon Dioxide Power Cycle Configurations for Use in Concentrating Solar Power Systems*. **Ma, Zhiwen and Turchi, Craig S.** Boulder, CO : s.n., 2011. Supercritical CO₂ Power Cycle Symposium. NREL/CP-5500-50787.
26. *Back to Basics: Selecting a Centrifugal Compressor*. **Sorokes, James M.** s.l. : American Institute of Chemical Engineers, June 2013, Chemical Engineering Progress. 20130644.
27. **National Institute of Standards and Technology**. NIST Chemistry WebBook, SRD 69. *NIST Standard Reference Data*. [Online] United States Secretary of Commerce on behalf of The United States of America, 2017. [Cited: September 6, 2018.]
<https://webbook.nist.gov/cgi/cbook.cgi?ID=C124389&Mask=4>.
28. *Supercritical CO₂ Power Cycles: Design Considerations for Concentrating Solar Power*. **Ty Neises, Craig Turchi**. Pittsburgh, Pennsylvania : s.n., September, 2014. The 4th International Symposium - Supercritical CO₂ Power Cycles.
29. *Modeling and analysis of a printed circuit heat exchanger for supercritical CO₂ power cycle applications*. **Ajinkya Meshram, Ankush Kumar Jaiswal, Sagar D. Khivsara, Jesus D.**

- Ortega, Clifford Ho, Rucha Bapat, Pradip Dutta.** October 25, 2016, Applied Thermal Engineering, Vol. 109 Part B, pp. 861-870.
30. *Study on local thermal-hydraulic performance and optimization of zigzag-type printed circuit heat exchanger at high temperature.* **Ting Ma, Lei Li, Xiang-Yang Xu, Yi-Tung Chen, Qui-Wang Wang.** March 2015, Energy Conversion and Management, Vol. 104, pp. 55-66.
31. *Performance comparison of different supercritical carbon dioxide Brayton cycles integrated with a solar power tower.* **Al-Sulaiman, Fahad A. and Atif, Maimoon.** 2015, Energy, Vol. 82, pp. 61-71.
32. *Integration between supercritical CO₂ Brayton cycles and molten salt solar power towers: A review and a comprehensive comparison of different cycle layouts.* **Wang, Kun, He, Ya-Ling and Zhu, Han-Hui.** 2017, Applied Energy, Vol. 195, pp. 819-836.
33. *Supercritical carbon dioxide Brayton cycle for concentrated solar power.* **Garg, Pardeep, Kumar, Pramod and Srinivasan, Kandadai.** 2013, Journal of Supercritical Fluids, Vol. 76, pp. 54-60.
34. *Development and integration of an Equation-Solving Program for Engineering Thermodynamics Courses.* **Klein, S.A.** 3, 1993, Computer Applications in Engineering Education, Vol. 1, pp. 265-275.
35. *Dynamic model of a supercritical carbon dioxide heat exchanger.* **Simoës, Pedro C., Fernandes, Joao and Mota, Jose Paulo.** 2005, Journal of Supercritical Fluids, Vol. 35, pp. 167-173.
36. *Technical Notes: Where did the Dittus-Boelter equation come from?* **Winterton, R.H.S.** 4-5, 1998, International Journal of Heat and Mass Transfer, Vol. 41, pp. 809-810. 0017-9310/98.

37. *Buoyancy driven convection in near-critical and supercritical fluids.* **Hasan, Nusair and Farouk, Bakhtier.** 2012, International Journal of Heat and Mass Transfer, Vol. 55, pp. 4207-4216.
38. *New Correlation to predict the heat transfer coefficient in-tube cooling supercritical CO2 in horizontal macro-tubes.* **Hoo-Kyu Oh, Chang-Hyo Son.** 8, November 2010, Experimental Thermal and Fluid Science, Vol. 34, pp. 1230-1241.
39. *Experimental heat transfer of supercritical carbon dioxide flowing inside channels (survey).* **Duffey, Romney B. and Pioro, Igor L.** 2005, Nuclear Engineering and Design, Vol. 235, pp. 913-924.
40. *Analysis on heat transfer correlations of supercritical CO2 cooled in horizontal circular tubes.* **Lin, Wensheng, Du, Zhongxuan and Gu, Anzhong.** 2012, Heat and Mass Transfer, Vol. 48, pp. 705-711. DOI 10.1007/s00231-011-0919-0.
41. *Heat transfer and pressure drop characteristics during the in-tube cooling process of carbon dioxide in the supercritical region.* **Yoon, Seok-Ho, et al., et al.** 2003, International Journal of Refrigeration, Vol. 26, pp. 857-864. DOI 10.1016/S0140-7007(03)00096-3.
42. **NASA Jet Propulsion Laboratory.** Solar System Dynamics - Horizons System. *NASA Jet Propulsion Laboratory, California Institute of Technology.* [Online] 2018. [Cited: March 9, 2015.] <https://ssd.jpl.nasa.gov/?horizons#top>.
43. *Development of the turbomachinery for the supercritical carbon dioxide power cycle.* **Cho, Junhyun, et al., et al.** 2016, International Journal of Energy Research, Vol. 40, pp. 587-599.

44. *Thermodynamic functions of Carbon Dioxide: Joule-Thomson Coefficient, Isochoric Heat Capacity, and Isentropic Behavior at 100 degrees to 1000 degrees C and 50 to 1400 Bars.* **Price, Donna.** 1956, Chemical and Engineering Data Series, pp. 83-86.
45. *Thermodynamic Functions of Carbon Dioxide: Enthalpy, Entropy, and Isobaric Heat Capacity at 100 degrees to 1000 degrees C and 50 to 1400 Bars.* **Price, Donna.** August 1955, Industrial and Engineering Chemistry, pp. 1649-1652.
46. **MegaWatSoft, Inc.** Carbon Dioxide Properties Calculator. *Carbon Dioxide Properties.* [Online] 2009-2018. <https://www.carbon-dioxide-properties.com/co2tablesweb.aspx>.
47. *Co2 velocity measurement and models for temperatures up to 200 degrees C and pressures up to 100 MPa.* **Han, De-Hua, Sun, Min and Batzle, Michael.** 3, May-June 2010, Geophysics, Vol. 75, pp. E123-E129. 10.1190/1.3383324.
48. *Velocity of sound in two-phase mixtures.* **Michaelides, E.E. and Zisis, K.L.** 2, June 1983, International Journal of Heat and Fluid Flow, Vol. 4, pp. 79-84.
49. **Som, S.K.** Disturbance Propagation, Stagnation, and Sonic Properties. s.l., India : National Programme on Technology Enhanced Learning, Indian Institute of Technology, March 9, 2015. pp. Mod-01 Lec-29 .
50. **Boyce, Meherwan P.** *Centrifugal Compressors: A Basic Guide.* Tulsa : PennWell Corporation, 2003. ISBN 0-87814-801-9.

51. *Preliminary Results of Optimal Pressure Ratio for Supercritical CO₂ Brayton Cycle Coupled with Small Modular Water Cooled Reactor.* **Ho Joon Yoon, et al.** s.l. : Supercritical CO₂ Power Cycle Symposium, May 2011.
52. **Boyce, Meherwan P.** *Gas Turbine Engineering Handbook.* 4th. Waltham : Butterworth-Heinemann, 2012.
53. *Design of a Radial Inflow Turbine for 30 kW Microturbine.* **Sangsawangmatum, Thanate and Nontakaew, Udomkiat.** Shanghai, China : MATEC Web of Conferences, 2017. 3rd Annual International Conference on Mechatronics and Mechanical Engineering. Vol. 95. DOI: 10.1051/mateconf/2017950.
54. **Nichols, Kenneth E.** *How to Select Turbomachinery for Your Application.* Arvada, CO : Barber Nichols Inc., 2015.
55. **McLallin, Kerry L. and Haas, Jeffrey E.** *Experimental Performance Analysis of 15.04-Centimeter-Tip-Diameter, Radial-Inflow Turbine with Work Factor of 1.126 and Thick Blading.* U.S. Army Avradcom, National Aeronautics and Space Administration. s.l. : NASA Scientific and Technical Information Branch, 1980.
56. **Wright, Steven A., et al., et al.** *Operation and Analysis of a Supercritical CO₂ Brayton Cycle.* s.l. : Sandia National Laboratories, 2010. Sandia Report. SAND2010-0171.
57. *Description and Test Results from a Supercritical CO₂ Brayton Cycle Development Program.* **Stephen A. Wright, Paul S. Pickard, Milton E. Vernon, Ross F. Radel, Robert Fuller.** Denver, CO : s.n., 2009. 7th International Energy Conversion Engineering Conference.

58. **Williams, Jim.** Application Note 28: Thermocouple Measurement. *Linear Technology*. [Online] February 1988. <http://www.analog.com/media/en/technical-documentation/application-notes/an28f.pdf>.
59. **Mosaic Industries, Inc.** RTD Calibration. *Mosaic Documentation Web*. [Online] <http://www.mosaic-industries.com/embedded-systems/microcontroller-projects/temperature-measurement/platinum-rtd-sensors/resistance-calibration-table>.
60. **National Weather Service.** Weather Observations for the Past Three Days, Las Vegas, McCarran International Airport. *www.weather.gov*. [Online] February 13, 2017.
61. **OPTEK Technology, Inc.** *Photologic Slotted Optical Switch*. Carrollton, TX : s.n., 2016. Specification Sheet. OPB930-940-L-W.2.0.pdf.
62. **Chen, Xiaolin and Liu, Yijun.** *Finite Element Modeling and Simulation with ANSYS Workbench*. 3rd. Boca Raton : CRC Press, 2015.
63. *Compressors: Centrifugal vs Reciprocating Compressor*. **TMI Staff and Contributors**. November 4, 2016, International Turbomachinery.
64. **Guo, Boyun, Lyons, William C. and Ghalambor, Ali.** *Petroleum Production Engineering: A Computer Assisted Approach*. Burlington : Gulf Professional Publishing, Elsevier, 2007.
65. *Calculation of the thermodynamic sound velocity in two-phase multicomponent fluids*. **Picard, D.J. and Bishnoi, P.R.** 3, May-June 1987, International Journal of Multiphase Flow, Vol. 13, pp. 295-308.

66. **Chen, Xiaolin and Liu, Yijun.** *Finite Element Modeling and Simulation with ANSYS Workbench.*

Boca Raton, FL : Copyright Clearance Center, Inc., 2015.

67. **Depasquale, John.** *Turbomachinery: Efficiency Class 02b.* s.l. : University of Connecticut, Spring

2014.

<http://www.engr.uconn.edu/~barbertj/ME3280%20Turbo/Notes/Class02b%20Efficiency.ppt>.

CURRICULUM VITAE

Danielle Nobles-Lookingbill

Danielle.NoblesLookingbill@gmail.com

EDUCATION

University of Nevada, Las Vegas

- ✿ Ph.D. in Mechanical Engineering, to be Conferred on 18 December 2018
Concentration in Thermal Science and Nuclear Engineering
GPA: 3.78
- ✿ Graduate Certificate in Nuclear Safeguards and Security
- ✿ Bachelor of Science in Mechanical Engineering, 2014

Indiana University, Bloomington

- ✿ Bachelor of Science in Psychology, 1999
- ✿ Certificate in Criminal Justice, 1999
- ✿ Psi Chi Member, National Psychology Honor Society

Universidad de Salamanca, Spain

- ✿ Minor In Spanish, 1997

HONORS

Nuclear Regulatory Commission Nuclear Engineering Fellow
University of Nevada, Las Vegas Graduate College STEM Fellow

CERTIFICATIONS

U.S. Certified Engineer in Training (EIT) – Fundamentals in Engineering Exam Passed 2014

PROFESSIONAL INTERNSHIP EXPERIENCE

DOE Mission Support and Test Services Remote Sensing Laboratory, Nellis, Summer 2018

Work supported by the Department of Homeland Security Domestic Nuclear Detection Office
Summer Internship Program

In coordination with Oak Ridge Institute for Science and Education

Unmanned Arial Radiation Detection Intern

Under the direction of Dr. Paul Guss, Dr. Russell Malchow, and Karen McCall, MS

Contributions and Training

- ✿ Contributed to the advancement of the Unmanned Arial Radiation Detection mission
- ✿ Analyzed data for isotope ratio distribution in a radioactive plume
- ✿ Wrote script for transferring data from RaptorX to the AVID software platform
- ✿ Successfully created and flew Mission Planner data collection flight surveys using the 3DR UAS aircraft
- ✿ Participated in manual flight training on T-28 and 3DR UAS platforms
- ✿ Participated in Piccolo training and flight control on the Sandstorm UAS aircraft
- ✿ Assisted with editing one proposal, two operations plans, and two Form 2087's

- ⚙ Completed the Counterterrorism Operations Support Preventive Radiological/Nuclear Detection Program
- ⚙ Participated in the 6th AMS International Technical Exchange on Uncertainty in Radiological Aerial Measurements, NNSS RSL, Las Vegas, NV

Xi'an Jiaotong University, Xi'an, Shaanxi, P.R. China, Summer 2017

International Graduate Researcher

Under the direction of Dr. Qiuwang Wang, Vice Dean, School of Energy and Power Engineering

Contributions and Collaborative Goals

- ⚙ Contributed to supercritical carbon dioxide cycle and mini-channel heat exchanger collaborative research
- ⚙ Designed a XJTU and UNLV laboratory research collaboration plan for advancement and publication
- ⚙ Solidified the use of mini-channel heat exchangers, custom fabricated by the Xi'an Jiaotong University research team, as recuperators in the UNLV supercritical carbon dioxide Brayton cycle
- ⚙ Experimental data analyses and efficiency are compared to designed specifications

PROFESSIONAL RESEARCH EXPERIENCE AND COLLABORATIVE WORK

UNLV Center for Energy Research

Graduate Researcher, Nexus in Nevada Graduate Student Lead

Under the direction of Dr. Robert Boehm, P.E., Distinguished Professor, Director, Center for Energy Research

Doctoral Research Project

NSF EPSCoR Solar Energy, Water, Environment Nexus in Nevada Research Project (Nexus in Nevada)

Supercritical Carbon Dioxide Brayton Cycle Application using a High Concentration Solar (CSP) System Heat Source

This Research is supported by the National Science Foundation under grant number IIA-1301726

- ⚙ Nexus in Nevada is a collaborative Nexus of solar, energy technology, and power grid advancements, ecological and environmental consideration and restoration, water reduction and water treatment, and computer technology and data integration that encompasses mechanical engineers, electrical engineers, civil and environmental engineers, computer scientists, economists, biologists, ecologists, and hydrologists from the University of Nevada, Las Vegas, the University of Nevada, Reno, and the Desert Research Institute
- ⚙ SCO₂ Brayton cycles are being researched to provide a smaller, more efficient power cycle alternative for heat flux sources able to provide high working fluid temperatures, such as CSP and nuclear power plants

Responsibilities

- ⚙ Sized and designed a high temperature and pressure SCO₂ Brayton cycle, including turbomachinery and all associated components
- ⚙ Solidified an international collaboration for system recuperation with a mini-channel heat exchanger

- ⚙ Developed vendor relationships, completed order requisitions within budget, and submitted invoices for payment
- ⚙ Assembled a sensing and data collection system compliant with the robust environment, controlled by a PLC
- ⚙ Developed an EES code to model SC02 Brayton cycle power generation with CSP or nuclear heat flux sources
- ⚙ Experimental data analyzed for effectiveness and optimization of this high temperature SC02 Brayton cycle
- ⚙ Mentored seven plus undergraduate students at various times on this and other projects
- ⚙ Solidified an \$8,000.00 research donation to the Center for Energy Research

Additional Research Project Initiatives

Educational Solar Hot Water Heating and Energy Generation Kits for STEM Outreach

- ⚙ Designed and developed three interactive Solar Laboratory Experience Kits: Solar Power Visualization; Off-Grid Solar Power: Charging Your Cell Phone; Solar Hot Water Heating
- ⚙ Developed corresponding laboratory curriculum for each kit
- ⚙ Kits are used in UNLV Solar and Renewable Energy Minor courses and at K-12 and community events
- ⚙ Successors have grown the project and the kits are now being shipped across all of Nevada

DOE Regional Test Center, Managed by Sandia National Laboratory: Soitec Concentrated and PV Solar Project

- ⚙ Involved in preparation and development planning
- ⚙ Assisted in installation, system operations, maintenance, and data collection

Amonix Concentrated PV Systems for Southern Nevada Water Authority and UNLV

- ⚙ Involved in multidisciplinary problem solving
- ⚙ Completed operational maintenance, including cleaning and string and cell testing

3M Project: Coated versus Uncoated Photovoltaic Panels

- ⚙ Completed on-site IV curve testing, remote data collection and analysis, and quarterly reports

RESEARCH PRESENTATIONS AND INTERVIEWS

Swiss Embassy USA Swiss Touch Event Interview and Expert Panel, 7 Magic Mountains, Nevada, June 2018

- ⚙ “Swiss Touch on the Road: Las Vegas Best of”
<https://www.youtube.com/watch?v=1tfRr4IJcCI&feature=youtu.be>
<https://www.swisstouchusa.org/>

Nexus in Nevada Interviews

- ⚙ “Solar-Driven Supercritical CO² Engine Development,” 2017
<https://www.youtube.com/watch?v=2N0B1qLyOLY>
<https://solarnexus.epscorspo.nevada.edu/videos/>
- ⚙ “Mentoring by Danielle Nobles-Lookingbill, PhD Student, University of Nevada, Las Vegas,” 2017
<https://www.youtube.com/watch?v=NcXhCibchFs>
- ⚙ “What impact does solar research have on Nevada?” 2014
<https://www.youtube.com/watch?v=PbuGb96Fucs>
<https://solarnexus.epscorspo.nevada.edu/videos/>

The 9th Chinese Renewable Energy Conference and Expo, Wuxi, P.R. China, Presentation, November 2017

- ✿ “UNLV Center for Energy Research Developments”

Solar Power International Technical Symposium, Poster, September 2017

- ✿ ”Design of a Supercritical Carbon Dioxide Brayton Cycle for Solar Dish Concentrator Clean Energy Production”

Xi’an Jiaotong University, Xi’an, P.R. China, Presentation, July 2017

- ✿ ”Supercritical Carbon Dioxide Brayton Cycle Application using an SAIC Solar Dish Concentrator”

VOLUNTEER COMMUNITY ENGAGEMENT

Project Manager for the Competitive Gear-Up Robotics Club, 2015-Present

- ✿ Facilitate teams at South East Career Technical Academy and East Career Technical Academy
- ✿ Promote engineering design, innovation, and education
- ✿ Organize and facilitate the year-end interschool competition, showcase, and awards ceremony

Math Tutor, 2014-Present

UNLV Academic and Research Advocate, 2013-Present

- ✿ Manage various events and conferences, including Green Fest, Solarbration, and the Clean Energy Summit

Southern Hills Baptist Church Volunteer